ILMATIETEEN LAITOS
METEOROLOGISKA INSTITUTET
FINNISH METEOROLOGICAL INSTITUTE

143
CONTRIBUTIONS

CHALLENGES IN MEASURING WINTER PRECIPITATION:

ADVANCES IN COMBINING MICROWAVE REMOTE SENSING AND SURFACE OBSERVATIONS

ANNKAISA VON LERBER

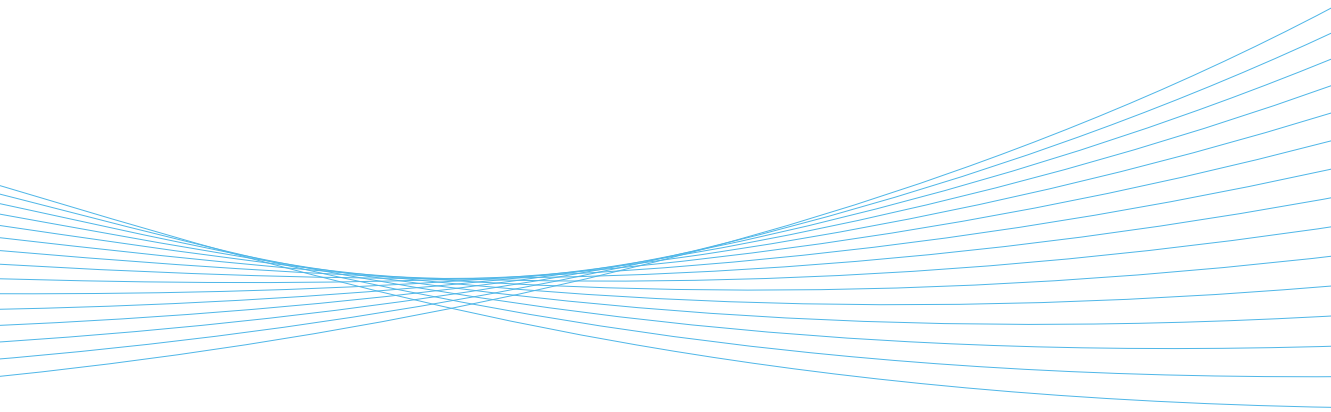

Aalto University publication series
DOCTORAL DISSERTATIONS 4/2018

Challenges in measuring winter precipitation:

Advances in combining microwave remote sensing and surface observations

Annakaisa von Lerber

A doctoral dissertation completed for the degree of Doctor of Science (Technology) to be defended, with the permission of the Aalto University School of Electrical Engineering, at a public examination held at the lecture hall Auditorio, Otakaari 3 on 1 February 2018 at 12.

This doctoral thesis is conducted in collaboration with Aalto University and Finnish Meteorological Institute.

Aalto University
School of Electrical Engineering
Department of Electronics and Nanoengineering
Space Science and Technology

Finnish Meteorological Institute
Earth Observation
Radar and Space Technology

Supervising professor
Professor Tuija Pulkkinen, Aalto University, Finland

Thesis advisors
Associate Professor Dmitri Moisseev, University of Helsinki, Finland

Professor V. Chandrasekar, Colorado State University, USA

Preliminary examiners
Dr. Wanda Szyrmer, McGill University, Canada

Dr. Sergey Matrosov, CIRES, University of Colorado, USA

Opponent
Professor Herman Russchenberg, Delft University of Technology, Netherlands

Aalto University publication series
DOCTORAL DISSERTATIONS 4/2018

ISBN 978-952-60-7790-1 (printed)
ISBN 978-952-60-7791-8 (pdf)
ISSN-L 1799-4934
ISSN 1799-4934 (printed)
ISSN 1799-4942 (pdf)
http://urn.fi/URN:ISBN:978-952-60-7791-8

Finnish Meteorological Institute Contributions 143
ISBN 978-952-336-044-0 (printed)
ISBN 978-952-336-045-7 (pdf)
ISSN 0782-6117

Images: The cover image presents a rimed ice crystal. Copyright belongs to Professor Kenneth G. Libbrecht. Printed with permission

Unigrafia Oy
Helsinki 2018

Finland

441 697
Printed matter

Author
Annakaisa von Lerber

Name of the doctoral dissertation
Challenges in measuring winter precipitation: Advances in combining microwave remote sensing and surface observations

Publisher School of Electrical Engineering

Unit Department of Electronics and Nanoengineering

Series Aalto University publication series DOCTORAL DISSERTATIONS 4/2018

Field of research Space Science and Technology

Manuscript submitted 17 December 2017 **Date of the defence** 1 February 2018

Permission to publish granted (date) 13 November 2017 **Language** English

☐ **Monograph** ☒ **Article dissertation** ☐ **Essay dissertation**

Abstract

Globally, snow influences Earth and its ecosystems in several ways by having a significant impact on, e.g., climate and weather, Earth radiation balance, hydrology, and societal infrastructures. In mountainous regions and at high latitudes snowfall is vital in providing freshwater resources by accumulating water within the snowpack and releasing the water during the warm summer season. Snowfall also has an impact on transportation services, both in aviation and road maintenance.

Remote sensing instrumentation, such as radars and radiometers, provide the needed temporal and spatial coverage for monitoring precipitation globally and on regional scales. In microwave remote sensing, the quantitative precipitation estimation is based on the assumed relations between the electromagnetic and physical properties of hydrometeors. To determine these relations for solid winter precipitation is challenging. Snow particles have an irregular structure, and their properties evolve continuously due to microphysical processes that take place aloft. Hence also the scattering properties, which are dependent on the size, shape, and dielectric permittivity of the hydrometeors, are changing.

In this thesis, the microphysical properties of snowfall are studied with ground-based measurements, and the changes in prevailing snow particle characteristics are linked to remote sensing observations. Detailed ground observations from heavily rimed snow particles to open-structured low-density snowflakes are shown to be connected to collocated triple-frequency signatures.

As a part of this work, two methods are implemented to retrieve mass estimates for an ensemble of snow particles combining observations of a video-disdrometer and a precipitation gauge. The changes in the retrieved mass-dimensional relations are shown to correspond to microphysical growth processes. The dependence of the C-band weather radar observations on the microphysical properties of snow is investigated and parametrized. The results apply to improve the accuracy of the radar-based snowfall estimation, and the developed methodology also provides uncertainties of the estimates. Furthermore, the created data set is utilized to validate space-borne snowfall measurements.

This work demonstrates that the C-band weather radar signal propagating through a low melting layer can significantly be attenuated by the melting snow particles. The expected modeled attenuation is parametrized according to microphysical properties of snow at the top of the melting layer.

Keywords remote sensing, radar, snowfall, precipitation microphysics, surface observations

ISBN (printed) 978-952-60-7790-1 **ISBN (pdf)** 978-952-60-7791-8

ISSN-L 1799-4934 **ISSN (printed)** 1799-4934 **ISSN (pdf)** 1799-4942

Location of publisher Helsinki **Location of printing** Helsinki **Year** 2018

Pages 276 **urn** http://urn.fi/URN:ISBN:978-952-60-7791-8

Tekijä
Annakaisa von Lerber

Väitöskirjan nimi
Edistysaskelia lumi- ja räntäsateiden mittaamisessa yhdistämällä kaukokartoitus- ja pintahavaintoja

Julkaisija Sähkötekniikan korkeakoulu

Yksikkö Elektroniikan ja nanotekniikan laitos

Sarja Aalto University publication series DOCTORAL DISSERTATIONS 4/2018

Tutkimusala Avaruustiede ja -tekniikka

Käsikirjoituksen pvm 17.12.2017 **Väitöspäivä** 01.02.2018

Julkaisuluvan myöntämispäivä 13.11.2017 **Kieli** Englanti

☐ **Monografia** ☒ **Artikkeliväitöskirja** ☐ **Esseeväitöskirja**

Tiivistelmä

Lumi vaikuttaa maapallon ilmastoon, ekosysteemeihin, säteilytasapainoon ja hydrologiseen kiertoon. Vuoristoisilla alueilla sekä pohjoisessa lumisade kerryttää elintärkeitä makean veden varantoja, ja se voi vaikeuttaa sekä maa- että lentoliikennettä.

Kaukokartoitusinstrumentit, kuten tutkat ja radiometrit, mahdollistavat sateen havainnoinin maailmanlaajuisesti suurella paikallisella ja ajallisella tarkkuudella. Mikroaaltokaukokartoituksessa sateen mittaaminen perustuu havaitun sadepisaran tai lumihiutaleen sähkömagneettisten ja fysikaalisten ominaisuuksien välisen riippuvuuden mallintamiseen. Lumi-ja räntäsateesta kertyvän sademäärän arvioiminen on haastavaa. Lumikiteet ja -hiutaleet ovat muodoltaan epäsäännöllisiä ja niiden ominaisuudet muotoutuvat jatkuvasti ilmakehässä eri mikrofysikaalisissa prosesseissa. Näin ollen, sirontaominaisuudet, jotka ovat riippuvaisia kohteen koosta, muodosta ja sähköisestä permittiivisyydestä, muuttuvat ja vaihtelevat hetkestä ja tilanteesta toiseen.

Tässä työssä lumisateen mikrofysikaalisia ominaisuuksia on tutkittu maan pinnalla olevilla laitteilla, ja havaitut muutokset ominaisuuksissa on yhdistetty kaukokartoitusmittauksiin. Tarkkoja havaintoja erilaisista lumihiutaleista, niin vahvasti huurtuneista lumirakeista kuin avoimen rakenteen omaavista lumihiutaleista, on yhdistetty kolmitaajuustutkamittauksissa havaittujen ominaisuuksien kanssa.

Työssä on toteutettu kaksi eri menetelmää lumihiutaleiden massan tai tiheyden määrittämiseen yhdistäen automaattisia disdrometri- ja sademittarihavainnointoja. Lumihiutaleiden massa-koko -suhteen muutokset on osoitettu olevan yhteydessä ilmakehässä havaittaviin lumihiutaleen kasvutapoihin. Näitä massa-koko -suhdemuutoksia on tutkimuksessa hyödynnetty myös C-taajuusalueen tutkahavaintojen tulkinnassa, ja tutkahavaintojen riippuvuutta lumisateen mikrofysikaalisien ominaisuuksien osalta on tutkittu ja parametrisoitu. Tulosten avulla lumisateen määrää voidaan säätutkalla arvioida tarkemmin ja määrittää virherajat arvioidulle sademäärälle. Tutkimuksessa luotua aineistoa on edelleen käytetty satelliittipohjaisen lumisadetuotteen validoinnissa.

Tässä työssä on myös osoitettu, että lähellä maanpintaa olevan sulamiskerroksen aiheuttava vaimennus C-taajuusalueella toimivalle säätutkalle on merkittävä. Vaimennuksen suuruus on mallinnuksen avulla yhdistetty lumen mikrofysikaalisiin ominaisuuksiin sulamiskerroksen yläpuolella.

Avainsanat kaukokartoitus, tutka, lumisade, sateen mikrofysiikka, pintahavainnot

ISBN (painettu) 978-952-60-7790-1 **ISBN (pdf)** 978-952-60-7791-8

ISSN-L 1799-4934 **ISSN (painettu)** 1799-4934 **ISSN (pdf)** 1799-4942

Julkaisupaikka Helsinki **Painopaikka** Helsinki **Vuosi** 2018

Sivumäärä 276 **urn** http://urn.fi/URN:ISBN:978-952-60-7791-8

Preface

It was a long lesson to learn. At times, the completion of my doctoral studies seemed an unreachable goal. Obviously, I could not have achieved this without guidance and support from people more knowledgeable and experienced than me. I own a deep gratitude to these people for sacrificing all the time and effort to help me on my academical path.

I would like to thank Prof. Tuija Pulkkinen for agreeing to act as my supervisor. Her guidance on academic work has been practical and encouraging. I feel privileged that Prof. Herman Russchenberg took the task of reviewing my thesis and acting as the official opponent at the public defense. I'm also grateful to both of my pre-examiners Dr. Wanda Szyrmer and Dr. Sergey Matrosov for their evaluation of the thesis. I truly appreciate their constructive comments and suggested improvements.

I wish to express a sincere gratitude to my advisor Prof. Dmitri Moisseev. Frankly, this work would never have finished without his guidance and support. He introduced me into the field of radar meteorology and has patiently advised forward. He has created an inspiring research atmosphere within his group at the University of Helsinki (UH) and I'm grateful that he offered opportunities to participate in international collaboration. I also would like to thank my other advisor Prof. V. Chandrasekar for the valuable comments and fruitful discussions. These often had a pivotal effect on my work. I wish to acknowledge the cooperation with international colleagues, Dr. Walter Petersen, Dr. Stefan Kneifel, Prof. Pavlos Kollias, Dr. Davide Ori, Dr. David A. Marks, Prof. Ali Tokay and Dr. Larry F. Bliven, with whom I have had the pleasure of co-authoring journal articles as a part this thesis work.

I have always had a benefit to work in a supporting and inspiring environment. I'm thankful to Prof. Jouni Pulliainen and Prof. Emeritus Martti Hallikainen, for initially acting as my advisor and supervisor, respectively.

Since 2013 I have been working in Finnish Meteorological Institute (FMI). I'm truly grateful to my bosses Dr. Ari-Matti Harri and M.Sc. Jarmo Koistinen for generously providing resources and encouragement to finish my studies. Financially this work has partly been supported by the Doctoral school of Aalto University School of Electrical Engineering, grant of the Vilho, Yrjö and Kalle Väisälä Foundation, Horizon 2020 grants No 699221 (PNOWWA) and No 700099 (ANYWHERE). These are gratefully acknowledged.

The colleagues both in Aalto and FMI have played an important role throughout my academic career. Not only by helping me on the way, but also by creating a pleasant and friendly atmosphere. From my time in Aalto University, I would especially like to thank co-workers Jaan, Jaakko, Pauli, Pekka, Afroza, and Jan. From FMI I would like to thank fellows in Tutkatiimi, and present and former colleagues, especially mentioning Jani, Jussi L., Pekka, Larissa, Osku, Seppo, Timo, and Terhi. Special thanks belong to Dr. Elena Saltikoff, who has been my unofficial mentor in snowfall studies and beyond, and to Dr. Mark Paton for proof-reading my manuscripts. As adopted to the UH radar group, I have enjoyed working with Jussi T., Laura, Susanna, Brandon, Haoran, Marta, Roberto, Lorenzo, and Kalle. I would also like to acknowledge M.Sc. Matti Leskinen, for patiently teaching about many aspects of practical measurements. For the peer-support and enjoyable lunch breaks, I would like to thank among others Päivi, Hannakaisa, Anu-Maija, Laura, and Daniela.

Luckily, there is more to life than Ph.D. studies. I'm happily surrounded by a wonderful group of friends and family, with whom I can share the joys and sorrows. I thank you all for being there for me! For my parents, Eliisa and Juhani Rinne, I'm deeply grateful for giving me such a great start in this life, and encouraging me to pursue towards my dreams. To my husband, Tuomo, for his loving support, I am thankful more than I can express with words. For our dear children, Milja, Elina, Julia, and Joonas, I'm blessed to share life with you. All those moments are precious to me.

Helsinki, December 26, 2017,

Annakaisa von Lerber

Contents

List of Publications

This thesis consists of an overview and of the following publications which are referred to in the text by their Roman numerals.

I von Lerber, A., Moisseev, D., Leinonen, J., Koistinen, J. and Hallikainen, M.. Modeling radar attenuation by a low melting layer with optimized model parameters at C-band. *IEEE Transactions on Geoscience and Remote Sensing*, vol.53, no.2, pp.724-737, doi:10.1109/TGRS.2014.2327148, 2015 .

II Kneifel, S., von Lerber, A., Tiira, J., Moisseev, D., Kollias, P. and Leinonen, J.. Observed relations between snowfall microphysics and triple-frequency radar measurements. *Journal of Geophysical Research: Atmospheres*, vol.120, no.12, pp.6034-6055, doi:10.1002/2015JD023156, 2015 .

III Tiira, J., Moisseev, D.N., von Lerber, A., Ori, D., Tokay, A., Bliven, L.F. and Petersen, W.. Ensemble mean density and its connection to other microphysical properties of falling snow as observed in Southern Finland. *Atmospheric Measurement Techniques*, vol.9, no.9, pp.4825-4841, doi:10.5194/amt-9-4825-2016, 2016 .

IV von Lerber, A., Moisseev, D., Bliven, L.F., Petersen, W., Harri, A.-M. and Chandrasekar, V.. Microphysical properties of snow and their link to $Z_e - S$ relations during BAECC 2014. *Journal of Applied Meteorology and Climatology*, vol.56, no.6, pp.1561-1582, doi:10.1175/JAMC-D-16-0379.1, 2017 .

V von Lerber, A., Moisseev, D., Marks, D.A., Petersen, W., Harri, A.-M. and Chandrasekar, V.. Validation of GMI snowfall observations by using a combination of weather radar and surface measurements. Accepted for publication in *Journal of Applied Meteorology and Climatology*, doi:10.1175/JAMC-D-17-0176.1, 2017 .

Author's Contribution

Publication I: "Modeling radar attenuation by a low melting layer with optimized model parameters at C-band"

In Publication I, a melting layer model is utilized to optimize the attenuation correction in a melting layer based on microphysical properties of snow at the top of the melting layer. The author implemented the model, derived the optimized factors, and demonstrated the attenuation of the melting layer close to the ground with a case study at C-band. The author wrote the most of the article.

Publication II: "Observed relations between snowfall microphysics and triple-frequency radar measurements"

In Publication II, the triple-frequency radar signatures in snowfall are compared with the co-located ground observations. The author provided and performed the analysis of the ground observation data with Jussi Tiira, and contributed to the writing of the journal.

Publication III: "Ensemble mean density and its connection to other microphysical properties of falling snow as observed in Southern Finland"

In Publication III, the ensemble mean density of snowfall is derived using observations of video-disdrometer and precipitation gauge. The connection of the derived density to snow ratio, fall velocity-dimensional relation and particle size distribution parameters are investigated. The author participated in the analysis of data, e.g. computing the snow ratios,

estimating the dimension correction and defining the $m(D)$ relations, and contributed to the writing of the journal.

Publication IV: "Microphysical properties of snow and their link to $Z_e - S$ relations during BAECC 2014"

In Publication IV, mass-dimensional relations in snowfall are retrieved based on the general hydrodynamic theory and changes in them are investigated related to microphysical processes of snow. Also, the dependence of the equivalent reflectivity factor and snowfall rate on snow microphysics is studied. The author implemented the retrieval method, performed processing and analysis of data, and mainly wrote the article text.

Publication V: "Validation of GMI snowfall observations by using a combination of weather radar and surface measurements"

In Publication V, the quantitative snowfall estimates of rate and accumulation are computed by applying event-specific relations between the equivalent reflectivity factor and snowfall rate to weather radar observations, and the uncertainties of the rate estimates are determined. The data set is applied to validate space-borne NASA GPM Microwave Imager (GMI) snowfall product. The GMI data are provided by D.A. Marks, otherwise, the data processing and analysis are mainly performed by the author. The majority of the journal paper is written by the author.

List of Abbreviations

ADDA	Amsterdam Discrete Dipole Approximation software (C-code)
AMSU-B	Advanced Microwave Sounding Unit-B
ATMS	Atmospheric Technology Microwave Sounder
BAECC	Biogenic Aerosols Effects on Clouds and Climate campaign
BSA	BackScatter Alignment
C	Frequency band, 4 to 8 GHz, λ = 7.5 to 3.8 cm
CCD	Charged Coupled Device
CCN	Cloud Condensation Nuclei
CDF	Cumulative Distribution Function
CDM	Coupled Dipole Method
CG-FFT	Conjugate Gradient-Fast Fourier Transform
CGM	Conjugate Gradient Method
CPI	Cloud Particle Imager
CPR	Cloud Profiling Radar
CPU	Central Processing Unit
CRM	Cloud Resolving Model
CSI	Critical Success Index
1D	one-dimensional
2D	two-dimensional
3D	three-dimensional
DDA	Discrete Dipole Approximation
DDSCAT	Discrete Dipole Scattering software (Fortran code)
DFIR	Double Fence International Reference
DGF	Digitized Green's Function method
2D-P	2D- Precipitation optical array probe
DPR	Dual-frequency Precipitation Radar
2DVD	2D-Video Disdrometer
DWR	Dual-Wavelength Ratio

EEMA	Extended Effective Medium Approximation
EMA	Effective Medium Approximation
FAR	False Alarm Rate
FDTD	Finite Difference Time Domain method
FMI	Finnish Meteorological Institute
FSA	Forward Scatter Alignment
GMI	GPM Microwave Imager
GMM	Generalized Multiparticle Mie method
GPM	Global Precipitation Measurement mission
GPROF	Goddard PROFiling algorithm
HCA	Hydrometeor Classification Algorithm
HHI	Holographic Hydrometeor Imager
HSS	Heidke Skill Score
HVSD	Hydrometeor Velocity and Shape Detector
IKA	FMI Ikaalinen weather radar
IN	Ice Nuclei
ITU	International Telecommunication Union
JWD	Joss-Waldvogel Disdrometer
Ka	Frequency band, 27 to 40 GHz, λ = 1.1 to 0.75 cm
Ku	Frequency band, 12 to 18 GHz, λ = 2.5 to 1.67 cm
LWE	Liquid Water Equivalent
LWP	Liquid Water Path
MASC	Multi-Angle Snowflake Camera
MG	Maxwell Garnett mixing rule
MHS	Microwave Humidity Sounder
MRMS	Multi-Radar-Multi-Sensor precipitation product of NOAA
NCEP	National Centers for Environmental Prediction
NEXRAD	NEXt-Generation RADar
NOAA	National Oceanic and Atmospheric Administration
NWP	Numerical Weather Prediction
QPE	Quantitative Precipitation Estimate
PARSIVEL	PARticle SIze VELocity disdrometer
PDF	Probability Density Function
PIP	Particle Imaging Package
POD	Probability Of Detection
PPI	Plan Position Indicator
PR	TRMM Precipitation Radar
PSD	Particle Size Distribution

RGA	Rayleigh-Gans Approximation
RHI	Range Height Indicator
RMSE	Root Mean Squared Error
S	Frequency band, 2 to 4 GHz, λ = 15 to 7.5 cm
SPICE	Solid Precipitation InterComparison Experiment
SSRGA	Self-Similar Rayleigh – Gans Approximation
SVI	Snowflake Video Imager
SVM	Separation of Variables Method
Swerad	SWEdish ground-based RADar network
TMI	TRMM Microwave Imager
TMM	T-Matrix Method
TRMM	Tropical Rainfall Measuring Mission
TWR	Triple-Wavelength Ratio
UHF	Ultra High Frequency, 0.3 to 3 GHz, λ = 100 to 10 cm
U.S.	the United States
VIEF	Volume Integral Equation Formulation
VPR	Vertical Profile Reflectivity
W	Frequency band, 75 to 110 GHz, λ = 0.40 to 0.27 cm
WMO	World Meteorological Organization
X	Frequency band, 8 to 12 GHz, λ = 3.8 to 2.5 cm

List of Symbols

$\mathbf{a}$	incident field terms of TMM
a_0	coefficient in turbulence correction
a, b, c, d	hits, false alarms, misses, correct rejections of a 2×2 contingency table
a_d	prefactor of the $\rho(D)$ relation
$a_{ds,dms}$	prefactor of the $\rho(D)$ relation in snow, melting snow
a_m	prefactor of the $m(D)$ relation
$a_{ms,mms,mr}$	prefactor of the $m(D)$ relation in snow, melting snow, rain
a_n	Mie scattering coefficient
a_v	prefactor of the $v(D)$ relation
$a_{vs,vms}$	prefactor of the $v(D_s)$ relation in snow, melting snow
$a^r_{vs,vms,vr}$	prefactor of the $v(D_r)$-relation in snow, melting snow, rain
a_x	axis ratio of a spheroid
$a_{xs,xms,xr}$	axis ratio of a snow, melting snow, rain particle
a_{zr}	prefactor of the $Z - R$ relation
a_{zs}	prefactor of the $Z_e - S$ relation
A	cross-sectional area
A, B, C, D	constants in a relation of the imaginary part of dielectric permittivity of ice
$A(D)$	area-dimensional relation
A_e	area normal to the flow
A_{eff}	effective area of antenna
A_g	geometric cross-sectional area
$A_{h,v,dr}$	horizontal, vertical, differential attenuation
A_m	constant in approximate formula for F_{ms} in (Szyrmer and Zawadzki, 1999)
$A_\perp$	area of the smallest circle or ellipse, which contains all of the A_e
A_r	area ratio

A_{tot}	total area ratio of a measured particle
b_0	coefficient in turbulence correction
b_d	exponent of the $\rho(D)$ relation
$b_{ds,dms}$	exponent of the $\rho(D)$ relation in snow, melting snow
b_m	exponent of the $m(D)$ relation
$b_{ms,mms,mr}$	exponent of the $m(D)$ relation in snow, melting snow, rain
b_n	Mie scattering coefficient
b_v	exponent of the $v(D)$ relation
$b_{vs,vms}$	exponent of the $v(D_s)$ relation in snow, melting snow
$b^r_{vs,vms,vr}$	exponent of the $v(D_r)$ relation in snow, melting snow, rain
b_{zr}	exponent of the $Z - R$ relation
b_{zs}	exponent of the $Z_e - S$ relation
B_m	constant in approximate formula for F_{ms} in (Szyrmer and Zawadzki, 1999)
c	speed of light
c_d	exponent of the melting snow drag coefficient relation in Yokoyama and Tanaka (1984)
c_g	factor in the description of melting snow fall velocity in Szyrmer and Zawadzki (1999)
C_0	pressure drag coefficient
C_c	capacitance factor of a particle
$C_{ci,cs,cms,cr}$	capacitance factor of a ice, snow, melting snow, rain particle
C_d	drag coefficient
$C_{ds,dms,dr}$	drag coefficient of a snow, melting snow, rain particle
C_r	radar constant
d	inter-dipole separation
d_f	fractal dimension
d_{max}	diameter of the largest cloud droplet
D	diameter
D_0	median volume diameter
$D_{i,s,ms,r}$	diameter of a ice, snow, melting snow, rain particle
D_m	mass-weighted mean diameter
D_{max}	maximum observed diameter
D_{veq}	volume equivalent diameter
D_v	water vapor diffusivity in air at 0°C, $2.11\dot{1}0^{-}2\mathrm{m}^2\mathrm{s}^{-1}$
$DWR_{\lambda_1/\lambda_2}$	Dual-wavelength ratio between reflectivity factors at wavelengths λ_1 and λ_2
$\bar{e}_{i,s}$	electric field unit vector into incident, scattered direction

$e_{sat,w,i}$	saturation vapor pressure over water, over ice
E	collection efficiency
$\bar{E}$	electric field
E_0	electric field amplitude
E_{agg}	aggregation efficiency
$\bar{E}^{inc,int,s,tot}$	incident, internal, scattered, total electric field
E_r	field ratio
f	frequency
$f(\bar{k}_s, \bar{k}_i)$	scattering amplitude
f_m	melted mass fraction
f_{rim}	degree of riming
f_V	volume fraction
F	ventilation factor for vapor and heat diffusion
$F_{s,ms,r}$	ventilation factor for vapor and heat diffusion in snow, melting snow, rain
g	gravitational acceleration, 9.81 ms^{-1}
g_{diff}	heat transferred by conduction
g_v	factor describing the changes of snow particle terminal velocity in melting in (Szyrmer and Zawadzki, 1999) or (Battaglia et al., 2003)
G	LWE precipitation accumulation
$\bar{\bar{G}}_0$	dyadic Green's function
G_t	antenna gain
h	height
$\bar{h}$	horizontal component, also as subscript h
$\bar{h}_n^1$	spherical Hankel function of the first kind
h_{max}	experimental melting layer thickness
$\bar{H}$	magnetic field
$\bar{H}^{inc,int,s,tot}$	incident, internal, scattered, total magnetic field
$\bar{\bar{I}}$	unit dyad
j	imaginary unit
$\bar{j}$	Bessel function of the first kind
$\bar{J}$	electric current
k	wavenumber, number
k_0	wavenumber in vacuum
k_a	thermal conductivity of air at 0°C, $2.4 \times 10^{-2}\mathrm{Jm}^{-1}\mathrm{s}^{-1}\mathrm{K}^{-1}$
$\bar{k}_{i,s}$	wavenumber vector into incident,scattered direction
K	dielectric factor

K_{dp}	specific differential phase
$K_{i,p,s,w}$	dielectric factor of ice, snow, particle, water
L	length parameter
L_{at}	atmospheric attenuation
LDR	Linear Depolarization Ratio
L_f	latent heat of fusion at 0°C, 334Jg^{-1}
L_v	latent heat of vaporization at 0°C, 2500Jg^{-1}
m	mass
$m(D)$	mass-dimensional relation
$\bar{m}_{lmn}^{(k)}$	spherical wave function, kth kind of Bessel function, l is even or odd of sinusoidal function, m and n are number of terms in cos- and sin-functions
$m_{s,ms,r}$	mass of snow, melting snow, rain particle
$\bar{M}$	magnetic current
M_w	molecular weight of water, 18 gmol^{-1}
n, N	number
N_0	intercept parameter of exponential or gamma distribution
$N(D)$	particle size distribution
$\bar{n}_{lmn}^{(k)}$	spherical wave function, kth kind of Bessel function, l is even or odd of sinusoidal function, m and n are number of terms in cos- and sin-functions
$N_{s,ms,r}()$	particle size distribution in snow, melting snow, rain
N_t	total particle concentration
N_w	intercept parameter of normalized gamma distribution
p	perimeter of a particle
$\mathbf{p}$	scattered field terms of TMM
$\bar{p}$	dipole moment
$P_{a,s}$	absorbed, scattered power
$\bar{P}_n^1$	Legendre function of the first kind
$P_{r,t}$	received, transmitted power
r	radius of a particle
$\bar{r}, \bar{r}'$	range vector
$r_{a,b}$	radius of a particle along axis a or b
R	rain rate, distance in far-field
R_e	Reynolds number
RH	relative humidity in %
R_v	ideal gas constant, 8.314 Jmol^{-1}K^{-1}
S	snowfall rate

$S_f(\bar{k}_s, \bar{k}_i)$	form factor of RGA
S_h	Sherwood number
$\bar{S}^{inc,s}$	incident, scattered directional energy flux density, Poynting vector
S_r	snow ratio
t	time
T	temperature
$\mathbf{T}$	T-matrix
T_0	temperature on a particle surface
T_∞	temperature of surrounding air
T_w	wet-bulb temperature
u	dimensionless form factor corresponding inclusion shape
U	volume flux
v	terminal fall velocity of a particle
$\bar{v}$	vertical component, also as subscript v
v_∞	observed fall velocity of particle
v_a	vertical velocity of air
$v_{s,ms,r}$	terminal fall velocity of snow, melting snow and rain particle
$v(D)$	velocity-dimensional relation
v_Z	reflectivity-weighted fall velocity
V	volume of a particle
V_{rdr}	measurement volume of a radar
$V_{s,ms,r}$	volume of a snow, melting snow, rain particle
x	size parameter
X_b	Best number
x, y, z, X, Y, Z	axis of Cartesian coordination
Z	reflectivity factor
Z_{dr}	differential reflectivity factor
Z_e	equivalent reflectivity factor
$Z - R$	reflectivity factor - rain rate relation
$Z_e - S$	equivalent reflectivity factor - snowfall rate relation
α	eccentricity of spheroid
α_k	polarizability of kth dipole
$\Gamma()$	complete gamma function
δ	inclusion size
δ_0	boundary layer thickness
δ_{hv}	backscatter differential phase
$\Delta\delta_{s,ms,r}$	orientation of a snow, melting snow, rain particle

ϵ	permittivity
ϵ_0	permittivity in vacuum, $8.8542 \cdot 10^{-12}$ As/Vm
ϵ_∞	high-frequency permittivity
ϵ_{eff}	effective permittivity
ϵ_r	relative permittivity
$\epsilon_{i,s,ms,w}$	relative permittivity of ice, snow, melting snow, water
$\epsilon_{ic,mt}$	permittivity of inclusion, matrix medium
ϵ_{st}	low-frequency or static permittivity
η	wave impedance
η_a	dynamic viscosity of air at 0°C, $\eta_a = \nu_a \rho_a$
θ	elevation angle
λ	wavelength
Λ	slope parameter of gamma distribution
μ	shape parameter of gamma distribution, permeability
μ_0	permeability in vacuum, $4\pi \cdot 10^{-7}$ Vs/Am
μ_s	permeability of snow
ν_a	kinematic viscosity of air at 0°C, 0.1346cm^{2}s^{-1}
ρ	density
$\rho_{a,i,s,ms,w}$	density of air, ice, snow, melting snow, water
$\rho(D)$	density-diameter relation
$\rho(D_0)$	density - median volume diameter relation
ρ_{hv}	correlation coefficient
$\sigma_{a,b,e,s}$	absorption,backscattering, extinction, scattering cross-section
τ	relaxation time, pulse length
ϕ	azimuthal angle
χ	heat transfer coefficient
$\psi_{a,b,c}$	depolarization factors of a spheroid
$\Psi_{a,b,c}$	factors related to $\psi_{a,b,c}$
ω	angular frequency
Ω	total spheroidal surface area
Ω_s	solid angle

1. Introduction

"Don't bother me with high and low
with model runs and upper flow.
The only thing I want to know
is: Will it snow, yes or no?"

Freely adapted from Prof. of Meteorology Herfried Hoinkes, Innsbruck 1970.

The modern society is increasingly vulnerable to hazards caused by severe weather events, heavy snowfall being one of them. The preparation and mitigation actions for reducing the losses caused by winter storms are economically significant. A good example is aviation, where the exact timing, the expected amount and type of snowfall is an important knowledge in mid and high latitudes. Snowfall affects visibility conditions, rerouting of flights, airport maintenance services, and deicing activities. Also, road traffic maintenance in cities and counties must be prepared for snow storms, for keeping the streets and highways safe for commuting citizens and ground transportation. In Finland every year thousands of households are without electricity, sometimes even for days, when the weight of accumulated snow breaks tree branches over electric power lines and in unfortunate cases the building roofs collapse under the snow load. At higher latitudes and mountainous regions, the accumulated snowpack through winter precipitation is vital for providing a large proportion of the freshwater resources required for many communities throughout the world.

Globally, precipitation acts as a significant coupling between Earth's water, energy and biogeochemical cycles (Hou et al., 2014; Skofronick-Jackson et al., 2015). Storage, transport, and release of latent heat associated with

cloud formation and precipitation processes constitute about 75% of the heat energy of the atmosphere and at high-latitudes and polar regions more than 25% of precipitation falls in the form of snow (Field and Heymsfield, 2015). Schiermeier (2010) stated that the precipitation is one of the most significant gaps in climate change studies. One of the reasons for the insufficiently understood cloud and precipitation systems is the lack of comprehensive observations in different climate regimes (Stephens and Kummerow, 2007).

Continuous monitoring of winter precipitation, both at local and global scales, is essential for the scientific research of winter weather. Remote sensing instrumentation plays a key role for the needed coverage. In this work, remote sensing instruments operating in the microwave region from 5 GHz to 183 GHz were used, with the corresponding wavelengths ranging from centimeters to millimeters. The microwave region is optimal for observing precipitation and clouds. In this region, the sensors are sensitive to the hydrometeor-sized particles, but the transmissivity of the atmosphere is still high for detecting objects at long distances. Remote sensing observations can cover large areas. For ground based radars the distance can be hundreds of kilometers, and the range is limited more by the curvature of Earth and vertical structure of precipitation, and not by the technology. The temporal and spatial resolution of a weather radar network is superior compared to e.g. a network of the traditional surface instruments such as precipitation gauges. In addition to large scale observations, radars can also obtain a 3D-state of the lower atmosphere providing information on the vertical structure of precipitating systems. Ground-based remote sensing instruments are usually located in populated areas because of the required infrastructure. On a global scale, satellite observations are needed to cover the oceans and rural areas (Kidd and Levizzani, 2011).

In remote sensing, the primary task is to solve the properties of the object by extracting them from the parameters that can be measured with the instrument, in this case, from observations of electromagnetic radiation. This is called an inverse problem, where the needed quantity must be inferred from its indirect manifestation. Thus it is necessary to establish relations between the properties of the object and the observed parameters. In remote sensing the needed relations are found by studying the interactions, i.e. scattering and absorption, of electromagnetic waves with the object and identifying the errors induced by other sources. This is

called forward modeling or solving the direct problem. When a connection is found, the inverse problem can be formulated (Logvin et al., 2002).

The snow particles consist of ice and air in elusive quantities in a complex structure, and thus electromagnetic scattering properties are challenging to be defined. As to a rain drop, a spheroid or sphere describes the true particle shape quite accurately. For snowflakes, more complicated models or approximations must be assumed causing uncertainty in remote sensing retrievals. Due to the differences in electromagnetic properties of ice and water in the microwave region, the scattering response of a dry snowflake to electromagnetic radiation is weaker than that of a water drop. Therefore, the power received at a remote sensing sensor from snowflakes is less than the backscattered power from same-sized water droplets (Rinehart, 1997). The scattering characteristics of melting snowflakes are even more complex as the scattering is highly sensitive to the amount of melted liquid present in a particle. Melting ice particles are important mainly as an error source in precipitation estimates and as a cause of signal attenuation on satellite links (Klaassen, 1990; Matrosov, 2008).

It is a challenge that many microphysically interesting quantities are not easily obtained from the remote sensing parameters. One way to constrain the inverse problem is the increase of measurements, e.g. by simultaneously measuring at several frequencies or polarizations. The algorithms in satellite-based precipitation estimates with passive instruments apply several frequency channels to distinguish the impact of different components of electromagnetic interactions on the observed radiation (Bennartz and Bauer, 2003). Also, adding more frequencies to radar measurements has shown to improve the derived snow particle properties (Matrosov, 1992; Kneifel et al., 2011). The size, location, and radial fall velocity of hydrometeors can be retrieved from single polarization radar observations, however, polarimetric observations are sensitive also to the shape and orientation of the hydrometeors, and can be utilized to discriminate the radar echoes of different objects (Bringi and Chandrasekar, 2001). Dual-polarization Doppler radars have been successfully used in hydrometeor classification algorithms (HCA) (Chandrasekar et al., 2013).

Surface measurements are essential when investigating microphysical processes and properties of winter precipitation. They are utilized in parameterizing quantities firstly for the forward modeling, and secondly for verifying remote sensing retrievals, and thirdly for the understanding how the microphysical processes are manifested in the remote sensing

observations. In the past, properties of individual snow particles were recorded manually (Locatelli and Hobbs, 1974). Although the observations were performed carefully, their representativity in temporal and spatial scale was poor. Automatic observations of snowfall are made using optical disdrometers, which typically measure particle size, fall velocity, particle size distribution and some description of a particle shape. Automatic observations offer the possibility to gather extensive data sets, but the complex structure of the snowflakes is challenging (Wood et al., 2013). At present, there is no instrument developed, which could observe the 3D-structure or measure the mass of a single snowflake. Gauges provide a physically direct measure of precipitation rate and often act as the ultimate reference. In many regions of the world, a network of precipitation gauges is the only measurement method available (New et al., 2001). However, gauges are also prone to errors, the main source of uncertainty being the under-catching of the precipitation, primarily caused by wind-induced turbulence over the gauge orifice, being most pronounced for snow measurements (Peterson et al., 1998).

This thesis focuses on the investigations of microphysical processes in winter precipitation and attempts to connect these processes to remote sensing observations. The starting point is to utilize surface observations, mainly performed with an optical disdrometer and a precipitation gauge. Two different methods are applied to retrieve the mass of the falling snow and are presented in Publication III and Publication IV. The changes of mass are linked to microphysical processes, namely aggregation and riming, and these are connected to signatures obtained from single- and triple-frequency radar observations shown in Publication IV and Publication II. The effect of microphysical parameterization to radar observations is studied. Improvements for estimation of radar-based snowfall rate are suggested in Publication IV and their feasibility is shown by validating the space-based radiometer snowfall rate as described in Publication V. The impact of parametrization of snow properties on the melting process is researched by combining the melting model with radar observations in Publication I. Based on the findings an attenuation correction for C-band weather radar measurements is suggested.

The studied microphysical properties of hydrometeors and main processes of winter precipitation are presented in Chapter 2. The surface instrumentation used in this research work are presented in Chapter 3, and the uncertainties of the different instruments are described and com-

pared. In Chapter 4 the basic concepts of the electromagnetic scattering theory are defined, and the background of the used methods and approximations applied in this work are presented. Remote sensing methodology is determined in Chapter 5. The main results of this thesis are summarized in Chapter 6, and the impact of the research work is evaluated and some future aspects are discussed in Chapter 7.

2. Microphysics of snow

"Snow crystals are the hieroglyphs sent from the sky."

Ukichiro Nakaya, Snow Crystals: Natural and Artificial, 1954

Ukichiro Nakaya was a Japanese physicist, who developed a technique for making the first artificial snow crystals in the 1930s. He studied how the growing conditions influence the snow crystal shape, and vice versa, how the snowflake structure can reveal different meteorological conditions aloft.

2.1 Microphysical parameters

Microphysical parameters describing snowfall are e.g. size, mass, shape and terminal velocity of a snow particle, and for an ensemble of snowflakes, particle concentration in a given volume. By examining these microphysical properties, the evolution and the interactions of hydrometeors governed by the atmospheric dynamics and thermodynamics can be investigated.

The definition of **dimension** for a non-spherical snow particle is ambiguous; often it is defined as the diameter of the circumscribing sphere, the mean diameter of maximum diameters in two orthogonal directions, disk- or volume-equivalent diameter. Different scientific communities have applied different definitions based on used measurement methodology. For instruments recording particles as images, the maximum diameter defined from the circumscribing sphere e.g. in (Mitchell, 1996; Heymsfield et al., 2004; Heymsfield and Westbrook, 2010) and (Publication IV, Publication V) or the disk-equivalent diameter e.g. in (Heymsfield et al., 2002) and (Publication III) is a common practice. Instruments, which observe par-

ticles by taking images from multiple angles have a broader view on the particle shape. In these studies, the diameter is typically an approximation of the volume-equivalent diameter e.g. in (Brandes et al., 2007; Wood et al., 2013; Huang et al., 2015). The limited observation geometry produces uncertainty also on the parameters derived from the dimension such as mass, velocity or reflectivity factor. The uncertainty between the observed dimensions relative to the true dimensions of the particle are estimated e.g. in (Schefold, 2004; Szyrmer and Zawadzki, 2010; Schmitt and Heymsfield, 2010; Wood et al., 2013) and also discussed in Publication IV.

Given the need to define properties of an ensemble of particles with different dimensions, properties such as **mass** and **fall velocity** are usually defined in the power-law format. Format is an approximation, but it is shown to work well in many cases. However, there is evidence that a single set of power-law factors may not be representative for the complete range of sizes e.g. (Mitchell, 1996; Mitchell and Heymsfield, 2005; Khvorostyanov and Curry, 2005; Schmitt and Heymsfield, 2009; Cotton et al., 2013; Szyrmer and Zawadzki, 2014; Erfani and Mitchell, 2016). The factors can be different for the smaller size regime than for the larger particles, and the different pair of factors are important for the lower and higher moments of the particle size distribution (Mitchell and Heymsfield, 2005; Szyrmer and Zawadzki, 2014).

For the mass-dimensional relation ($m(D)$), the power-law format is

$$m = a_m D^{b_m}, \tag{2.1}$$

where m is the mass in g, D is the defined diameter typically in cm, prefactor a_m is in gcm$^{-b_m}$ and exponent b_m has values between $0 < b_m \leq 3$. There are several studies, which determine the $m(D)$ relation for certain snow particle types e.g. (Magono and Nakamura, 1965; Locatelli and Hobbs, 1974; Mitchell et al., 1990; Mitchell, 1996; Brown and Francis, 1995; Heymsfield et al., 2004, 2007, 2010). Typically for fluffy low-density aggregates, the value of b_m is close to 2, and for denser particles such as graupel, it is close to 3. On the other hand, the prefactor a_m varies more than by a factor of ten between different particle types.

Terminal velocity is the constant velocity of a freely falling hydrometeor when the gravitational force pulling the particle downward is balanced with the slowing aerodynamic drag (Rinehart, 1997). The fall velocity depends on the particle shape and mass, as well as the density and viscosity of the atmosphere. Higher in the atmosphere, where the density of air is less than near the Earth's surface, the particles fall faster. Spheres and

other smooth particles fall faster than rougher particles of equal size, and dense particles fall faster than fluffier particles. The fall behavior of snow particles is driven by mass distribution in the particle and how the shape is exposed to the fall direction. Hydrometeors tend to fall in orientation by maximizing the drag, i.e. the maximum dimension of a snowflake is aligned horizontally. Because of the complex structure of snowflakes, the fall patterns can be unstable, and particles can swing or tumble while falling. The fall behavior of single crystals or snowflakes have been studied e.g. by (List and Schemenauer, 1971; Zikmunda and Vali, 1972; Zikmunda, 1972; Kajikawa, 1972; Cho et al., 1981; Heymsfield and Kajikawa, 1987; Garrett et al., 2015).

The fall velocity-dimensional $v(D)$ relation defined here in ms^{-1} is

$$v = a_v D^{b_v}. \tag{2.2}$$

For different snow particles, according to Locatelli and Hobbs (1974) the prefactor a_v varies around 0.62-1.5 $\mathrm{ms}^{-1}\mathrm{mm}^{b_v}$ and the exponent b_v is changing from 0.12 to 0.66.

The **particle size distribution** (PSD) expresses the number of particles per given size interval in a measurement volume. PSD parameter describes the population of the particles and also depends on prevailing microphysical processes, e.g. a wider distribution with large particles is expected for aggregation (Brandes et al., 2007). A gamma functional form is typically used to describe precipitation (Ulbrich, 1983)

$$N(D) = N_0 D^{\mu} \mathrm{exp}(-\Lambda D). \tag{2.3}$$

$N(D)$ is often expressed in $\mathrm{mm}^{-1}\mathrm{m}^{-3}$, where N_0 is the intercept parameter in $\mathrm{mm}^{-1-\mu}\mathrm{m}^{-3}$, D is the diameter in mm, μ is the shape parameter, and Λ is the slope parameter in mm^{-1}. For $\mu = 0$, Eq.(2.3) transforms to exponential distribution proposed by Marshall and Palmer (1948).

To estimate parameters of gamma distribution, the moment method of D can be applied and the nth moment can be expressed as

$$\langle D^n \rangle = \int_0^{\infty} D^n N(D) dD = N_0 \Lambda^{-(\mu+n+1)} \Gamma(\mu + n + 1), \tag{2.4}$$

where $\Gamma()$ is the complete gamma function. The zeroth moment defines the total particle concentration in m^{-3}

$$N_t = \int_0^{\infty} N(D) dD = N_0 \Lambda^{-(\mu+1)} \Gamma(\mu + 1). \tag{2.5}$$

Above, an analytical solution is obtained using the complete gamma function and the integration limits are set to infinity. In reality, the integral is

truncated from both directions. The moment method may also be defined on the truncated moments with incomplete gamma function, e.g. in (Mallet and Barthes, 2009; Kumar et al., 2011). The lower limit is larger than zero, because of the resolution threshold of the measuring instrument (Moisseev and Chandrasekar, 2007) and the top limit is usually constrained because the occurrence of large particles is not representative during the given integration time and instrumental limitations. The effect of truncation is discussed in e.g. (Ulbrich and Atlas, 1998) and the induced bias to the quantities of nth moment due to limited sample in e.g. (Smith and Kliche, 2005).

To describe a mean diameter of precipitating particles often either **mass-weighted mean diameter** (D_m) (Bringi and Chandrasekar, 2001)

$$D_m = \frac{\int_0^\infty Dm(D)N(D)dD}{\int_0^\infty m(D)N(D)dD}, \tag{2.6}$$

or the **median volume diameter** (D_0) are used (Bringi and Chandrasekar, 2001)

$$\int_0^{D_0} D^3 N(D)dD = \frac{1}{2}\int_{D_0}^\infty D^3 N(D)dD. \tag{2.7}$$

D_0 describes the diameter in a given volume such that half of the volume is contributed from particles smaller than D_0.

2.2 Snow growth processes

For snow particles, the evolution starts by ice nucleation and continues firstly by diffusional growth and secondly by the collection of other particles in aggregation and riming. At some point, the snow particle reaches the mass, where gravitational attraction is larger than the net force of the air buoyancy and updraft, and it will fall towards the ground. If the particle falls below the 0°C isotherm, it will melt and eventually change into raindrop before reaching the ground.

2.2.1 Ice nucleation

In cold clouds, where the temperature is below 0°C, ice and supercooled cloud droplets are often coexisting. Ice crystals can be formed from cloud water vapor by two pathways; vapor can deposit directly to the ice phase, or it first condensates to a liquid phase and then freezes. The latter is more common, only in extreme conditions at temperatures -100°C the

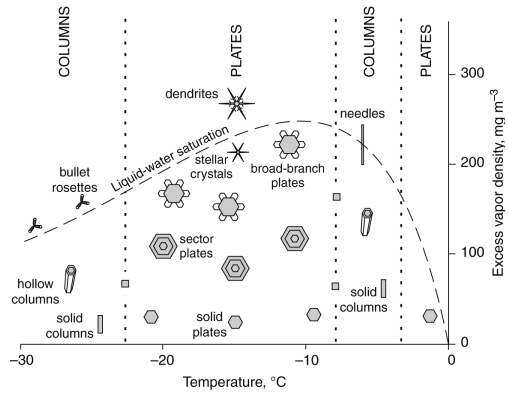

Figure 2.1. Morphology of snow crystals as a function of different temperature and supersaturation conditions. Photo credits: Lamb and Verlinde (2011) with permission.

direct way is more likely (Lamb and Verlinde, 2011). The freezing of a cloud droplet can either be triggered by aerosol particles acting as ice nuclei (IN) or occur homogeneously (without IN) below a temperature of $-38°$C (Pruppacher and Klett, 1997). For the homogeneous freezing, e.g. for micrometre-sized droplets at $-38°$C temperature, the required ice saturation ratio is 1.45 (Koop et al., 2000), and thus between $-38°$C and $0°$C ice crystals are more likely formed by heterogeneous nucleation. Suitable INs are solid, water-insoluble particles e.g. desert and agricultural dust, biogenic particles with some bacteria and fungi, soot and sulfate particles (Hoose and Möhler, 2012). The number concentration of cloud condensation nuclei (CCN) is usually much higher than the IN concentration, and one of the important scientific questions has been to explain the observed high number of ice particles relative to the smaller number of INs. Both the homogeneous and heterogeneous nucleations are considered as primary ice production processes, and the high amount of ice particle have been explained by secondary ice production (Field et al., 2017). Several mechanisms have been proposed, e.g. rime splintering, shattering of freezing large supercooled drops, fragmentation of delicate ice crystals in ice to ice particle collisions (Hallett and Mossop, 1974; Rangno and Hobbs, 2001; Yano and Phillips, 2011; Rangno and Hobbs, 2005; Lawson et al., 2015).

2.2.2 Growth by vapor deposition

The ambient temperature mainly defines whether the crystal grows into plate-like or columnar form, in any case, because of the molecular structure

of water, the ice crystals usually have hexagonal symmetry. The humidity conditions influences the complexity of the snow crystal. A snow crystal morphology diagram, also called a Nakaya Diagram, shown in Figure 2.1, presents the humidity and temperature regimes for a certain snow crystal habit. Thin plates grow around a temperature of -2°C, while columns and needles appear near -5°C. Larger stellar-like plates and dendrites form near -15°C. The vapor growth is a nonlinear process, which dynamics is typically dominated by attachment kinetics in combination with two transport effects: particle diffusion, which carries water molecules to the growing crystal, and heat diffusion, which removes latent heat generated by solidification (Libbrecht, 2005). The process is sensitive to small changes in temperature, supersaturation, and other factors; hence there is substantial variability in crystal sizes and shapes even though crystals would have grown under fairly similar conditions (Libbrecht, 2005). The deposition of vapor on the surface of the ice crystal is following the vapor concentration gradients. In low supersaturations, the gradients are relatively weak, and the crystal shape follows the underlying crystallography. At high supersaturations, stronger radial gradients are present, and vapor gradients conduct the deposition growth to the protruding crystal features (Lamb and Verlinde, 2011).

Because of the lower equilibrium vapor pressure of ice compared to the one of water, in mixed-phased clouds, ice particles grow faster than cloud droplets and consume the available vapor. If the vapor is taken up by ice particles more rapidly than can be supplied by uplift, supersaturation with respect to water drops below zero and the droplets evaporate and are consumed by the ice particles. The growth of ice particles in the presence of liquid water is called the Wegener-Bergeron-Findeisen process. The deposition growth takes from 15 minutes to an hour, and the diameter of snow crystals varies from 10 μm at the top of the cloud to centimeter scale towards the bottom of the cloud (Baran, 2012). The initial growth from the vapor gathers more and more mass onto the snow crystal, and it is increasingly affected by the gravitational attraction and starts to fall. A falling particle will interact with other particles and through interaction with other particles grows even further.

2.2.3 Riming

In the riming process, the super-cooled cloud droplets collide with the falling snow particle and rapidly freeze on its surface. At an early stage of

riming the original crystal is still visible as can be seen in Figure 2.2a. As the riming process continues, more frozen droplets are covering the particle, and the underlying structure is only vaguely recognizable (Figure 2.2b). When the snow crystal is obscured, and the particle is more roundish and white, it is called a graupel (Figure 2.2c).

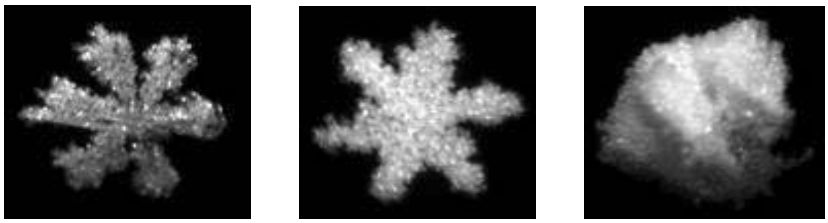

(a) **(b)** **(c)**

Figure 2.2. Snow crystals with different stages of riming, c) shows an example of graupel. Images are taken with the University of Utah MASC (Multi Angle Snowflake Camera) photo credits: Prof. Timothy Garrett with permission.

The stages of riming were previously determined by manual observations of individual particles (Harimaya and Sato, 1989; Mitchell et al., 1990; Mosimann et al., 1994). Mosimann et al. (1994) presented a scale between 0 to 5 (unrimed to graupel) based on the estimated percentage of rime coverage on the surface of the crystal. Lately, also automatic classification is reported based on e.g. roundness of the particle and interpixel brightness variability in (Garrett and Yuter, 2014) and both dimensions and shape descriptors of contour images and fall velocity differences in Grazioli et al. (2014).

The accretion of cloud droplets onto a snow particle adds its mass. The mass growth rate is dependent on snow particle and droplet properties and PSD of the droplets (Pruppacher and Klett, 1997; Jensen and Harrington, 2015; Erfani and Mitchell, 2017)

$$\left(\frac{dm}{dt}\right)_{\text{riming}} = \int_0^{d_{max}} E(D,d)A_g(D,d)|v(D)-v(d)|m(d)N(d)\mathrm{d}d, \qquad (2.8)$$

where d is the diameter of a cloud droplet, $A_g(D,d)$ is the geometric cross-sectional area occupied by both the snow particle and droplet, $E(D,d)$ is collection efficiency between the cloud droplet and snow particle, $v(D)$ and $v(d)$ are the fall velocities of the snow particle and droplet, respectively, $m(d)$ is the cloud droplet mass, $N(d)$ is the cloud droplet number distribution, and d_{max} is the diameter of the largest cloud droplet. Commonly it is assumed that the super-cooled droplets freeze on the snow particle upon impact, and therefore the collection efficiency $E(D,d)$ is equal to the

collision efficiency, hence the sticking efficiency is considered 1.0 (Lamb and Verlinde, 2011; Erfani and Mitchell, 2017). The collision efficiency in riming is affected by the shape and size of the collecting snow particle, and the particle must have grown by vapor to some critical size to collect cloud droplets, e.g. approximately size of 35μm for hexagonal columns and greater than 110 μm for hexagonal plates (Harimaya, 1975; Pitter and Pruppacher, 1974; Bruintjes et al., 1987; Wang and Ji, 2000; Lamb and Verlinde, 2011). If hexagonal columns and plates are compared, riming rate is higher for columns because of their faster fall velocity and higher collision efficiency (Erfani and Mitchell, 2017). The fall velocity of the cloud droplet is typically assumed to be zero (Heymsfield, 1982; Zhang et al., 2014). The collision efficiency is dependent on the size of the droplet; it is small for the droplet diameter smaller than 10 μm, e.g., (Kajikawa, 1974; Harimaya, 1975) and increases for larger droplet sizes (Pruppacher and Klett, 1997; Erfani and Mitchell, 2017).

The fall velocity of the snow particle increases with riming, not only because of the addition of the mass by accreted cloud droplets but also due to the different fall behavior of the rimed particles (Zikmunda and Vali, 1972). In (Locatelli and Hobbs, 1974) it is concluded that the densely rimed particle falls with speed up to twice as great as of a similar unrimed particle with the same maximum dimension. The fall velocity of rimed snowflakes depends on both the riming degree and their crystal type composition; the fall velocity of snowflakes consisting of irregular crystals is rather high for all riming regimes, whereas for needle or plate aggregates fall velocity increases with riming, and for aggregates of dendrites, the fall velocity is low throughout all degrees of riming stages (Barthazy and Schefold, 2006).

Based on the conceptual study of Heymsfield (1982) at the early stages of riming the water droplets accrete to the spaces between crystal branches and the diameter of the particle is not increasing. This leads to a result in a power-low $m(D)$ relation in Eq.(2.1) that the exponent, b_m, remains constant, while the prefactor, a_m, increases. Although earlier studies e.g. Locatelli and Hobbs (1974) stated that the exponent to be higher for rimed particles, Erfani and Mitchell (2017) showed that based on their data set, the exponent values are similar for unrimed and rimed particles. A similar observation was seen in Publication IV, where the exponents of $m(D)$ of different snow events were classified according to liquid water path (LWP), which can be considered as a proxy indicating riming process.

Riming is an important precipitation process, as observational studies

have shown it to contribute substantially to the snowfall rates and a large percentage of cloud systems contain supercooled liquid water (Hogan et al., 2003; Moss and Johnson, 1994). Mitchell et al. (1990) have estimated that riming constituted 30 to 40 % of the mass of fresh snow and Moisseev et al. (2017) found that with 22 snow events during winters 2014-2015 in Southern Finland the riming is responsible for 5% to 40% of snowfall mass. Riming is more common in the beginning or at the end of the season with milder temperatures, and also near large water bodies (Jiusto and Weickmann, 1973). In a lake-effect snow storm, riming of snow aggregates significantly influences the microphysical structure of the storm (Iguchi et al., 2012).

2.2.4 Aggregation

The snow crystals also tend to grow as they fall by colliding and sticking with other crystals forming an aggregate, these are usually called snowflakes (Lamb and Verlinde, 2011). The efficiency of the aggregation process seems to depend mainly on the crystal habit and the temperature region (Young, 1993). The aggregation rate, i.e. changes in the snow particle concentration can be stated (Pruppacher and Klett, 1997; Mitchell et al., 2006)

$$\begin{aligned}\left(\frac{dN(m)}{dt}\right)_{\text{aggr}} &= \frac{1}{2}\int_0^m A_g(m-m',m')E_{agg}(m-m',m') \\ &\quad \times|v(m-m')-v(m')|N(m-m')N(m')\mathrm{d}m' \\ &\quad -N(m)\int_0^\infty A_g(m,m')E_{agg}(m,m') \\ &\quad \times|v(m)-v(m')|N(m')\mathrm{d}m', \end{aligned} \tag{2.9}$$

where the first term describes the production of the ice aggregates of mass m due to aggregation of crystals having mass $m-m'$ and m' and the second term the depletion of aggregates of mass m due to the aggregation with particles of mass m'. The geometric cross-sectional area occupied by both the original snow particles is $A_g(m-m',m')$, $E_{agg}(m-m',m')$ is aggregation efficiency, $v(m-m')$, $v(m')$ and $N(m-m')$, $N(m')$ are the fall velocities and PSDs of the snow particles, respectively. The aggregation efficiency $E_{agg}(m-m',m')$ is a product of the collision and sticking efficiency. The sticking efficiency is temperature-dependent and typically smaller than one.

Snow crystals adhere to each other with different mechanisms e.g. the dendrites can mechanically interlock together as their arms are acting

as hooks or more simple structures can stick together due to electrostatic forces or sintering (Lamb and Verlinde, 2011). The mechanical interlocking is the prominent mechanism for aggregation in a temperature regime between -10 and -15°C. Although a snow particle is frozen, the water molecules near the crystal surface are less bound to the structure and are acting more as liquid-like. In sintering, the quasi-liquid molecules diffuse across the ice surface from a place of lower curvature or the environment towards a place of higher curvature, such as the contact point between two particles and form a solid bond. Sintering does take place at colder temperatures, but more efficiently near 0°C. The largest aggregates are usually found within a few degrees of 0°C (Young, 1993).

Aggregates have a highly irregular structure; they can be composed of any number of crystals, from a few to hundreds, in any arrangement. Depending on the primary particle habit, their structure can be loose, as usually with needle aggregates, or denser, if also riming is increasing the density and freezing cloud droplets are attached to open structure. Aggregation is an effective growth mechanism, and usually, the particle diameter is growing from millimeter to centimeter scale, such as for snowflakes the density always decreases as a function of the diameter. Hence the aggregation process can be recognized from the lower values of the exponent b_m of $m(D)$-relation. Typically b_m is approximately 2. In his thesis, Westbrook (2004) showed by simulating aggregates that $b_m > 2.0$ and the simulated aggregates had a fractal dimension $d_f = 2.05 \pm 0.1$. Similar results were obtained in (Ishimoto, 2008; Schmitt and Heymsfield, 2010) for d_f to have values 2.1 and 2.0-2.3, respectively. This is also confirmed by fitted values to measured aggregates e.g. in (Locatelli and Hobbs, 1974; Mitchell, 1996; Heymsfield et al., 2002; Szyrmer and Zawadzki, 2010) with gained values of 1.9, 2.1, 2.04 - 2.08 and 1.85-2.07, respectively.

The balance between gravity and drag forces define the terminal fall velocity of falling snow particles, and for the unrimed snowflakes, the dependence of velocity on size is smaller than in cases with single crystals. The gravitational and the frictional force seem to grow to the same extent with increasing size (Hanesch, 1999). The primary crystal type seem to have smaller influence on the fall velocity than in riming process (Hanesch, 1999; Barthazy and Schefold, 2006). Zawadzki et al. (2010) studied the fall velocity of unrimed snow particles and ended up using a constant exponent of 0.18 in the $v(D)$ relation.

According to Jiusto and Weickmann (1973), the most common snow

particle type in mid-latitude snowfall storms, are aggregates. This is, because many continental snow storms contain little super-cooled water, and the increasing of mass on snow particles results firstly through vapor deposition on snow crystals and lower in the clouds through aggregation process (Pruppacher and Klett, 1997). In an altostratus cloud in the temperature regime $-40°$-$(-20)°$C the diffusional growth dominated the ice crystal evolution, whereas between in temperatures between $-20°$-$(-10)°$C aggregation was the main growth mechanism (Field, 1999).

2.2.5 Melting

Melting process of the snow crystals and snowflakes is a significant part in the development of stratiform precipitation at mid- and high latitudes, and melting is also present in convective summer storms where hail and graupel are falling into warmer atmospheric layers. Melting of snow particles starts below the 0°C isotherm, and it usually takes several hundreds of meters for particles to melt completely. In stratiform precipitation, a clear melting layer can be observed and typically it is around 200 - 500 m thick (Fabry and Zawadzki, 1995). The thickness is influenced by several factors e.g. the size and type of the snow particles, precipitation intensity, temperature and humidity gradients and vertical air velocity. Melting process cools the air, and this can result in an isothermal layer, affecting the thermodynamic stability of the lower atmosphere separating it from the layer above the melting layer, and thus influencing the dynamics of the convective systems (Lamb and Verlinde, 2011). In sub-saturated conditions due to evaporation, the melting rate is decreased and postponed, the width of the so called non-melting layer increases nearly linearly with decreasing relative humidity (Matsuo and Sasyo, 1981a).

For all the snow particle types melting will lead to decrease in particle size and increasing of fall velocity, and consequently decrease in particle concentration. The distribution of the forming liquid water on the melting particle is, however, dependent on the original habit (Figure 2.3). The flow of the liquid water is mainly driven by the surface tension, and the impact of the aerodynamic force is relatively small for snow crystals and snowflakes (Knight, 1979). In columnar crystals and needles the melting starts uniformly, but as the melting proceeds, the melted water forms bulges on the thin crystal. The melting, and in sub-saturated conditions the evaporation, is more rapid at the thin parts exposed to the surrounding air. Oraltay and Hallett (2005) found that these thin parts can break

and shed mixed ice and water fragments. In planar crystals, the water is forming a double convex lens with the edges defined by the original hexagonal shape, and the relative melting rate seems to be influenced by the thickness of the formed liquid layer (Knight, 1979). No shedding or breaking up was observed with planar crystals (Oraltay and Hallett, 2005). Fujiyoshi (1986) described the melting pattern of aggregates in five stages. At the first stage, small droplets are produced at the tip of the crystals. The degree of melting is uneven in the different parts of the snowflake, and it seems to be most intense at the bottom part of the particle. At the second stage, the particle is already largely melted, and the original structure of the snow crystals forming the aggregate is hardly discernible. The surface is jagged as the melting water is accumulating to the interior parts and leaving the surface of the particle uncovered of water. At the third stage, the surface is more smooth, and no discernible crystal formats can be observed, and holes are forming in those parts of the melting snowflake, where the ice is thin, because of the more rapid melting rate. Fujiyoshi (1986) speculated that the melted particles can break into parts. At the fourth stage, snowflakes are smooth and have no holes, but have an irregular shape. At the last stage, the snowflake displays round, plate- or lens-like shapes rather than spherical. A similar description was in the study of Mitra et al. (1990), who divided melting of snowflakes into four stages. The melting pattern of hail and graupel differ from the melting patterns of snowflakes and snow crystals. The liquid layer wrapping a hail particle forms a torus around the ice core due to the aerodynamics and, when a critical mass of liquid water is reached, shedding occurs. Because a graupel has a lower density than hail, the liquid will flow into the cavities, and the spongy ice core will soak in melted water and no torus is formed (Rasmussen and Heymsfield, 1987).

The impact of aggregation and breakup of melting snow particles within the melting layer is still partly unresolved (Heymsfield et al., 2015), although studies showing the significance in (Yokoyama and Tanaka, 1984; Yokoyama et al., 1984; Göke, 1999; Zrnić et al., 1993; Drummond et al., 1996) or vice versa in (Ohtake, 1969; DuToit, 1967) has been carried out already several decades. The aggregation efficiency is high in the temperature region close to 0°C, due to the enhanced adhesion of the particle surfaces. Aircraft observations show the presence of the larger snowflakes after the onset of melting (Stewart et al., 1984; Willis and Heymsfield, 1989; Heymsfield et al., 2015). However, Ohtake (1969) measured the PSDs

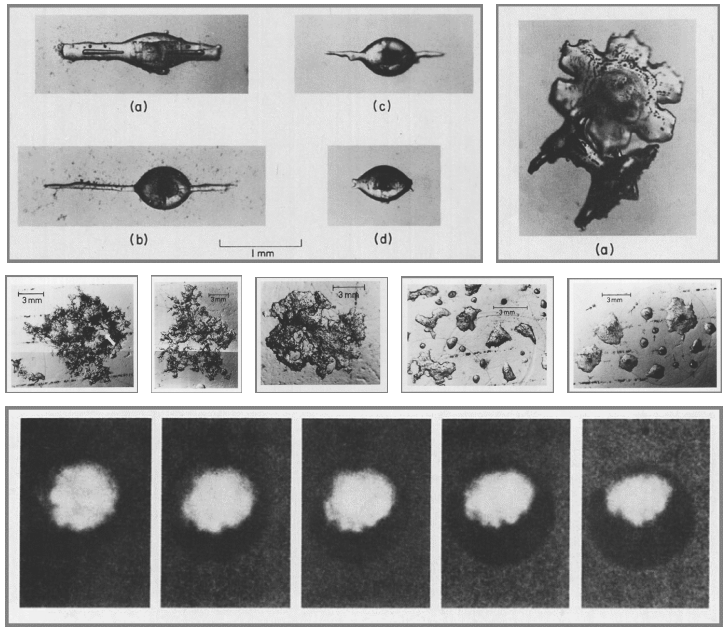

Figure 2.3. Examples of melting patterns of different snow particles. Upper pane: columnar crystal and plate from (Knight, 1979). Middle pane: Five stages of melting snowflakes (Fujiyoshi, 1986). Lower pane: Melting hail stone (Rasmussen and Pruppacher, 1982). Published with permission ©American Meteorological Society

above and under the melting layer, and found no significant aggregation or break-up effect present inside the melting layer. Fabry and Zawadzki (1995) gathered long-term melting layer observations by vertically pointing X-band radar and UHF wind profiler and stated that aggregation at the early stages of the melting and breakup in the final stages contribute little to the radar observed melting layer signatures.

2.3 Melting layer models

The melting layer is prominent in a widespread stratiform rain, and it is a dominating feature in radar observations with enhanced values of reflectivity factor; hence it is called "bright band" (Fabry and Zawadzki, 1995). In the early days of radar meteorology, at the times of World War II, the bright band was identified and firstly reported in 1946 by Ryde (Austin and Bemis, 1950; Atlas and Ulbrich, 1990). Because of the strong signature in microwave frequencies, the melting layer has been widely studied with remote sensing instruments. Therefore existing melting layer models usually include two parts, the microphysical and electromagnetic part. In

this section, the microphysical models are presented, and in Section 5.2 the electromagnetic part is discussed.

Several melting layer models exist in the literature describing the melting of snowflakes. These utilize different microphysical parametrizations and address the changes of the parameters differently in the course of melting. Many of them are shown in Figure 2.4 and listed in Table 2.1 with the corresponding assumptions of microphysical parametrization. Most models are 1D-steady state models, and do not account for the horizontal variability of the atmospheric conditions, but Szyrmer and Zawadzki (1999) coupled the melting layer parametrization to a 2D-dynamical model, and Olson et al. (2001) drove the model by 3D-cloud-resolving model (CRM) simulations. The underlying assumption in many of the models is that the mass of individual particles and the mass flux are conserved, thus one snowflake melts into one raindrop.

2.3.1 Melting rate

The melting rate of a snow particle can be defined from the heat balance at the particle surface. The melting results from the two main mechanisms transferring external heat to the particle; the conduction of heat because of the temperature difference at the particle surface and the surrounding atmosphere, and the latent heat released/removed by condensation/evaporation (Szyrmer and Zawadzki, 1999). The melting rate dm/dt is the melted mass of the particle at a given time (Szyrmer and Zawadzki, 1999)

$$-L_f \left.\frac{dm}{dt}\right|_{melt} = \frac{dq_{diff}}{dt} + L_v \left.\frac{dm}{dt}\right|_{cond}, \tag{2.10}$$

moreover, if the terms are following the form presented in (Mitra et al., 1990)

$$\begin{aligned} -L_f \frac{dm}{dt} = 2\pi D F C_c \Bigg(& k_a \left[T_\infty(t) - T_0\right] \\ & + \frac{D_v M_w L_v}{R_v} \left[\frac{(RH/100) e_{sat,w}(T_\infty(t))}{T_\infty(t)} - \frac{e_{sat,w}(T_0)}{T_0} \right] \Bigg). \end{aligned} \tag{2.11}$$

Different to Mitra et al. (1990), here in Eq.(2.11) the diameter D is taken out of the capacitance factor C_c term. The capacitance factor is dependent on the particle shape. In (Mitra et al., 1990) for spherical particle it is the same as the particle radius (here the factor C_c equals to 1), but for a non-spherical particle it is different and changes during melting. The effect of particle shape and structure on melting rate is considered e.g. in (Matsuo and Sasyo, 1981a; Klaassen, 1988; Mitra et al., 1990). The

ventilation factor F is generally considered to be the same for heat and vapor transfer. The constants in Eq.(2.11) are the latent heat of fusion L_f and evaporation L_v, the heat conductivity of air k_a, the diffusivity of water vapor in air D_v, the molecular weight of water M_w and the ideal gas constant R_v. The saturation vapor pressure over water surface is $e_{sat,w}$ in the ambient temperature T_∞ and the particle surface temperature T_0, and RH is the relative humidity of the air around the melting snowflake. The change in melted mass fraction f_m for each particle size in a given time is defined

$$\frac{df_m}{dt} = \frac{1}{m_t}\frac{dm}{dt}, \tag{2.12}$$

when m_t is the total mass of the particle. To connect the melting rate to melting layer, Eq.(2.11) is integrated from the 0°C isotherm height downwards and the time dependence is converted to height dependence as in (Klaassen, 1988)

$$\frac{df_m}{dt} = \frac{df_m}{dh}\frac{dh}{dt} = \frac{df_m}{dh}v, \tag{2.13}$$

where h is the height and v is the terminal fall velocity of the particle $v = v_\infty - v_a$ as fall velocity of air is extracted. It is assumed that the vertical velocity of air is in the opposite direction than the particle velocity and v_a is less or equal to observed fall velocity of the particle v_∞. Usually, the v_a is assumed to be constant (Klaassen, 1988).

From Eq.(2.11) it can be seen that the melting process is governed by the environmental temperature and relative humidity conditions. In saturated conditions, the component of condensation/evaporation heat determines approximately half of the used heat for melting (Szyrmer and Zawadzki, 1999). If the surrounding air is sub-saturated, part of the heat is removed from the melting due to the evaporation. Matsuo and Sasyo (1981b) modeled the postponing and slowing effect on melting in sub-saturated conditions, and the non-melting layer increased by a factor of more than 4, when the relative humidity was dropped from 90% to 50%. Nevertheless, in many melting layer models, a relative humidity of 100% is assumed, and the delay in the onset of melting is considered by starting the melting process at wet-bulb temperature of 0°C (Klaassen, 1988). Although the condensation/evaporation is considered in the heat budget, the excess/loss of mass is not usually accounted for in the models. Szyrmer and Zawadzki (1999) estimated that the mass error in saturated conditions is less than 7% and for the sub-saturated conditions, it is even less. Klaassen (1988) speculated that the error is in the order of 10%. Melting cools the surrounding air, and this is taken into account in (Klaassen, 1988) by a negative

feedback system connected to the melting rate, but generally, this is not considered in the other models. The heat transfer by radiation is usually considered to be negligible (Lamb and Verlinde, 2011), and it is also assumed that the temperature on snow particle surface is 0°C during the melting. Other components in Eq.(2.11) that affect the melting process are the shape of the particle through ventilation factor and capacitance factor, fall velocity and density of the particle.

The model presented in (Russchenberg and Ligthart, 1996) differs from the other presented models in Table 2.1. There the melting rate is parametrized as a function of expected melting layer thickness defined from an experimental function of rain rate R as $h_{max} = 492R(\mathrm{mmh}^{-1})^{0.272}$ in meters. The melted mass fraction is then empirically defined

$$f_m = \frac{1}{2}\left[\sin\left(\frac{h\pi}{h_{max}} - \frac{1}{2}\right) + 1\right]. \tag{2.14}$$

2.3.2 Density

The density of snowflake depends on snow habit, with degrees of aggregation and/or riming, and this affects the melting patterns and melting rate. The density of snow has a strong effect on the radar-observed bright band, and the melting of denser particles increases the thickness of the melting layer as the excess of mass takes a longer time to melt, and the higher density corresponds to faster falling particles also stretching the distance of the particles path while melting.

The utilized density or mass estimates for the dry snowflakes for different melting layer models are stated in Table 2.1. Mostly these are taken from the know relations in literature. Some studies e.g. Yokoyama and Tanaka (1984); Fabry and Szyrmer (1999) tested different relations and their impact on the melting layer characteristics, and Zawadzki et al. (2005) introduced a riming factor to correspond to the increased particle density at the top of the melting layer.

Due to the assumption that one snowflake results in one raindrop, the mass conservation can be written as

$$\rho_i(0.1D_i)^3 = \rho_s(0.1D_s)^3 = \rho_{ms}(0.1D_{ms})^3 = \rho_r(0.1D_r)^3, \tag{2.15}$$

and although, some of the models assume aggregation process (e.g. Göke (1999),Yokoyama and Tanaka (1984)) or non-spherical particles (e.g. Mitra et al. (1990)), the Eq.(2.15) is still applied.

Figure 2.4. Microphysical melting layer models of melting snowflakes and the research applying these models.

Model	Snow	Rain	Melting Snow	T	RH	PSD	Aggr.
Dissanayake and McEwan (1978a)	$\rho_s = 0.02 D_s^{-2}$, $0.008 \leq \rho_s \leq 0.3$ $v_s = v_r \left(\frac{\rho_s}{\rho_w}\right)^{1/3}$ $F_s = 1 + 0.21 R_e^{0.5}$, Pruppacher, Klett (1997)	$m_r = \pi/6 \rho_w D_r^3$ Atlas et al. (1973) F_r with same relation as F_s	$D_{ms}^3 = f_m D_r^3 + D_i^3$, with inner diam. D_i $v_{ms} D_{ms} = v_r D_r$ F_{ms} with same relation as F_s	variable $\Delta T \mathrm{km}^{-1}$	sub.	Marshall and Palmer (1948)	No
Matsuo and Sasyo (1981a)	ice-skeleton structure $\rho_i = 0.036 \mathrm{gcm}^{-3}$ $v_s = \sqrt[2]{\frac{4 D_s \rho_i g}{3 \rho_a C_{ds}}}$ $F_s = 1 + 0.24 R_e^{0.5}$ C_{cs} measured averaged value of 1.75 $C_{ds} = 1.2$	$m_r = \pi/6 \rho_w D_r^3$ $v_r = 9.31[1 - exp(-D_r/1.77)^{1.147}]$ F_r with same relation as F_s C_{cr} = 1 $C_{dr} = \frac{4 g \rho_w D_r}{3 \rho_a} v_r^{-2}$	decreased D_i, ρ_i constant $v_{ms} = \sqrt[2]{\frac{4 D_{ms} \rho_i g}{3 \rho_a C_{dms}}}$ F_{ms} with same relation as F_s - $C_{dms} = \frac{C_{ds} - C_{dr}}{D_i - D_r}(D_{ms} - D_i) + 1.2$	$6°\mathrm{Ckm}^{-1}$	sub.	-	No
Yokoyama and Tanaka (1984)	$\rho_s = 0.05$ gcm^{-3}, $\rho_s = 0.2$ gcm^{-3} $v_s = a_{vs}^r D_r^{0.31}$, with a_{vs}^r = 160-234 $F_s = 1 + 0.22 R_e^{0.5}$ C_{ds}	$m_r = \pi/6 \rho_w D_r^3$ $v_r = 1791.5 D_r^{0.762}$ F_r with same relation as F_s C_{dr}	$D_{ms} = D_r f_m + (1 - f_m) \frac{\rho_w}{\rho_s}^{1/3}$ $v_{ms} = \frac{v_r}{\left(f_m (1 - \frac{\rho_w}{\rho_s}) + \frac{\rho_w}{\rho_s}\right)^{1/3}} \left[\frac{C_{dr}}{C_{dms}}\right]^{1/2}$ F_{ms} with same relation as F_s $C_{dms} = f_m^{c_d}(C_{dr} - C_{ds})$, c_d = 3 or 1/3	constant lapse rate	sat.	Marshall and Palmer (1948)	Yes
Klaassen (1988)	$\rho_s = 0.74 D_r^{-0.8}$ $v_s = \sqrt[2]{\frac{4 D_s \rho_s g}{3 \rho_a}}$ $C_{cs} = 2 - e$, initial value $e = 0.3$ $C_{ds} = 1.0 - 0.5e$, initial value $e = 0.3$	$m_r = \pi/6 \rho_w D_r^3$ v_r, Atlas et al. (1973) $C_{cr} = 1$ $C_{dr} = 0.5$	$\rho_{ms} = \frac{\rho_s}{1 - f_m}$ $v_{ms} = \sqrt[2]{\frac{4 D_{ms} \rho_s g}{3 \rho_a}}$ - C_{ds} until particle saturated with water	isothermal layer is corrected	sat.	$N(D_r) = N_0 D_r^2 exp(-5.67 D_r / D_0)$	tested
Mitra et al. (1990)	spheroid with $\rho_s = 0.02$ gcm^{-3}, $a_x = 0.3$ v_s, Locatelli and Hobbs (1974) F_s, Eq.(2.29) $C_{cs} = 0.8 C_{ci}$ with $C_{ci} = \alpha/(sin^{-1}\alpha)$	$m_r = \pi/6 D_r^3$ v_r, Beard (1976) F_r, Eq.(2.29) 1	ρ_{ms} and a_x linearly changing with f_m v_{ms}, experimental F_{ms}, Eq.(2.29) C_{cms} linearly between $0.8 \cdot C_i$ and $1.0 \cdot C_i$	variable	90%	-	No
Russchenberg and Ligthart (1996)	$\rho_s = 0.01 - 0.5 \mathrm{gcm}^{-3}$ v_s, Matsuo and Sasyo (1981b)	spheroid, $D_r = 0.495(\frac{3.67}{4.1} R^{0.21})$ v_r, Atlas et al. (1973)	$\rho_{ms} = \frac{\rho_s}{1 - (1 - \rho_s) f_m}$ v_{ms}, Matsuo and Sasyo (1981b)	paramet. melting	sat.	mono-disperse	No
Szyrmer and Zawadzki (1999)	different relations $v_s = 366 D_r^{0.61}$ $F_s = 0.86 + 0.24 R_e^{1/2}$	$m_r = \pi/6 D_r^3$ $v_r = 1690 D_r^{0.6}$ $F_r = 0.78 + 0.28 R_e^{1/2}$	$\rho_{ms} = \frac{\rho_s \rho_w}{[f_m \rho_s + (1 - f_m)\rho_w]}$ v_{ms}, Eq.(2.22) $F_{ms} = 33.0 \frac{D_r^{1.7}}{D_m}$	variable $\Delta T \mathrm{km}^{-1}$	90%	Marshall and Palmer (1948)	No
Giangrande (2007)	$\rho_s = 0.178 f_{rim} D_r^{-0.922}$ v_s, Zawadzki et al. (2005) same as F_{ms}	spheroid with axis ratio from Brandes et al. (2002) v_r, Brandes et al. (2002) same as F_{ms}	$\rho_{ms} = \frac{\rho_s \rho_w}{f_m \rho_s (1 - f_{ms}) \rho_w}$ v_{ms}, Szyrmer and Zawadzki (1999) $F_{ms} = 33.0 \frac{D_r^{1.7}}{D_{ms}}$	measured profile	sat.	Marshall and Palmer (1948)	bi-exp.

Table 2.1. Microphysical melting layer models with assumptions of microphysical parametrization of density ρ or mass m, velocity v, ventilation factor F, capacitance factor C_c, and drag coefficient C_d. The subscripts i, s, ms and r describe ice, snow, melting snow and rain, respectively. In case parametrization of the parameter is not described in corresponding journal, it is left out from the table.

The density increases in the course of melting, in e.g. (Klaassen, 1988; Mitra et al., 1990; Szyrmer and Zawadzki, 1999) it is assumed to vary linearly with the melted mass fraction between the initial snowflake density and that of water (Fabry and Szyrmer, 1999)

$$\rho_{ms} = \frac{\rho_s \rho_w}{[f_m \rho_s + (1 - f_m)\, \rho_w]}. \tag{2.16}$$

Whereas Matsuo and Sasyo (1981a) modeled the melting as a decrease in the ice frame dimensions. Fabry and Szyrmer (1999) proposed a two-layered sphere approximation, where the density of the interior part is greater than the density of the exterior part, and changes in density because of the melting were more intense in the shell. Recent studies by Botta et al. (2010); Johnson et al. (2016); Leinonen and von Lerber (2017) have simulated the melting pattern of snowflakes more rigorously following the description of Mitra et al. (1990) and Fujiyoshi (1986). The goal is to improve the bright band modeling as the scattering calculations are sensitive to melted fraction of the particle and the location of the water inside the particle. These more precise simulations of melting are not yet connected to a microphysical melting layer model.

2.3.3 Terminal fall velocity

The fall velocities of various types of snow particles in the melting layer models are often presented in the power-law form (Eq.(2.2)), where the parameters are taken from the literature e.g. (Magono and Nakamura, 1965; Locatelli and Hobbs, 1974; Jiusto and Bosworth, 1971). Another approach is to calculate the fall velocity by equalizing gravitational force with drag force

$$mg = \frac{1}{2} C_d A \rho_a v^2, \tag{2.17}$$

and the fall velocity is

$$v^2 = \frac{4 D \rho g}{3 \rho_a C_d}, \tag{2.18}$$

assuming spherical particle with mass $m = \pi/6 \rho D^3$ and cross-section $A = \pi/(4D^2)$ (Klaassen, 1988). Different values of drag coefficient C_d are used in models, these are stated in Table 2.1. To consider the decreased density of air as a function of altitude the values of velocities are multiplied with factor $(\rho_{a,0}/\rho_a)^{0.5}$, where $\rho_{a,0}$ is the air density at mean sea level, and ρ_a at the height of interest.

The fall velocity of raindrops in melting layer models is often obtained from derived relations in literature e.g. (Gunn and Kinzer, 1949; Best, 1950;

Sekhon and Srivastava, 1971; Atlas et al., 1973; Brandes et al., 2002). In comparison to snow particles, the fall behavior of rain drops is easier to define, although drops may oscillate around their equilibrium shape and large rain drops are shown to break-up; about 6–8 mm are believed to be the largest encountered in natural conditions (Testik and Barros, 2007). Raindrops greater than 0.25 mm are flattened on the lower surface because of the drag and the deformation increases with size (Testik and Barros, 2007). The fall velocity as a function of rain drop size is fairly established and the discrepancies between the different relations, especially for small-sized drops with diameter below 2 mm, are small. In the high latitude climate the drop size is usually small, the mass-weighted mean diameter values are concentrated at around 1.5 mm (Leinonen et al., 2012b). The fall velocity of rain drops can be discriminated from the low-density snow particles, for 2 mm snowflakes the fall velocity values are in the range of 1-1.5 ms^{-1}, whereas for raindrop the fall velocity is 5-6 ms^{-1}.

As a particle melts, its fall velocity increases. Yokoyama and Tanaka (1984) modeled the change by calculating the decreasing value of drag coefficient and diameter in Eq.(2.18). Hardaker et al. (1995) assumed, because of the mass conservation and following the study of Foote and Toit (1969), the fall velocity of melting particle can be retrieved from

$$v_s D_s = v_{ms} D_{ms} = v_r D_r. \tag{2.19}$$

This is based on the definition of the Reynolds number R_e, which is a dimensionless parameter describing the particle flow in fluid, according to Pruppacher and Klett (1997)

$$R_e = \frac{vD\rho_a}{\eta_a}, \tag{2.20}$$

where ρ_a is the density of air, D is the characteristic length of the particle relative to flow and η_a is the dynamic viscosity. Szyrmer and Zawadzki (1999) approximated, because of the similar values of the exponents of power-law form of the $v(D_r)$ relation of rain a^r_{vr} and snow a^r_{vs}, when defined as a function of melted diameter D_r, the velocity for melting particles can be stated

$$v_{ms} \approx \frac{1}{g_v\left(f_m\right)} v_r\left(D_r\right) \tag{2.21}$$

where

$$g_v\left(f_m\right) \approx \frac{a^r_{vr}}{a^r_{vs}} - c_g f_m - c_g {f_m}^2 \tag{2.22}$$

with $c_g = 0.5\left[\left(a^r_{vr}/a^r_{vs}\right) - 1\right]$.

Mitra et al. (1990) studied the change of fall velocity in melting as a function of the melted mass fraction based on measurements in a vertical wind tunnel. They investigated both the fall speed as well as the fall patterns of aggregated dendrites with sizes of 5 mm to 10 mm. They have observed that at the initial stage of melting, the fall velocity changed only a little, but as the melting progressed to around 70% of the mass, velocity increased very rapidly (Mitra et al., 1990). Göke (1999) parametrized a relation based on the experimental curve of Mitra et al. (1990)

$$v_{ms} = \begin{cases} v_s, & \text{for } f_m = 0 \\ v_s + 0.01(v_r - v_s)\exp(4.6 f_m), & \text{for } f_m > 0 \end{cases} \tag{2.23}$$

and a parametrization of Battaglia et al. (2003)

$$v_{ms} = g_v(f_m)(v_r - v_s) + v_s, \tag{2.24}$$

with

$$g_v(f_m) = \frac{f_m + f_m^2}{9.2 - 3.6(f_m + f_m^2)}. \tag{2.25}$$

2.3.4 Ventilation factor

When a snow particle is melting or sublimating during falling, the rate of change of mass and heat transfer is described by a ventilation factor (Field et al., 2008). The ventilation factor is the ratio of the mass or heat fluxes to or from the particle, when the particle is moving with respect to a motionless state (Pruppacher and Klett, 1997). In melting layer models, it is usually assumed that the factors are the same for both the transfer of heat and water vapor. The ventilation factor F is dependent on hydrometeor size and its physical characteristics; hence it is changing throughout the melting, and the melting process is sensitive to its parametrization. Szyrmer and Zawadzki (1999) approximate that a F_{ms} expression is dependent on the melted diameter and the degree of melting, assuming a constant density of snow (0.1 gcm^{-3}),

$$F_{ms} = B_m \frac{D_r^{A_m}}{D_{ms}} \tag{2.26}$$

with constants $A_m = 1.7$ and $B_m = 33.0 cm^{-0.7}$. This approach is adopted in (Battaglia et al., 2003; Giangrande, 2007) and in Publication I. Mitra et al. (1990) describe the ventilation factor following the approach presented in (Pruppacher and Klett, 1997) with length parameter L is defined by

perimeter p, total surface area Ω and spheroid eccentricity α

$$\begin{aligned} L &= \frac{\Omega}{p} \\ p &= 2\pi r_a \\ \Omega &= \pi r_a^2 \left[2 + \pi(a_x) \frac{1}{\alpha} ln \left(\frac{1+\alpha}{1-\alpha} \right) \right] \\ \alpha &= \sqrt{1 - a_x^2} \\ a_x &= \frac{r_b}{r_a}, \end{aligned} \tag{2.27}$$

with $r_{a,b}$ describing the radius of the particle along the axis a and b. The ventilation factor for both heat and vapor transfer can be written

$$F = \begin{cases} 1 + 0.14\chi^2 & \chi \leq 1.0 \\ 0.86 + 0.28\chi^2 & \chi > 1.0 \end{cases} \tag{2.28}$$

$$\begin{aligned} \chi &= S_h^{1/3} R_e^{1/2} \\ S_h &= \frac{\nu_a}{D_v} \\ R_e &= \frac{L v_s}{\nu_a}, \end{aligned} \tag{2.29}$$

where ν_a is the kinematic viscosity of air, S_h is the Sherwood number and χ is the heat transfer coefficient. Battaglia et al. (2003) showed the effect of parameterization of ventilation factor on the melting rate considering also changes in density, velocity, and shape, and concluded that the parameterization presented in (Szyrmer and Zawadzki, 1999) appears to fit on average best to reflectivity factor and fall velocity observations within melting layer.

2.3.5 Aggregation and break-up in melting layer

The one-to-one correspondence implies that no aggregation, break-up or drop-shedding is occurring in the melting layer. Due to the mass flux conservation, it can be stated

$$\begin{aligned} & N_s(D_s)\, v_s(D_s)\, dD_s \\ = \;& N_m(D_m)\, v_m(D_m)\, dD_m \\ = \;& N_r(D_r)\, v_r(D_r)\, dD_r, \end{aligned} \tag{2.30}$$

where the changes in distributions must be considered according to the diameter definition (Petty and Huang, 2011).

As stated in Section 2.2.5 there is a discussion on the importance of the aggregation and break-up processes inside the melting layer. Even though aggregation and break-up phenomena are present in the melting

layer, the combined effect can accounted for less than 1 dB of change in reflectivity (Fabry and Zawadzki, 1995). Moreover, regarding extinction properties, which are less sensitive to changes in size distribution, this effect is even less important (Battaglia et al., 2003). In laboratory studies, Mitra et al. (1990) reported that the spontaneous breakup of melting dendrite aggregates is rare unless the snowflake has a strong asymmetric mass distribution. Only a few models consider aggregation and break-up processes, and modeling numerically the stochastic collection or breakup equations such as presented in (Mitchell, 1988) for melting particles is challenging. Klaassen (1988) estimated a spontaneous break-up at the later stage of melting and improved simulations of the melting process with respect to observations, however the corresponding improvements were not seen to include aggregation. Yokoyama and Tanaka (1984) constructed two conceptual models of mono-disperse distribution; a non-coalescence and -break-up model and the other considering both the collision and the break-up effect. In the coalescence two particles with the same size attach to each other and form a larger particle, the fall velocity of the aggregated particle increases and the number concentration decreases. In the break-up the one particle breaks into two particles with the same size, the fall velocities of the new particles are less than of the previous particle and the number concentration increases. Yokoyama and Tanaka (1984) studied by modeling at which stage of the melting layer the coalescence and break-up would explain the two-wavelength radar observations measured in (Yokoyama et al., 1984). Göke (1999) modeled the stochastic aggregation process according to Tzivion et al. (1987) and compared with observations in a case study; a good agreement was found by assuming collision efficiency of 100% within first 100 m below the on-start of the melting. Towards to the lower parts of the layer utilizing around 50% collision and 50% breakup efficiencies in simulations produced the most accurate results compared with the measured PSDs. Giangrande (2007) explored the effect of aggregation by utilizing a bi-exponential distribution and assuming larger particles present in the melting layer to reproduce the observed polarimetric signatures.

2.3.6 Melting layer model utilized in the study

The focus in Publication I was to investigate the effect of microphysical parametrization of snow particles, namely the assumption of the density and fall velocity, to the estimated attenuation of radar signal in the melting

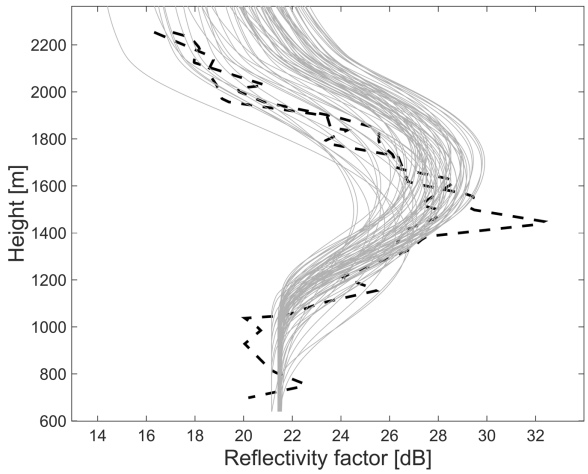

Figure 2.5. Dashed black line presents the averaged equivalent radar reflectivity factor profile on September 21, 2010 and the gray thin lines are modeled values by assuming different $m(D)$ and $v(D)$ relations from literature values.

layer. The data set used included PSD in rain as measured on the ground, temperature profile from sounding and equivalent radar reflectivity factor (Z_e) and reflectivity-weighted velocity (v_Z) data. The optimized relations of $m(D)$ and $v(D)$ were searched by comparing the measured Z_e and v_Z profiles to the observed ones. The data set in the study for examining the microphysical parametrization was limited, and thus the goal was not to develop a new melting layer model. The implemented model was based on earlier models, mostly following the principles presented by Szyrmer and Zawadzki (1999). The adapted solutions were commonly used and applicable to a wide range of conditions.

Following a standard approach, the mass of individual particles and the mass flux were considered to be conserved during melting (Eq.(2.15), (2.30)), and hence the aggregation and break-up are not included in the study. In rain, the gamma-distributed PSD was assumed (Bringi and Chandrasekar, 2001) and the fall velocity of rain drops was obtained from (Atlas et al., 1973). The hydrometeors were assumed to be spherical, and no capacitance correction term was considered. The average ventilation factor was defined as in (Szyrmer and Zawadzki, 1999).

Both relations of fall velocity and density of snow as a function of particle size were presented using the power-law form; for the fall velocity

$$v_s\left(D_s\right) = \left(\frac{\rho_{a,0}}{\rho_a}\right)^{0.5} a_{vs}\left(0.1 D_s\right)^{b_{vs}}, \tag{2.31}$$

and for the density

$$\rho_s = a_{ds} \left(0.1 D_s\right)^{b_{ds}} . \tag{2.32}$$

The optimized factors for a_{vs}, b_{vs}, a_{ds} and b_{ds} were estimated by fitting modeled profile with the radar measurements using a nonlinear least squares method. Initial guesses of the snow parameters were taken from the relations defined in (Fabry and Szyrmer, 1999; Battaglia et al., 2003; Locatelli and Hobbs, 1974; Barthazy and Schefold, 2006) and the search was constrained to physically meaningful values. Figure 2.5 shows an example of measured Z_e profile and the modeled profiles when different $m(D)$ and $v(D)$ relations for snow were assumed. The additional fitting parameters were N_w and D_0 of the PSD in rain to minimize possible discrepancies between the PSD measured on the ground and the actual PSD just below the melting layer.

The density of melting particles was assumed to be a linear a function of the melted mass fraction f_m. The size was calculated as Skaropoulos and Russchenberg (2003)

$$D_{ms}^3 = D_r^3 \left[f_m + (1 - f_m)\right] \rho_r / \rho_s, \tag{2.33}$$

and the melting snow fall velocity was calculated according to Yokoyama and Tanaka (1984)

$$v_{ms} = \frac{v_s}{\left[f_m \left(\rho_s/\rho_r - 1\right) + 1\right]^{1/3}} \left[\frac{1}{1 + \left(C_{dr}/C_{ds} - 1\right) f_m}\right]^{1/2}, \tag{2.34}$$

where C_{dr} and C_{ds} are the drag coefficients of raindrop (0.5) and snow $C_{ds} = C_{dr} \left(v_r/v_s - v_s\right)$, respectively. The melting process was simulated assuming the air is saturated with respect to water, and the vertical air motion is negligible compared to fall speed. The temperature on the particle surface was assumed to be constant at 0 °C throughout the melting process.

2.4 Mass retrieval based on hydrodynamic theory

Particle mass is a fundamental microphysical property. The mass in conjunction with PSD and fall velocity measurements determine the bulk properties such as an equivalent reflectivity factor (Z_e) and liquid equivalent snowfall precipitation rate (S) for quantitative precipitation estimation (QPE). Earlier, when snow particles were studied by collecting individual particles, photographing and melting them, the mass of a particle with the

shape information could be obtained (Nakaya and Tereda, 1935; Magono and Nakamura, 1965; Ohtake, 1969; Langleben, 1954; Zikmunda and Vali, 1972; Kajikawa, 1972). Nowadays data are gathered mostly by automatic optical imagers. Unfortunately, there is no single instrument, which would reliably and simultaneously measure mass, shape, and fall velocity of an falling snow particle. Therefore masses of snow particles are either retrieved from combined disdrometer and other instrument observations as performed in Publication III and e.g. in (Muramoto et al., 1995; Heymsfield et al., 2004; Brandes et al., 2007; Huang et al., 2010; Wood et al., 2014) or utilizing the general hydrodynamic theory (Böhm, 1989) connecting particle terminal velocity and shape observations as done both in Publication IV and Publication V and e.g. in (Hanesch, 1999; Szyrmer and Zawadzki, 2010; Huang et al., 2015). For a single ice crystal with regular geometrical structure, mass also can be estimated from the projected cross-sectional area (Heymsfield et al., 2004).

2.4.1 Hydrodynamic theory

A hydrometeor falling in still air can be regarded as a particle moving through a fluid. In a stationary flow, the relative importance of the inertia term and the frictional term define the flow type. Reynolds number R_e defined in Eq.(2.20) indicates the transition from laminar to turbulent flow. When the inertial forces dominate over the viscous forces (when the fluid is flowing faster and R_e is larger) then the flow is turbulent. When the viscous forces are dominant (slow flow, low R_e), the fluid is orderly with all particles moving in straight lines, then the flow is laminar. These flow types define the forces acting on the falling snow particles, and the equation of motion is determined from equilibrium of forces, in this case of drag, buoyancy, and gravity. Atmospheric buoyancy is usually assumed to be small compared to the drag and gravity, and the connection between the fall velocity and mass can be retrieved from Eq. (2.17). The drag coefficient C_d depends on the shape of the body and the roughness of its surface, but it is also depends on fall velocity itself through Reynolds number and the degree of turbulence in the flow. A common approach is to utilize the Best number $X_b = C_d R_e^2$ to calculate velocities (Beard, 1976) as it is related to C_d, but independent of fall speed. The mass can then be stated

$$m = \frac{X_b A \eta_a^2}{2 g \rho_a D^2}. \tag{2.35}$$

To retrieve the mass from the velocity measurements, a relation between R_e and X_b needs to established. Abraham (1970) derived a simplified functional dependence, where a rigid spherical particle together with its boundary layer forms one body passing through an inviscid fluid. Based on Abraham (1970) results, Böhm (1989) derived a general equation for the fall velocity of hydrometeors. Essential is the semi-empirical dependence between the Reynolds number R_e and the Best number X_b. The Reynolds number is

$$R_e = \frac{\delta_0^2}{4}\left[\left(1+\frac{4X_b^{1/2}}{\delta_0^2 C_0^{1/2}}\right)^{1/2}-1\right]^2 \tag{2.36}$$

or vice versa Best number can be stated as

$$X_b = \left[\frac{\delta_0^2 C_0^{1/2}}{4}\left[\left(\frac{\sqrt{4R_e}}{\delta_0}+1\right)^2-1\right]\right]^2, \tag{2.37}$$

with heuristic defined coefficients of characterizing boundary layer thickness $\delta_0 = 5.83$ and pressure drag coefficient $C_0 = 0.6$ (Böhm, 1989). Böhm considered hydrometeors as porous spheroids and the drag coefficient of a snow particle C_{ds} is related to the drag coefficient of an equivalent disk C_d

$$\frac{C_{ds}}{C_d} = \left(\frac{A_\perp}{A_e}\right)^{3/4}, \tag{2.38}$$

with A_e as the area normal to the flow and $A_\perp$ the area of the smallest circle or ellipse, which contains all of the A_e. Calculating Best number X_b of a snow particle respect to an equivalent disk considering Eq.(2.38) and inserting this to Eq.(2.35), when $A = A_e$ and $D = 2\left(\frac{A_\perp}{\pi}\right)^{1/2}$, the snow particle mass is

$$m = \frac{\pi \eta_a^2 X_b}{8 g \rho_a}\left(\frac{A_e}{A_\perp}\right)^{1/4}. \tag{2.39}$$

This hydrodynamic method is widely used and developed further, either to retrieve the fall velocity or inversely mass of hydrometeors e.g. (Mitchell, 1996; Hanesch, 1999; Khvorostyanov and Curry, 2002, 2005; Mitchell and Heymsfield, 2005; Heymsfield and Westbrook, 2010; Szyrmer and Zawadzki, 2010; Wood et al., 2014; Huang et al., 2015).

The Eq.(2.36) derived in (Böhm, 1989) assumes laminar flow for the falling particle, and in Böhm (1992) an empirical correction factor for drag coefficient was added to explain the turbulent flow for hydrometeors with higher Reynolds number ($R_e \gtrsim 1000$). Also, the axis ratio to particle description was introduced for improving the accuracy of the parametrization, and the rain drops were included in the modeled range. Eq.(2.36) is in an inconvenient form, Mitchell (1996) resolves this by utilizing four experimentally retrieved $R_e(X_b)$ relations for different ranges

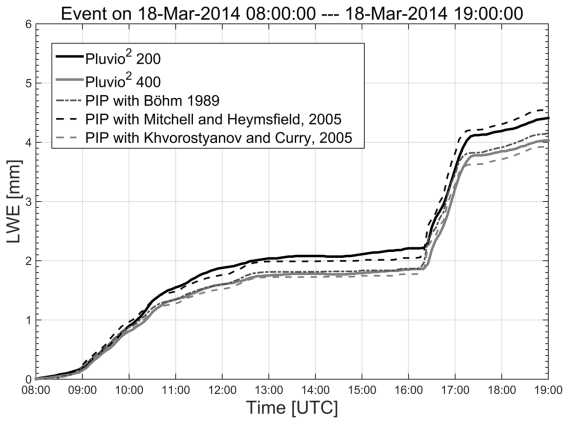

Figure 2.6. An example of the sensitivity of the accumulated snow estimate to selected versions of the hydrodynamic theory in Publication IV.

of X_b and implementing mass- and area-dimensional relations to the definition of fall velocity leading to a convenient power-law representation of fall velocity as $v(D) = a_v D^{b_v}$. The discontinuity of the four $R_e(X_b)$ relations in Mitchell (1996) was parameterized to a continuous $R_e(X_b)$ relation by Khvorostyanov and Curry (2002), and further improved in Khvorostyanov and Curry (2005) by changing the δ_0 and C_0 to the values presented in (Böhm, 1989) and considering the turbulence effect to R_e. Mitchell and Heymsfield (2005) modified the original derivation of $R_e(X_b)$ relation Eq.(2.36) to improve estimates of fall velocities of aggregates

$$R_e = \frac{\delta_0^2}{4}\left[\left(1 + \frac{4X_b^{1/2}}{\delta_0^2 C_0^{1/2}}\right)^{1/2} - 1\right]^2 - a_0 X_b^{b_0}, \tag{2.40}$$

where the second term accounts for the dilation of the boundary layer thickness and increase of affected area projected to the flow. Coefficients are $a_0 = 1.7 \times 10^{-3}$ and $b_0 = 0.8$, and if turbulence correction presented in (Böhm, 1992) is considered, the values are $a_0 = 1.0 \times 10^{-5}$ and $b_0 = 1.0$. Heymsfield and Westbrook (2010) investigated laboratory and field data of falling both snow crystals and snowflakes and suggested a simple adjustment to the solution presented in (Mitchell, 1996). The C_d was modified to consider more precisely snow particles with low area ratio such as aggregates due to their overestimated fall speed related to the data set. New coefficients for δ_0 and C_0 were proposed with values of 8.0 and 0.35, respectively. The modified equation for mass is given by Heymsfield and Westbrook (2010)

$$m = \frac{\pi \eta_a^2 X_b}{8 g \rho_a}\left(\frac{A_e}{A_\perp}\right)^{0.5}. \tag{2.41}$$

Szyrmer and Zawadzki (2010) derived eighth-order polynomial fit for the relations of $R_e(X_b)$ in (Mitchell and Heymsfield, 2005; Khvorostyanov and Curry, 2005). They utilized both of those relations in deriving an ensemble of $m(D)$ estimates, from which they defined the average relation. In Publication IV the two polynomial fits from Szyrmer and Zawadzki (2010) and the first version from Böhm (1989) without turbulence correction was implemented, and different derived estimates of $m(D)$ relations were compared to a gauge-measured liquid water equivalent (LWE) accumulation. An example of the differences is shown in Figure 2.6. The computed accumulated snow estimates of these three versions are producing relatively similar results and in Publication IV the version presented in Mitchell and Heymsfield (2005) was found to correspond best to the data obtained during BAECC (Biogenic Aerosols Effects on Clouds and Climate) -campaign (Petäjä et al., 2016).

2.4.2 Observed and true dimensions of a snow particle

Aerodynamically solid hydrometeors are assumed to fall with their maximum projected area perpendicular to the direction of fall with observations of snow crystals supporting this e.g. (Zikmunda and Vali, 1972; Cho et al., 1981). It is also shown that early snowflakes can fall with unstable spiral motion depending on their non-symmetrical structure (Kajikawa, 1989). Often it is assumed the mean canting angle of 0° (minor axis with respect to the vertical direction) with a standard deviation of 9° defined for single crystals (Matrosov et al., 2005a). Recently Garrett et al. (2015) stated, based on measurements of Multi-Angle Snow Camera (MASC), the mode of orientation angle relative to the horizontal direction for aggregates is 13°, which is notably higher than was shown in (Matrosov et al., 2005a).

For the hydrodynamic calculations, the particle dimensions projected to the flow are needed, but all the ground-based disdrometers observe the falling particles from the side. Depending on the measurement setup the disdrometers are viewing either from one, two or three projection planes and, especially, particle dimensions estimated from one side projection are not necessary descriptive of the true maximum dimensions. Also, particle area observed from the side and the area perpendicular to flow needed for the mass retrieval, can be very different.

The relations between side-view projection of the particle to the cross-section perpendicular to flow has been addressed e.g. in (Schefold, 2004; Szyrmer and Zawadzki, 2010; Wood et al., 2013) and in Publication IV.

Schefold (2004) studied two alternative ways of estimating the difference and compared these to measurements with a video spectrometer (Schefold, 2004). Szyrmer and Zawadzki (2010) combined the results obtained by Schefold (2004) with applying another hypothesis that the area ratio of a particle is independent of the angle of observation. They derived that the maximum observed dimension viewed from the side in respect to the maximum horizontal dimension perpendicular to flow is on average 0.85 and decreasing with increasing size to selected threshold value of 0.75 (Szyrmer and Zawadzki, 2010). Following the approach presented in (Wood et al., 2013) in Publication IV a relation between observed and true particle dimensions is defined by rotating and tilting an ellipsoid and investigating the changes in the relation as a function of different aspect ratios. It was derived that in most snow events the observed maximum diameter is close to 0.82 of the true maximum diameter, which is close to the value derived in (Szyrmer and Zawadzki, 2010). However, it must be noted, in Publication IV the selected value for the ratio between the observed and true maximum diameter also partly corresponds to the limitations of observing area perpendicular to the flow and to the truncation of the observed PSD for smaller particles as discussed in both Publication IV and Publication V.

3. Surface observations

"We must trust to nothing but facts: these are presented to us by Nature and cannot deceive."
Antoine Lavoisier, 1743-1794

This is maybe true, but the instrumentation to measure and our interpretation of Nature are prone to uncertainties and errors. *In situ* measurements, such as aircraft observations of clouds and surface precipitation measurements, are considered the reference for the remote sensing observations, because they are presenting the direct samples of the microphysical properties of interest. They can be utilized to validate retrievals and adjust measurements to correct errors. However, *in situ* have limitations inherently due to the measurement principles, finite sampling volumes and the environmental influence. As a point measurement surface observations are representative only in a limited area and are prominently confined in describing precipitation, which varies both in time and space.

3.1 Liquid equivalent precipitation and snow ratio

A total accumulation of solid precipitation is usually expressed in terms of the vertical depth of liquid water equivalent (LWE) to which it would cover a horizontal plane in a stated time period Δt. Following this definition, LWE accumulation G in mm is

$$G = \frac{10^{-3}}{\rho_w} \int_t^{t+\Delta t} \int_0^{D_{max}} m(D,t) v(D,t) N(D,t) dD dt. \tag{3.1}$$

The precipitation rate is the mass flux, and can be expressed in mmh^{-1} as

$$S(t) = \frac{3.6}{\rho_w} \int_0^{D_{max}} m(D,t) v(D,t) N(D,t) dD. \tag{3.2}$$

3.1.1 Precipitation gauges

Precipitation gauge is the most common instrument used to measure precipitation. There exist many different types of gauges differing in design, shape, size, and material (Sevruk and Klemm, 1989). The orifice area varies from 7 to 1000 cm^2, though most gauges have an area of 100-200 cm^2 (Sevruk and Klemm, 1989). The precipitation is measured either by its volume or mass, for snowfall only the latter is valid. Generally, three types of automatic precipitation recorders are utilized, namely the weighing-recording, the tilting or tipping-bucket, and the float type (Goodison et al., 2014). From those the weighing gauge performs for all types of precipitation, the other two types are limited to rainfall only. The weighing gauge is recording the weight of the container continuously with a spring mechanism or balance weights. The container capacity ranges from 150 to 750 mm (Goodison et al., 2014). The gauge is not automatically emptied; this is a part of the regular maintenance duties.

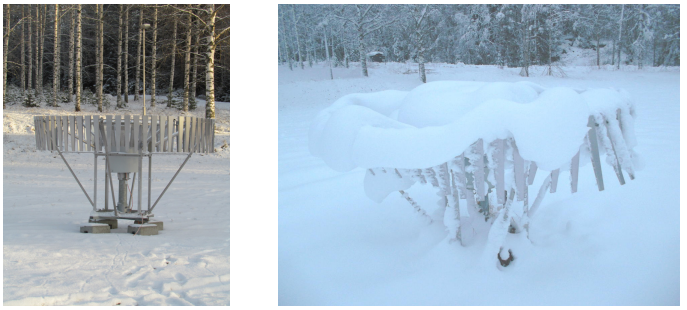

(a) **(b)**

Figure 3.1. a) Precipitation gauge Pluvio^2 400 with Tretyakov and Alter wind shields and b) the same gauge after a snowstorm on 23 November 2015 (Photo by Matti Leskinen).

The possible error sources of the automatic weighing gauges in snowfall are listed in (Michelson, 2004), and mitigating procedures to reduce the errors are presented in (Goodison et al., 1998, 2014). Here is a summary of them.

- Wind induced errors are one of the main sources of uncertainty in the gauge measurements. Especially with snowfall measurements, the catch ratio for unshielded gauges can be less than 60% with wind speeds higher than 4ms^{-1} (Goodison et al., 1998). Wind cause underestimation, as the wind field around the gauge orifice is distorted, preventing some of the precipitation from entering the gauge. For solid precipitation,

the gauges are usually shielded with wind fences to alter the turbulent airflow around the gauge orifice to increase the gauge catch efficiency. Typical structures are so called Alter or Tretyakov wind shields, and the reference gauge for solid precipitation is the gauge known as the Double Fence Intercomparison Reference (DFIR). It has octagonal vertical double fences surrounding a Tretyakov-shielded gauge. Wind induced errors can be corrected with experimental methods.

- Error induced from evaporation. Although the structure of a gauge is designed to reduce evaporative surface area, evaporation causes gradual loss to the measured mass. This can be reduced by adding oil or other evaporation suppressants inside the container to form a film over the water surface. With continuous automatic recording, the effect of evaporation can be estimated.

- Blowing snow can drift inside the gauge if the gauge is improperly sited. The orifice must be placed above the maximum expected depth of snow cover, and preferably even higher to prevent wind-blowing snow from the ground.

- The chosen site is not representative for the surroundings, or it is strongly influencing the catchment leading to non-representative measurements. It is recommended that the gauges should not be located too near forest or trees, which would shelter the gauge from the snowfall. Also in the newest SPICE- intercomparison campaign (WMO SPICE, 2017), it was recommended to install the gauge with the measurement unit towards the north to reduce the warming effect of the sun.

- If the gauge is improperly designed and/or constructed, this could lead to measurement errors. For example in the case where the sensitive weighing sensors are disturbed, from an unstable platform or the oscillation of the balance in strong winds. In winter conditions antifreeze solution must be added preventing liquid to freeze and eliminating ice buildup, which affects the stableness of the container.

- Piling of snow onto the orifice prevents catching of snowfall causing misinterpretations (Figure 3.1). Particularly freezing rain or wet snow can stick to the inside of the gauge orifice and not fall into the bucket

until some time later. Orifice heaters are used to prevent this, but in some cases, they have increased the piling by melting the dry snow to stick even tighter.

In Publication II, Publication III, Publication IV and Publication V two weighing precipitation gauges are utilized to retrieve $\rho(D_0)$ and $m(D)$ relations. These gauges are located at the Hyytiälä measurement site (Petäjä et al., 2016) and the measurement setup is designed to address the challenges of winter precipitation surface measurements. The site is an opening sheltered by boreal forest; hence the local wind conditions are moderate, and the distance of the instruments to the closest trees is more than 10 m. The gauge OTT Pluvio^2 200 with an orifice of 200 cm^2 is located on the platform at a height of 3.5 m inside the double wind fence similar to DFIR (Goodison et al., 1998), in addition the gauge has the Tretyakov wind shield. The Pluvio^2 400, with an orifice of 400 cm^2 at height of 1.5 m, is placed on the field about 20 m from the double wind fence. It has both Tretyakov and Alter wind shields (Figure 3.1). Regular maintenance visits ensure the quality of the gathered data; containers are emptied, antifreeze solution is added in winter period and in the case of piling snow, the formed blockages are cleaned, and a data quality warning can be addressed to the time period in question.

3.1.2 Acoustic and optic snow depth sensors

Snowfall depth describes the depth of freshly fallen snow deposited over a specified period on a horizontal plate, and it is usually expressed in cm. The term snow here also includes other forms of winter precipitation such as ice pellets, glaze, hail and sheet ice formed from precipitation, but the definition excludes the deposition of drifting or blowing snow. Whereas snow depth means the total depth of snow on the ground at the time of observation, also expressed in cm.

Manually snow depth is measured with a ruler or similar graduated rod, which is pushed down through the snow to the ground surface (Goodison et al., 2014). Snow drifts with wind forming piles, and in a forested area, falling snow is partly attached to the tree canopy, and due to canopy shade, the melting progresses unevenly. Snow cover changes constantly through snow particle metamorphosis, and depth decreases because of the settlement and packing by the wind (Gray and Male, 1981). Therefore, the depth of the snow cover is nonuniform, and for a representative measurement,

several vertical measurements should be averaged.

At automatic weather stations, ultrasonic ranging devices provide snow depth measurements with a temporal resolution of minutes. The sensor sends out an acoustic (typically around 50 kHz) sound pulse and measures the time it takes to travel to the ground and to reflect back. The duration of the returned pulse is adjusted for the speed of sound in the air based on measured air temperature (Ryan et al., 2008). This is a point measurement, and thus may not be spatially representative, and misreadings can be introduced from wind driven snow or random branches or leaves. Compared to manual measurements, the acoustic sensors tended to underestimate the total snow depth by approximately 2 cm (Ryan et al., 2008). This is mostly attributed to spatial variability of the snow cover. A similar measurement can be performed with optical sensors, which measure the snow depth by comparing signal phase information of the modulated visible laser light. The $\rho(D_0)$ relations in Publication III are retrieved with video disdrometer Particle Imaging Package (PIP) and gauge measurements, and these are validated against to hourly measured change in the snow depth by estimating the volume-flux from the relations. The snowflakes were assumed as spheroids with an axis ratio of 0.6 (Matrosov, 2008) and with a conversion factor the volume equivalent diameter was determined. The volume flux in mms^{-1} can be written as a function of the fall velocity, PSD and volume equivalent diameter

$$U(t) = 10^{-6} \int_0^{D_{max}} \frac{\pi}{6} D^3 v(D,t) N(D,t) dD. \tag{3.3}$$

Given that freshly fallen snowfall depth was estimated, the packing efficiency was assumed to be 100% and compression was ignored. The correspondence between the estimated snow volume and change in snow depth was good, and this confirmed the derived ensemble mean densities.

3.1.3 Snow ratio

Snow ratio (S_r) describes the ratio of snowfall depth to LWE accumulation, and it is inversely proportional to the snow density if packing of snow on the ground is not considered. This ratio is typically assumed to be about 10:1, but there are variations depending on temperature, humidity, compaction and wind conditions. The values can range from 3:1 to 100:1 in different data sets (Roebber et al., 2003; Ware et al., 2006). Power et al. (1964) established a link between the snow accumulation to snow density and reported the influence of riming in increasing the snowfall density.

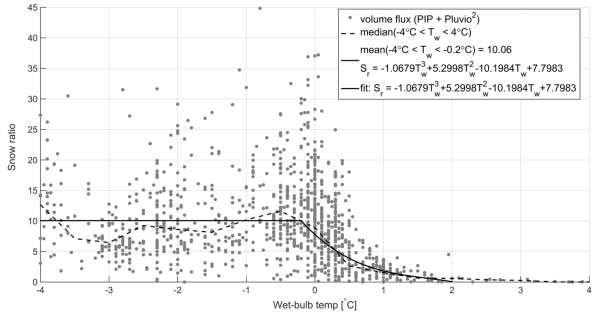

Figure 3.2. Snow ratio S_r as a function of humidity and temperature (T_w as the wet-bulb temperature) defined from the estimated volume flux based on video-disdrometer PIP measurements for 95 snow events during winters 2014-2015.

Roebber et al. (2003) identified seven environmental factors, which affect the value of snow ratio; the most important were the month, temperature, and external compaction, and relative humidity information was of lesser significance. They aimed to improve the snow depth forecasting by using numerical weather prediction models. Snow density was grouped to three classes, which are based on snow ratio; heavy (1:1-9:1), average (9:1 - 15:1), and light ($>$ 15:1). Ware et al. (2006) examined snow ratios measured from the 24-h accumulations over the U.S. continent during 21 years. With 1650 studied snowfall events they found a median value of 14.1:1, the mean value 15.6:1 and the mode value to be close to the commonly assumed 10:1. According to Ware et al. (2006), the snow ratio tends to increase with decreasing temperature and decreasing liquid equivalent precipitation rate.

In Publication III, snow ratio is determined from the volume flux (Eq.(3.3)) measured with PIP. The derived mean value is 10.1:1 and median 9.0:1. Though, it should be noted, that the packing efficiency and compression of the snowflakes on the ground were not considered. This method has been utilized for determining the change in the snow ratio as a function of humidity and temperature (Figure 3.2). The practical application is for airport maintenance to help decide the appropriate maintenance procedures of cleaning the runways. At the airport snow cover is frequently removed; thus the significance of packing and compression can be assumed to be small.

3.2 Disdrometers

Disdrometers are automatic instruments providing PSD measurements. The modern instruments can also measure fall velocity and an estimate of shape for an individual hydrometeor. Disdrometer data is used, in addition to measure PSD, for hydrometeor classification, snow rate measurements, and particle mass retrievals (as explained in Section 2.4). Detailed characteristics of a snow particle are needed to define its scattering properties. Data can be applied to construct the corresponding link from the surface observations to remote sensing measurements and to improve microphysical parameterizations in numerical weather prediction models. Figure 3.3 shows pictures of different disdrometers located in Hyytiälä measurement site.

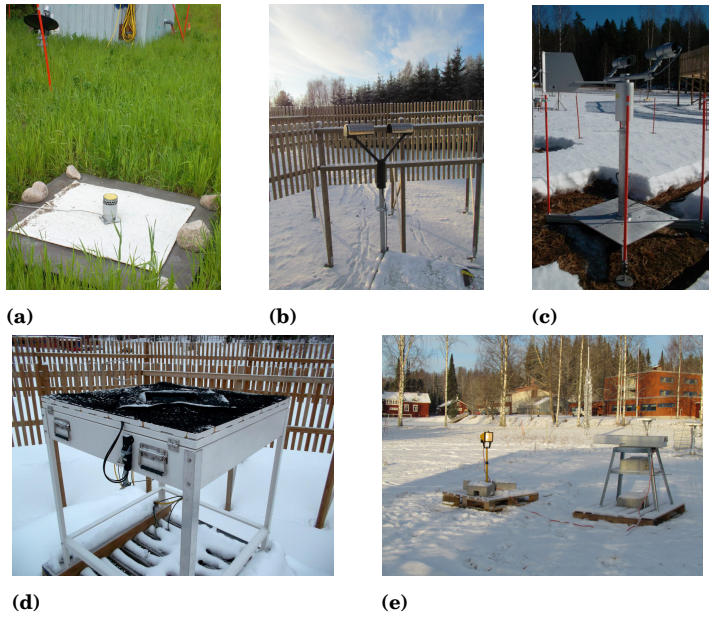

Figure 3.3. Different disdrometers at the Hyytiälä measurement site a) Joss-Waldvogel disdrometer b) PARSIVEL, c) Holographic Hydrometeor Imager, d) 2D-video disdrometer and e) Particle Imaging Package. Photo credits: a), c) and d) are taken by Matti Leskinen.

One of the older designs, but actively used disdrometers is **Joss-Waldvogel disdrometer (JWD)**. It has been commercially available for almost 50 years (Joss and Waldvogel, 1967) and it is often considered to be a reference instrument for PSD measurements in rain. JWD is an impact-type electromechanical counter with a sampling cross-sectional area of 50 cm^2 (Tokay et al., 2001). The sensor consists of a cylindrical metal housing containing an electromechanical transducer and an amplifier module. The

sensor transforms the mechanical momentum of an impacting drop to an electrical pulse. It can measure the drop size with a 5% accuracy, and drops are sorted into 20 size intervals ranging from 0.3 to about 5.0–5.5 mm (Tokay et al., 2001). JWD underestimates the number of small drops in heavy rain due to the automatic threshold for monitoring noise level (Tokay and Short, 1996). Small drops are also suppressed with strong background noise, as noise level reaches 55 dB; the detection of the drop diameters of 0.3 to 0.4 mm are significantly underestimated (Tokay et al., 2001). Furthermore, with drops larger than 5.0 to 5.5 mm, the diameter cannot be distinguished by JWD. The size measurement retrieval is calibrated to raindrops falling at their terminal fall speed, and thus vertical air motion influencing the fall speeds results in an error of the measured drop size. From the same reason, JWD cannot be used for snowfall measurements. In Publication I, JWD provides PSD in rain below the melting layer.

PARticle SIze VELocity (PARSIVEL) disdrometer was originally designed for liquid precipitation (Löffler-Mang and Joss, 2000). It is a laser sensor that produces a horizontal flat laser sheet between the emitter and the receiver. The used wavelength is 650 nm, and the measurements area is 180 mm x 30 mm (54 cm^2). At the receiving end, a photo diode converts the received light into electric voltage, and as the falling particle passes through the laser, it blocks off a portion of the light proportional to its size. Thus the reduced voltage output can be related to the diameter of the particle. Fall velocity is derived from the duration that the particle is dimming the laser sheet, assuming a fixed ratio between horizontal and vertical dimensions (Battaglia et al., 2010a). PARSIVEL can measure sizes from 0.2 mm up to about 25 mm, and fall velocity range is 0.2 - 20 ms^{-1}. Löffler-Mang and Blahak (2001) demonstrated that radar reflectivity factor in snowfall can be retrieved with reasonable accuracy from PSD measured by PARSIVEL, and Yuter et al. (2006) classified snow, wet snow, and rain particles based on their size and fall speed properties with PARSIVEL data. Battaglia et al. (2010a) described the limitations of PARSIVEL's measurement principle in snowfall. They concluded that the observed diameter, namely maximum horizontal diameter, has shortcomings in describing irregular particles due to internally assumed dependence between horizontal and vertical dimensions. Therefore this causes errors, over- and underestimation depended on the particle size, both in the retrieved velocity and PSD output. Also if large snowflakes are falling close to the laser-sheet border, the partially seen particles are counted smaller in size,

and this border effect artificially increases the concentration of the smaller particles (Battaglia et al., 2010a).

Many of the automatic snow observations have been performed with **Hydrometeor Velocity and Shape Detector (HVSD)** (Barthazy et al., 2004) and **2D-video disdrometer (2DVD)** (Kruger and Krajewski, 2002; Schönhuber et al., 2007). The measurement principle is the same in both instruments, except HVSD is viewing the falling particles from one direction and 2DVD from two orthogonal directions. The instruments consist of two horizontally oriented line-scan cameras illuminated with incoherent uniform light. The light sheets are vertically separated by an offset of around 6 mm for 2DVD and around 9 mm for HVSD. The falling particle casts a shadow related to its size on a horizontal array of line camera's photodetectors, and stacking the data from the recorded shadowed detectors, a contour image of the particle can be constructed. The fall velocity is obtained from the time interval for a particle to fall from one light sheet to the other, and thus this requires automatic matching of the two corresponding contour images. With HVSD matching is more straightforward from a single projection. With 2DVD it is more challenging as the complex structure of snow particles appears different from the two observation projection. The improved matching or rematching algorithms are created for 2DVD in (Hanesch, 1999; Huang et al., 2010; Bernauer et al., 2015). The benefit of two projections is more comprehensive description of the particle shape. For accurate velocity measurements, the vertical distance of the two light planes should be precise, and the uncertainty in measured velocity values influences the resulting PSD. With 2DVD the exact position of the light planes is determined with a manual calibration process by dropping metal spheres of distinct sizes from a certain height. Instruments with line sensors have shortcomings with wobbling and rotating particles; the resulting constructed image is suffering from distortions, and this is enhanced in windy conditions. For this reason, for example, in (Bernauer et al., 2016) only snow events with wind velocities below 5 ms^{-1} are considered. The measurement area of 2DVD is approximately 100 mm x 100 mm, and the area of HVSD is 81 mm x 72 mm. Although the resolution of 2DVD is reported to be 0.2 mm (Kruger and Krajewski, 2002), Bernauer et al. (2015) recommended that the reliable size and shape observations can be obtained for particles larger than 0.5 mm.

HVSD has been applied for studying the fall velocity of snowflakes, as a function of riming degree in (Barthazy and Schefold, 2006). Zawadzki

et al. (2010) studied the natural variability of snowflake fall velocities and connecting these to environmental factors such as the surface temperature, echo-top temperature, and depth of precipitation system. They also addressed the instrumental uncertainties. Szyrmer and Zawadzki (2010) determined an approximate relation between the factors of $m(D)$ and $v(D)$ relation for aggregates by calculating snowflake masses with hydrodynamic theory from the HVSD data.

2DVD was utilized in several studies to obtain the $m(D)$ or $\rho(D)$ relation either using hydrodynamic theory (Huang et al., 2015; Bringi et al., 2017) or combining the size and velocity information with radar data (Huang et al., 2010) or gauge measurements (Brandes et al., 2007). Wood et al. (2014) introduced a Bayesian optimal estimation retrieval for constraining microphysical properties of dry snow by integrating multi-instrumen-tal observations; the size-resolved fall speeds and volume estimates of snow particles were obtained with 2DVD. The snowflake shape characteristics influencing the fall velocity were investigated in (Hanesch, 1999). The relation between the fall velocity of aggregates and temperature at the ground is proposed in Brandes et al. (2008), as the higher temperatures are associated with potentially increased concentration of supercooled liquid aloft, and through riming process, the fall speeds are observed to increase with temperature. Zhang et al. (2011a) calculated the polarimetric radar parameters using data measured with 2DVD. Lately, 2DVD data is applied for hydrometeor classification in (Grazioli et al., 2014; Gavrilov et al., 2015; Lee et al., 2015; Bernauer et al., 2016).

Multi-Angle Snowflake Camera (MASC) is a recently introduced instrument taking high-resolution photographs of hydrometeors in three different angles separated by 36° (Garrett et al., 2012). The distance of the focal point to each camera is circa 10 cm, and the measuring cross section is approximatively 2.5 cm^2. The resolution of the stereographic photographs is 9 to 37 micron, and a detailed structure of the snow particles can be distinguished as shown in Figure 2.2, where the accreted small supercooled cloud droplets on snowflake are clearly seen. The instrument also includes a system of near-infrared emitter-detector pairs, arranged in two arrays that are separated vertically by 32 mm. Fall speed is retrieved from the time it takes a hydrometeor to fall the distance between the upper and lower triggering array. MASC has been applied to study the hydrometeors characteristics, such as type, aspect ratio, orientation and fall speed, and how these properties are affected with riming (Garrett and Yuter, 2014;

Garrett et al., 2015). MASC has been utilized in hydrometeor classification (Praz et al., 2017), where the algorithm could benefit from the texture features visible in the images for defining the degree of riming. One of the shortcomings of the instrument is its small measurement volume, which results in truncation of the measured PSD. In (Garrett and Yuter, 2014), the fall velocity of rimed particles was studied, and a strong peak value in distribution was observed in fall speeds around 1 ms^{-1}. There is speculation that the instrument case could distort the wind field by generating local turbulence in the presence of horizontal winds (Garrett et al., 2015).

Holographic Hydrometeor Imager (HHI) is also one of the new instruments measuring hydrometeor characteristics and fall velocity (Kaikkonen et al., 2014; Kaikkonen and Mäkynen, 2016). The imaging method is based on in-line holography with plane wave illumination. The image resolution is approximately 20 microns, and the measurable fall velocity range is 0.1 to 4 ms^{-1}. The latest developed version has a measurement volume of 670 cm^3. One of the interesting inventions of HHI is a vertical tail wing at the backside of the instrument, which rotates it according to the wind. The wing is designed to turn the longest side of the measurement volume against the wind direction, which is ideal for sampling. So far the usability of the instrument has been limited because of the computational cost and the data transfer has a constraint on continuous measurements during snowfall.

Particle Imaging Package (PIP) is the new generation of the Snowflake Video Imager (SVI) (Newman et al., 2009). The measurement principle is the same. A 2D-gray scale video image is recorded from a falling hydrometeor as it falls between a charge-coupled device (CCD) camera and background light (Newman et al., 2009). SVI could not measure the fall velocity, but because of the higher frame rate (380 fps (frames per second)) of the PIP camera, the fall velocity can be retrieved from the consecutive observed frames. For PIP the particle sizes are recorded in the range of 0.2 - 26 mm with the resolution of 0.2 mm in the current software version. The field of view (48 x 64 mm) of PIP is larger than with the SVI (24 m x 32 mm). The measurement volume is defined by the field of view and the depth of field. The depth of field is dependent on the particle diameter and defined by the processing software either rejecting or not detecting particles that are out of focus. The expected particle size error due to the blurring effect is 18 %, and for SVI the depth of field is approximately 117 times the particle equivalent diameter (Newman et al., 2009). In the

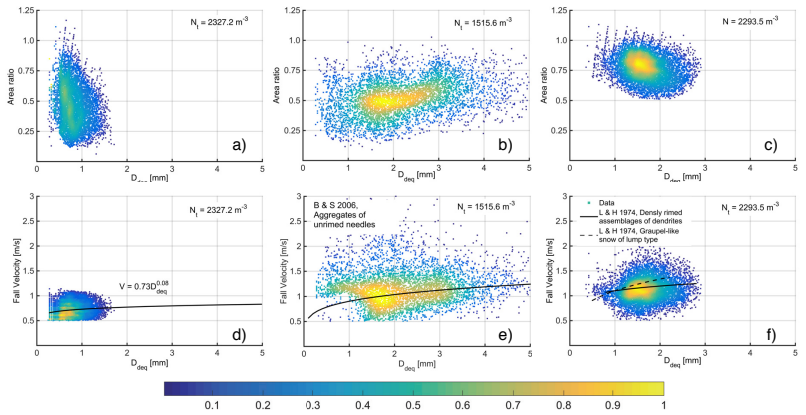

Figure 3.4. PIP observations of three ensembles of particles separated by clustering. Density plots of retrieved area ratios and observed fall velocities as functions of diameter with the estimated number concentrations. Small needle-like particles are shown in a) and d) with $v(D)$ relation defined with nonlinear regression. Aggregates are depicted in b) and e), and the $v(D)$ relation is taken from (Barthazy and Schefold, 2006). Rimed particles are shown in c) and f) when $v(D)$ relations are for densely rimed assemblages of dendrites and graupel-like snow of lump type taken from (Locatelli and Hobbs, 1974), published with permission (Sinclair et al., 2016).

current algorithm, particles smaller than 14 pixels are rejected, effectively meaning that particles smaller than disk-equivalent diameter ≈ 0.2 mm are not observed. Given that the measurement volume of PIP/SVI is not enclosed, the expected effects in calm to moderate wind conditions on measurements of particle PSD are modeled to be minimal (Nešpor et al., 2000).

In (Moisseev et al., 2015) images of snowflakes recorded by SVI were utilized to identify particle type and in (Huang et al., 2010) SVI was acting as a reference for PSD measurements when 2DVD was suffering from under-catchment due to the matching challenges. In Publication II and Publication III the $\rho(D_0)$ relations were retrieved by combining fall velocity and PSD measurements of PIP with precipitation gauge observations. The snowflake images were used as confirmation of the observed triple-frequency radar signatures in Publication II. The retrieved $\rho(D_0)$ relation was also utilized in (Moisseev et al., 2017) for determining the rime mass fraction in snowfall following the approach of a single ice-phase category microphysical scheme in numerical weather prediction (NWP) models. The mass retrieval with PIP data was performed based on hydrodynamic theory in Publication IV and Publication V. Figure 3.4 shows an example, where ensembles of particle types in snowfall were classified by clustering according to the microphysical properties of fall velocity, diameter and

shape characteristics observed with PIP. In (Sinclair et al., 2016) this particle type identification verified the presence of secondary ice production observed with the polarimetric radar.

3.2.1 Comparison of disdrometers

PIP is the main surface instrument utilized in this research. The main benefit of PIP is the large and open sampling volume, which provides representative PSDs also in moderate wind conditions. 2DVD and HVSD have challenges in matching observations of the two measurement levels, and the shortcoming of MASC is its small sampling volume. PIP records videos, and thus rotation and wobbling of snowflakes is also recorded, and the effect on dimension measurements can be retrieved and quantified, whereas with the line-scan type of instruments the distortion is inherently in the data. The resolution of PIP images is not as accurate as with images of MASC and too coarse for detailed particle classification. One of the advantages of PIP is its robustness when compared to 2DVD. Once aligned properly and positioned on a stable platform, the only maintenance services needed are changing lamp yearly and clearing snow in case of piling. For 2DVD the rather cumbersome calibration procedure to estimate the light plane offset should be repeated approximately every six months.

4. Basic theory of electromagnetic scattering of snow particles

"It certainly cannot result in an organism such as a horse, which is not spherically symmetrical."
Alan Turing, The Chemical Basis of Morphogenesis, 1952.

For modeling remote sensing observations of winter precipitation, the electromagnetic scattering properties of snow crystals and snowflakes are required. Snow crystals and snowflakes are not spherically symmetrical, and thus some approximation must be applied to retrieve a solution. This chapter presents the basic scattering theory of a single particle, and briefly explains the main computational methods used to estimate the scattering properties of a single particle. It also gives reasoning, when it is justified to compute the scattering properties assuming the snowflake as a spherical particle and when this approximation fails.

4.1 Electromagnetic scattering of a single particle

Single scattering approximation can be used when other scatterers are sufficiently far-away, and no multiple-scattering effects between them need to be considered. The boundary distance is dependent on scatterer size and the wavelength of the electromagnetic field. The assumption of single scattering applies to falling snow in the lower microwave frequency regions (S, C, and X), but at higher frequencies (f > Ku), the multiple scattering effects can be observed (Battaglia et al., 2010b).

In remote sensing, the observed target locates in the far-field of the radiating electromagnetic source, and it can be approximated that an incident electromagnetic wave travels in homogeneous and isotropic space and impinges upon a single scatterer. Given a non-magnetic scatterer, e.g. snow crystal or snowflake, it has a permittivity $\varepsilon_s(\bar{r}) = \varepsilon_0 \varepsilon_r(\bar{r})$, $\varepsilon_r(\bar{r})$

being the relative permittivity, and a permeability $\mu_s(\bar{r}) = \mu_0$. Given that all electric and magnetic fields are assumed to be time harmonic and can be stated as $\bar{E}(\bar{r})\, e^{j\omega t}$ and $\bar{H}(\bar{r})\, e^{j\omega t}$, with an angular frequency of $\omega = 2\pi f$, the dependence $e^{j\omega t}$ is suppressed in the following equations. Incident electric field $\bar{E}^{inc}(\bar{r})$ and magnetic field $\bar{H}^{inc}(\bar{r})$ are the solution of Maxwell's equations in the homogeneous space with the radiating source lying outside the space, and the total fields $\bar{E}^{tot}(\bar{r})$ and $\bar{H}^{tot}(\bar{r})$ are the solution of Maxwell's equations in the inhomogeneous space with $\varepsilon(\bar{r})$ and $\mu(\bar{r})$, when the scatterer is present. The total fields are

$$\bar{E}^{tot}(\bar{r}) = \bar{E}^{inc}(\bar{r}) + \bar{E}^{s}(\bar{r}) \tag{4.1}$$

$$\bar{H}^{tot}(\bar{r}) = \bar{H}^{inc}(\bar{r}) + \bar{H}^{s}(\bar{r}), \tag{4.2}$$

where $\bar{E}^{s}(\bar{r})$ and $\bar{H}^{s}(\bar{r})$ are the scattered fields.

The problem is to determine the unknown scattered and internal fields with respect to the known incident fields. It is assumed that the medium around the scattering particle is air (ε_0, μ_0) and thereby the incident fields are defined according to Maxwell's equations

$$\nabla \cdot \bar{E}^{inc}(\bar{r}) = 0 \tag{4.3}$$

$$\nabla \cdot \bar{H}^{inc}(\bar{r}) = 0 \tag{4.4}$$

$$\nabla \times \bar{E}^{inc}(\bar{r}) = -j\omega\mu_0 \bar{H}^{inc}(\bar{r}) \tag{4.5}$$

$$\nabla \times \bar{H}^{inc}(\bar{r}) = j\omega\varepsilon_0 \bar{E}^{inc}(\bar{r}). \tag{4.6}$$

Moreover, Eq.(4.5) and (4.6) for the total fields are

$$\nabla \times \bar{E}^{tot}(\bar{r}) = -j\omega\mu(\bar{r})\, \bar{H}^{tot}(\bar{r}) \tag{4.7}$$

$$\nabla \times \bar{H}^{tot}(\bar{r}) = j\omega\varepsilon(\bar{r})\, \bar{E}^{tot}(\bar{r}). \tag{4.8}$$

Subtracting Eq.(4.5) from Eq.(4.7) and Eq.(4.6) from Eq.(4.8)

$$\begin{aligned} &\nabla \times \left(\bar{E}^{tot}(\bar{r}) - \bar{E}^{inc}(\bar{r})\right) = -j\omega\mu(\bar{r})\, \bar{H}^{tot}(\bar{r}) - \left(-j\omega\mu_0 \bar{H}^{inc}(\bar{r})\right) \\ &= -j\omega\mu_0 \left(\bar{H}^{tot}(\bar{r}) - \bar{H}^{inc}(\bar{r})\right) - j\omega\left(\mu(\bar{r}) - \mu_0\right) \bar{H}^{tot}(\bar{r}) \end{aligned} \tag{4.9}$$

$$\begin{aligned} &\nabla \times \left(\bar{H}^{tot}(\bar{r}) - \bar{H}^{inc}(\bar{r})\right) = +j\omega\varepsilon(\bar{r})\, \bar{E}^{tot}(\bar{r}) - j\omega\varepsilon_0 \bar{E}^{inc}(\bar{r}) \\ &= j\omega\varepsilon_0 \left(\bar{E}^{tot}(\bar{r}) - \bar{E}^{inc}(\bar{r})\right) + j\omega\left(\varepsilon(\bar{r}) - \varepsilon_0\right) \bar{E}^{tot}(\bar{r}) \end{aligned} \tag{4.10}$$

from which the scattered fields can be determined according to Eq.(4.1) and Eq.(4.2)

$$\nabla \times \bar{E}^{s}(\bar{r}) = -j\omega\mu_0 \bar{H}^{s}(\bar{r}) - j\omega\left(\mu(\bar{r}) - \mu_0\right) \bar{H}^{tot}(\bar{r}) \tag{4.11}$$

$$\nabla \times \bar{H}^{s}(\bar{r}) = j\omega\varepsilon_0 \bar{E}^{s}(\bar{r}) + j\omega\left(\varepsilon(\bar{r}) - \varepsilon_0\right) \bar{E}^{tot}(\bar{r}). \tag{4.12}$$

Also, the scattered fields satisfy Maxwell's equations. Inside the particle, the incident field induces an apparent electric current $\bar{J}$ and this current generates then the scattering electromagnetic field. The particle operates like an antenna, and its scattering energy is lost from the incident wave. Considering magnetic and electric current sources

$$\bar{M}(\bar{r}) = j\omega(\mu(\bar{r}) - \mu_0)\bar{H}^{tot}(\bar{r}) \tag{4.13}$$

$$\bar{J}(\bar{r}) = j\omega(\varepsilon(\bar{r}) - \varepsilon_0)\bar{E}^{tot}(\bar{r}). \tag{4.14}$$

and, as already stated, the magnetic current is zero $(\mu(\bar{r}) - \mu_0 = 0)$. Taking a curl $(\nabla\times)$ of Eq.(4.11) and combing it with Eq.(4.12), the scattered electric field is

$$\nabla \times \nabla \times \bar{E}^s - k_0^2 \bar{E}^s = k_0^2(\varepsilon_r(\bar{r}) - 1)\bar{E}^{tot}. \tag{4.15}$$

where wavenumber in the vacuum is $k_0 = \omega\sqrt{\epsilon_0\mu_0} = \frac{2\pi}{\lambda}$ and λ is the wavelength. If the electric current source is equal to zero, the equation Eq. (4.15) becomes the vector Helmholtz equation. The vector Helmholtz equation at an observation point $\bar{r}$ can be solved for a point source located at $\bar{r}'$ with the dyadic Green's function (Tsang et al., 2000)

$$\bar{\bar{G}}_0(\bar{r},\bar{r}') = \left(\bar{\bar{I}} + \frac{1}{k_0^2}\nabla\nabla\right)\frac{e^{-jk_0|\bar{r}-\bar{r}'|}}{4\pi|\bar{r}-\bar{r}'|} \tag{4.16}$$

and the solution for a general source is found from the convolution of the Green's function with the source (Tsang et al., 2000)

$$\bar{E}^s(\bar{r}) = -j\omega\mu_0\int_V \bar{\bar{G}}_0(\bar{r},\bar{r}')\cdot\bar{J}(\bar{r}')dV' \tag{4.17}$$

$$= -k_0^2\int_V \left(\bar{\bar{I}} + \frac{1}{k_0^2}\nabla\nabla\right)\frac{e^{-jk_0|\bar{r}-\bar{r}'|}}{4\pi|\bar{r}-\bar{r}'|}\left(\varepsilon_r(\bar{r}') - 1\right)\bar{E}^{tot}(\bar{r}')\,dV'. \tag{4.18}$$

In remote sensing the incident electromagnetic field is far-away from its source; the strength of the field decreases inversely with distance and no reactive or radiative effects of the near-field need to be taken into account. In the far-field, the originally spherical wavefront can be considered as a plane wave, where the wavefront is a plane perpendicular to the direction of propagation. The Green's function Eq.(4.16) in the far-field ($r = R >> r'$) can be approximated as

$$\lim_{r\to\infty}\bar{\bar{G}}_0(\bar{r},\bar{r}') = \left(\bar{\bar{I}} - \bar{k}_s\bar{k}_s\right)\frac{e^{-jk_0R}}{4\pi R}e^{-jk_0\bar{k}_s\cdot\bar{r}'} \tag{4.19}$$

and the scattered electronic field in the far-field is (Tsang et al., 2000)

$$\bar{E}^s(\bar{k}_s) = -\frac{k_0^2}{4\pi}\frac{e^{-jk_0R}}{R}\int_V\left(\varepsilon_r(\bar{r}') - 1\right)\bar{k}_s\times\left(\bar{k}_s\times\bar{E}^{\mathrm{tot}}(\bar{r}')\right)e^{-jk_0\bar{k}_s\cdot\bar{r}'}dV'$$

$$= f\left(\bar{k}_s,\bar{k}_i\right)\frac{e^{-jk_0R}}{R}, \tag{4.20}$$

where $f(\bar{k}_s, \bar{k}_i)$ is the scattering amplitude. The scattering amplitude relates the incident electric field to the scattered field and describes proportionality of the field from direction $\bar{k}_i$ into direction $\bar{k}_s$.

4.2 Basic scattering parameters

If $\bar{k}_i$ is the propagation direction, then the linearly polarized incident electric plane wave can be written as (Tsang et al., 2000)

$$\bar{E}^{inc} = \bar{e}_i E_0 e^{-jk_0 \bar{k}_i \cdot \bar{r}}, \tag{4.21}$$

where $\bar{e}_i$ is a unit vector in the direction of the polarization (perpendicular to $\bar{k}_i$) with amplitude E_0. The scattered wave is then

$$\bar{E}^s = \bar{e}_s f(\bar{k}_s, \bar{k}_i) E_0 \frac{e^{-jk_0 R}}{R}, \tag{4.22}$$

where the unit vector of the scattered field is $\bar{e}_s$ (perpendicular to propagation direction $\bar{k}_s$). The magnetic field associated with the incident wave is (Tsang et al., 2000)

$$\bar{H}^{inc} = \frac{1}{\eta} \bar{k}_i \times \bar{E}^{inc}, \tag{4.23}$$

where $\eta = \sqrt{\mu/\epsilon}$ is the wave impedance. The **Poynting vector** represents the directional energy flux density, and for the incident wave it is

$$\bar{S}^{inc} = \frac{1}{2} \Re \left(\bar{E}^{inc} \times \bar{H}^{inc,*} \right) = \frac{|E_0|^2}{2\eta} \bar{k}_i \tag{4.24}$$

and for the scattered wave it is

$$\bar{S}^s = \frac{1}{2} \Re \left(\bar{E}^s \times \bar{H}^{s,*} \right) = \frac{\left|\bar{E}^s\right|^2}{2\eta} \bar{k}_s = \frac{\left|\bar{E}_0\right|^2 \left|f(\bar{k}_s, \bar{k}_i)\right|^2}{2\eta R^2} \bar{k}_s. \tag{4.25}$$

The scattered power can be retrieved by integrating over scattered angle

$$P_s = \int \left|\bar{S}^s\right| R^2 d\Omega_s = \int \frac{\left|\bar{E}_0\right|^2 \left|f(\bar{k}_s, \bar{k}_i)\right|^2}{2\eta} d\Omega_s = \int \left|\bar{S}^{inc}\right| \left|f(\bar{k}_s, \bar{k}_i)\right|^2 d\Omega_s, \tag{4.26}$$

where $d\Omega_s$ is the differential solid angle. The **scattering cross-section** is

$$\sigma_s = \int \left|f(\bar{k}_s, \bar{k}_i)\right|^2 d\Omega_s. \tag{4.27}$$

The electromagnetic wave suffers power loss not only because of scattering, but also due to absorption. The absorbed power by a small particle with a volume V is (Tsang et al., 2000)

$$P_a = \frac{1}{2} \omega V \Im(\epsilon_r) \left|\bar{E}^{tot}\right|^2 \tag{4.28}$$

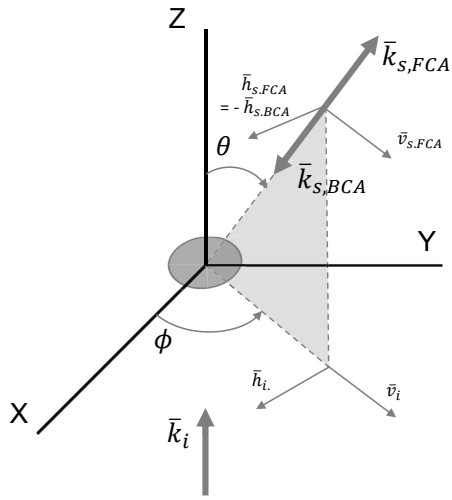

Figure 4.1. Scattering plane defined by the incident wave vector $\bar{k}_i$ and the scattered wave vector $\bar{k}_s$ with the scattering particle centered in origin.

and the **absorption cross-section**

$$\sigma_a = \frac{P_a}{\frac{1}{2\eta}\left|\bar{E}^{inc}\right|^2}. \tag{4.29}$$

The total attenuation, also called the extinction, is the sum of the scattering and absorption cross-sections. Thus the **extinction cross-section** is (Ishimaru, 1978)

$$\sigma_e = \sigma_a + \sigma_s = \frac{-4\pi}{k_0}\Im\left[f(\bar{k}_i, \bar{k}_i)\cdot\bar{e}_i\right], \tag{4.30}$$

where $f(\bar{k}_i, \bar{k}_i)$ is the forward scattering amplitude.

The wave vectors $\bar{k}_i$, $\bar{k}_s$ define the **scattering plane** in 3D-space with a scattering particle centered in origin and direction of scattering is determined by the **scattering angles**; θ between the direction of propagating incident and scattered wave on the scattering plane and ϕ perpendicular to θ in azimuthal direction (Figure 4.1). Given $\phi = 0°$, $\theta = 0°$ describes the forward-scattering and $\theta = 180°$ the backscattering.

The **linearly polarized** incident electrical field Eq.(4.21) and the consequential scattered field Eq.(4.22) can be written with two linearly independent vectors that are perpendicular to propagation $\bar{k}_i$ and $\bar{k}_s$

$$\bar{E}^{inc} = \left(\bar{v}_i E_v^{inc} + \bar{h}_i E_v^{inc}\right) e^{-jk_0\bar{k}_i\cdot\bar{r}} \tag{4.31}$$

$$\bar{E}^{s} = \left(\bar{v}_s E_v^{s} + \bar{h}_s E_h^{s}\right) \frac{e^{-jk_o R}}{R} \tag{4.32}$$

in which the h stands for horizontal and v for vertical polarization components. The directions ($\bar{k}_i$, $\bar{v}_i$, $\bar{h}_i$) are orthogonal unit vectors in the

Cartesian coordinate system (X, Y, Z) following a right-hand rule, thus $\bar{k}_i = \bar{v}_i \times \bar{h}_i$. There are two conventions to determine the scattering direction in forward scatter (FSA) or backscatter alignment (BSA) (Bringi and Chandrasekar, 2001). In FSA the triplet is defined $\bar{k}_{s,FSA} = \bar{v}_s \times \bar{h}_s$, whereas in BSA the scattering direction is towards the observation point and $\bar{k}_{s,BSA} = -\bar{k}_{s,FSA} = \bar{v}_s \times -\bar{h}_s$. The **scattering amplitude matrix** can be written according to Eq.(4.20)

$$\begin{bmatrix} E_h^s \\ E_v^s \end{bmatrix} = \frac{e^{-jk_0R}}{R} \begin{bmatrix} f_{hh}\left(\bar{k}_s, \bar{k}_i\right) & f_{hv}\left(\bar{k}_s, \bar{k}_i\right) \\ f_{vh}\left(\bar{k}_s, \bar{k}_i\right) & f_{vv}\left(\bar{k}_s, \bar{k}_i\right) \end{bmatrix} \begin{bmatrix} E_h^{inc} \\ E_v^{inc} \end{bmatrix}, \tag{4.33}$$

with co-polarized (f_{vv}, f_{hh}) and cross-polarized (f_{vh} ,f_{hv}) scattering amplitudes. For radar applications, the BSA convention has benefits, as for a monostatic radar the scattering matrix is symmetric. For example the scattering amplitude matrix of a sphere, which is a good model for small liquid water droplets, in backscattering direction is a unit matrix (Bringi and Chandrasekar, 2001). The connection between the alignments is (Bringi and Chandrasekar, 2001)

$$f_{BSA} = \begin{bmatrix} -1 & 0 \\ 0 & 1 \end{bmatrix} f_{FSA} \tag{4.34}$$

4.3 Effective Medium Approximation

In a basic definition, dielectric materials have no free charges as electrical conductors do, and therefore they do not conduct electricity. When the dielectric material is exposed to an electric field, the bounded charges are slightly displaced from their equilibrium positions, i.e. polarized, with a net displacement of positive charges into the direction of the electric field and electrons into the opposite direction, but the net charge is zero (Sihvola, 1999). This creates an internal electric field that reduces the overall field within the dielectric itself. A separation of the charges is equivalent to the dipole moment, and polarizability is a measure for the interactions between the dipole moment and the electric field (Sihvola, 1999). Although, some materials have a permanent dipole moment even in the absence of an electric field, for example water molecules. Permittivity is a value, which characterizes the dielectric properties of a material, the larger the tendency for electric polarization, the larger the value of the permittivity.

Ice crystals are homogeneously composed of pure ice, whereas snowflakes are a mixture of ice and air, and in the melting process also water is included. Even though both ice and water are constructed from H_2O molecules, their permittivity is very different in microwave frequency region.

The real part of the relative dielectric permittivity of ice has almost a constant value of $\varepsilon_r' = 3.2$ over a frequency range from 10 MHz to 1 THz with slight temperature dependence (Mätzler and Wegmüller, 1987). Based on Mätzler and Wegmüller (1987) measurements over the frequency range from 2 to 100 GHz at two different temperatures (T=-5°C, -15°C), the real effective permittivity of ice can be described

$$\varepsilon_r' = 3.1884 + 0.00019T, \tag{4.35}$$

where T is the temperature in degrees Celsius.

The imaginary part of ε_r'' is small compared to the real part; it ranges between $10^{-4} - 10^{-2}$ at the microwave frequencies. It is influenced by the impurities, and as the wavelength increases, also the sensitivity on temperature grows (Warren, 1984). The imaginary part of permittivity is usually presented in the form

$$\varepsilon_r'' = (A/f) + Bf^C + Df^3 \tag{4.36}$$

where f is the frequency in GHz. The parameters A, B, C, and D are dependent on the temperature and the impurities (Mätzler and Wegmüller, 1987; Hufford, 1991; Mishima et al., 1983; Jiang and Wu, 2004). For example Mätzler and Wegmüller (1987) defined the terms from an empirical fit to data for pure ice $A = 6 \cdot 10^{-4}$, $B = 6.5 \cdot 10^{-5}$, $C = 1.07$ at T=-5°C, and $D = 0$.

The permittivity of water is usually determined according to Debye model (applicable below 100 GHz frequency domain, Liebe et al. (1991)) (Sihvola, 1999)

$$\varepsilon_w(f) = \varepsilon_\infty + \frac{\varepsilon_{st} - \varepsilon_\infty}{1 - j2\pi f\tau}, \tag{4.37}$$

where $\varepsilon_{st} = 190.0 - 0.375T$ is the low-frequency or static permittivity, $\varepsilon_\infty = 4.90$ is the high-frequency permittivity, $\tau = \frac{1.99}{T} e^{2140/T} \cdot 10^{-12}$s is the relaxation time. For higher frequencies, the Double Debye Model should be applied. The Debye model describes well the dielectric response of fluids with permanent electric dipole moments (Sihvola, 1999). At microwave frequencies ice is fairly dispersionless and lossless, whereas water is strongly dependent on the wavelength. For example the permittivity of water at

0°C with Eq.(4.37) at C-band is 63.0 + j37.8, at Ka - band 9.5 +j18.9 and at W-band 5.6+j7.5, respectively.

For an inhomogeneous particle, the dielectric properties are calculated as a weighted average of the properties of the components in the medium, considering e.g. shape, size, orientation and mutual relation of the different components. Thus the particle can be treated as homogeneous with effective permittivity. The method to compose the effective permittivity is known as **Effective Medium Approximation** (EMA) or utilizing mixing model rules. The drawback of EMA is that information of the particle structure is lost, and its effect e.g. to polarimetric quantities cannot be derived. The feasibility of EMAs is restricted to a frequency region, where the inhomogeneities are much smaller than the wavelength. There exists also so called extended EMAs (EEMA), which is constructed to allow a larger size of inclusions, but still smaller than the wavelength. As a rule of thumb, it is suggested in (Sihvola, 1999)

$$\frac{\lambda}{2\pi} > \delta, \tag{4.38}$$

where δ is a measure for the size of the inclusion (Yaghjian, 1980). At C-band, the utilization of mixing formulas is justified for describing snowflakes, but towards higher frequencies like at Ka- or W-bands, the assumptions used in the EMA may not be valid.

In a two-material mixture, the inclusion component is called a guest, and the environment is called the host or matrix material. Some EMAs can be expanded to include several components, but often the mixing is performed in stages; first two components are mixed according to a mixing rule, and then the third component is mixed with the resulting mixture and so forth.

Maxwell Garnett-model (MG) is a basic mixing rule for isotropic inclusions and environment medium. The MG model is asymmetric, and for the two-phase MG mixture, the method provides the upper and lower bounds of possible values of permittivity, whether the another component is the inclusion and the other forming environment matrix (Mishchenko et al., 2000).

For spherical inclusions, the MG rule can be derived from the static field solution presented later in Section 4.5.1 with the internal electric field stated as a function of an incident field for a sphere in Eq.(4.50) (Sihvola, 1999). Let the mixture consists of spherical inclusions of relative permittivity ε_{ic} in an environment with permittivity of ε_{mt} and the fraction f_V of the volume is occupied by the inclusions and $1 - f_V$ of the environment.

Then it can be written

$$\varepsilon_{eff} = \frac{(1 - f_V)\,\varepsilon_{mt} + f_V E_r \varepsilon_{ic}}{(1 - f_V) + f_V E_r}, \tag{4.39}$$

where E_r is the field ratio between the internal field and the external field. Inserting Eq.(4.50), the effective permittivity is

$$\varepsilon_{eff} = \varepsilon_{mt} + 3 f_V \varepsilon_{mt} \frac{\varepsilon_{ic} - \varepsilon_{mt}}{\varepsilon_{ic} + 2\varepsilon_{mt} - f_V\left(\varepsilon_{ic} - \varepsilon_{mt}\right)}, \tag{4.40}$$

which is the basic form of the MG mixing rule. However, with the basic MG rule, it is impossible to model $f_V = 1$, because the maximum packing efficiency with spheres is ≈ 0.63 (Bringi and Chandrasekar, 2001). A higher packing efficiency can be reached with different sizes of inclusions. Bohren and Battan (1982) derived, for randomly distributed and oriented ellipsoidal inclusions of different sizes, the form of MG is

$$\varepsilon_{eff} = \frac{(1 - f_V)\,\varepsilon_{mt} + f_V \beta \varepsilon_{ic}}{1 - f_V + f_V \beta}, \tag{4.41}$$

$$\beta = \frac{2\varepsilon_{mt}}{\varepsilon_{ic} - \varepsilon_{mt}} \left[\frac{\varepsilon_{ic}}{\varepsilon_{ic} - \varepsilon_{mt}} \ln(\varepsilon_{ic}/\varepsilon_{mt}) - 1 \right]. \tag{4.42}$$

In a similar expression for randomly orientated spheroids MG is presented in (de Wolf et al., 1990)

$$\varepsilon_{eff} = \varepsilon_{mt} \frac{1 + \frac{1}{3} f_V \left[\frac{\varepsilon_{ic}}{\varepsilon_{mt}} \left(\langle \Psi_1 \rangle + \langle \Psi_2 \rangle + \langle \Psi_3 \rangle \right) - 3 \right]}{1 + \frac{1}{3} f_V \left[\left(\langle \Psi_1 \rangle + \langle \Psi_2 \rangle + \langle \Psi_3 \rangle \right) - 3 \right]}, \tag{4.43}$$

with

$$\langle \Psi_1 \rangle = \langle \Psi_2 \rangle = \frac{2\varepsilon_{mt}}{(r_b - r_a)\left(\varepsilon_{ic} - \varepsilon_{mt}\right)} \ln \left[\frac{(\varepsilon_{ic} + \varepsilon_{mt}) - r_a\left(\varepsilon_{ic} - \varepsilon_{mt}\right)}{(\varepsilon_{ic} + \varepsilon_{mt}) - r_b\left(\varepsilon_{ic} - \varepsilon_{mt}\right)} \right] \tag{4.44}$$

$$\langle \Psi_3 \rangle = \frac{\varepsilon_{mt}}{(r_b - r_a)\left(\varepsilon_{ic} - \varepsilon_{mt}\right)} \ln \left[\frac{\varepsilon_{mt} - r_b\left(\varepsilon_{ic} - \varepsilon_{mt}\right)}{\varepsilon_{mt} - r_a\left(\varepsilon_{ic} - \varepsilon_{mt}\right)} \right] \tag{4.45}$$

Bruggeman method has no hierarchy difference between the host and the guest material. The effective permittivity according to Bruggeman method for spherical particles is (Sihvola, 1999)

$$\sum_{j=1}^{N} f_{V_j} \frac{\varepsilon_j - \varepsilon_{eff}}{\varepsilon_j + 2\varepsilon_{eff}} = 0, \tag{4.46}$$

where N is the number of different phases with permittivities ε_j each occupying a volume fraction of f_{V_j}.

The **Wiener mixing rule** used by Oguchi (1983) is

$$\frac{(\varepsilon_{eff} - 1)}{(\varepsilon_{eff} + u)} = \sum_{j=1}^{N} f_{V_j} \frac{(\varepsilon_j - 1)}{(\varepsilon_j + u)}, \tag{4.47}$$

where $\sum_{j=1}^{N} f_{V_j} = 1$ and u is a dimensionless form factor corresponding inclusion shape and for spherical particles, which are sparsely distributed in a vacuum, $u = 2$.

In (Meneghini and Liao, 2000) the effective permittivity is defined by computing the internal fields of the particle with volume integral equation method and then averaging the field amplitudes $\langle E_1 \rangle$ and $\langle E_2 \rangle$. The method is called Conjugate Gradient Fast Fourier Transform (CG-FFT), and it can be stated as

$$\varepsilon_{eff} = \frac{\varepsilon_1 f_{V_1} \langle E_1 \rangle / \langle E_2 \rangle + \varepsilon_2 f_{V_2}}{f_{V_1} \langle E_1 \rangle / \langle E_2 \rangle + f_{V_2}}. \tag{4.48}$$

The mutual relation of the inclusion and matrix component depends on the topology modeled for volume integral equation methods and a change of component shape from cubic to spherical had a relatively small effect on the resulting effective permittivity value (Meneghini and Liao, 2000).

For snow, where the permittivity difference between air and ice is small, the effective permittivity has very similar values with different EMAs. There is no general conclusion, which would prefer one mixing rule over another. Also, if MG is applied, the retrieved effective permittivity is almost independent of the selection of matrix and inclusion media. However given that the permittivity of water is high in the microwave region, with the melting hydrometeors the discrepancy of component permittivities is large. Changing the order of the mixed components to another or utilizing different mixing rules, can lead to notably different effective permittivity values and therefore to different scattering response (Fabry and Szyrmer, 1999). This is discussed in Section 5.2.

4.4 Size parameter and scattering regimes

The **size parameter** is a dimensionless parameter to describe the particle size relative to the radiation wavelength

$$x = \frac{\pi D}{\lambda}, \tag{4.49}$$

where D is a characteristic diameter of the particle. The different scattering modes and methods to solve the scattering problem are typically divided into three domains according to size parameter:

- **Rayleigh scattering regime** ($x \ll 1$), where the particle size is much smaller than the wavelength, typically the upper limit is determined *ad*

hoc as $1/10$ of the wavelength. In this region, it can be approximated that the incident field $\bar{E}^{inc}$ impinging on the particle is constant and the internal field can be calculated from the knowledge of the static field solution. The scattering is strongly dependent on size of the particle $\sim D^6$, and there is no angular dependence.

- **Resonance regime** ($x \approx 1$), where the particle has approximately the same size as the wavelength. In this regime, the shape and the inhomogeneities of the particle are significantly influencing the complex scattering pattern. The closed-form solution exists only for spheres. For arbitrary shaped particles, numerical methods are used to determine the scattered field, and these are usually computationally costly.

- **Physical optics regime** ($x \gg 1$), where the particles are much larger than the wavelength. In this regime, the laws of geometric optics,i.e. reflection, refraction, and diffraction, are generally sufficient to describe the interaction of electromagnetic wave with the particle. The ray tracing is one of the computational techniques used in this regime.

4.5 Scattering methods

The scattering problem is stated in Eq.(4.20). The internal electric field $\bar{E}^{\text{int}}$ inside the particle induced by the total electric field $\bar{E}^{\text{tot}}$ is generally unknown, because of this, some kind of approximation is applied instead. Here some of the well-known methods for retrieving the scattering properties are briefly presented, more extensive descriptions can be found for example from (Tsang et al., 2000; Tsang and Kong, 2001; Mishchenko et al., 2000; Kahnert, 2003).

4.5.1 Rayleigh scattering

For a particle much smaller than the wavelength, the spatial and temporal variance of the incident field can be neglected, and the instantaneous internal electric field inside the scatterer can be obtained from a static solution. This is called the Rayleigh approximation. For a small spherical particle centered at origin, the internal field is (Tsang et al., 2000)

$$\bar{E}^{\text{int}} = \frac{3}{\varepsilon_r + 2}\bar{E}^{\text{inc}}. \tag{4.50}$$

Then the scattered field can be obtained from Eq.(4.20), where the volume of the particle is $V = \pi/6D^3$ and ε_r is a constant value

$$\bar{E}^s = -\frac{k_0^2}{4\pi}\frac{e^{-jk_0R}}{R}\int\limits_V (\varepsilon_r - 1)\,\frac{3}{\varepsilon_r + 2}\bar{k}_s \times \left(\bar{k}_s \times \bar{E}^{inc}\right) e^{-jk_0\bar{k}_s\cdot\bar{r}'}dV'. \quad (4.51)$$

From Eq.(4.21) follows that the scattering amplitude is

$$f(\bar{k}_s, \bar{k}_i) = \frac{k_0^2}{4\pi}\frac{3\,(\varepsilon_r - 1)}{\varepsilon_r + 2}V\left(-\bar{k}_s \times \left(\bar{k}_s \times \bar{e}_i\right)\right). \quad (4.52)$$

For vertical and horizontal polarizations the scattering amplitude matrix can be written as a function of incident and scattered angles θ_i, ϕ_i and θ_s, ϕ_s in the scattering plane coordinate system (Tsang et al., 2000)

$$\begin{bmatrix} E_h^s \\ E_v^s \end{bmatrix} = \frac{e^{-jk_0R}}{4\pi R}\frac{3k_0^2\,(\varepsilon_r - 1)}{\varepsilon_r + 2}V \quad (4.53)$$
$$\begin{bmatrix} -\cos(\phi_s - \phi_i) & -cos\theta_i sin(\phi_s - \phi_i) \\ \cos\theta_s \sin(\theta_s - \theta_i) & \cos\theta_s \cos\theta_i \cos(\phi_s - \phi_i) + \sin\theta_s \sin\theta_i \end{bmatrix}$$
$$\begin{bmatrix} E_h^{inc} \\ E_v^{inc} \end{bmatrix}.$$

If the incident wave propagate along z-axis ($\bar{k}_s = \bar{r}$, $\theta_i = \phi_i = 0$) and scatteres in the backscattering direction ($\bar{k}_s = -\bar{k}_i$, $\theta_s = \pi, \phi_s = \pi$), the scattering amplitude is

$$\begin{bmatrix} E_h^s \\ E_v^s \end{bmatrix} = k_0^2\frac{e^{-jk_0R}}{4\pi R}\frac{3\,(\varepsilon_r - 1)}{\varepsilon_r + 2}V\begin{bmatrix} 1 & 0 \\ 0 & 1 \end{bmatrix}\begin{bmatrix} E_h^{inc} \\ E_v^{inc} \end{bmatrix}. \quad (4.54)$$

Considering the scattering cross-section for the backscattering direction from Eq.(4.27) for a co-polarized wave and inserting the volume of sphere, it will be

$$\sigma_b(-\bar{k}_i, \bar{k}_i) = 4\pi\left|f(-\bar{k}_i, \bar{k}_i)\right|^2 = 4\pi\left|\frac{3k_0^2}{4\pi}\frac{\pi D^3}{6}\frac{(\varepsilon_r - 1)}{(\varepsilon_r + 2)}\right|^2 = \frac{\pi^5}{\lambda^4}\left|K\right|^2 D^6, \quad (4.55)$$

when wave number is $k_0 = 2\pi/\lambda$ and the dielectric factor $|K|^2 = \left|\frac{(\varepsilon_r - 1)}{(\varepsilon_r + 2)}\right|^2$. For a spheroid, the polarizability matrix should take into account the shape effects (Bringi and Chandrasekar, 2001). Typically Rayleigh scattering is considered to be applicable to weather radar observations ($f < 10$ GHz (X-band)).

4.5.2 Lorenz-Mie theory

When the size of the scatterer is comparable with the wavelength, the Rayleigh approximation does not apply. The most common solution to the

scattering problem is an analytical solution for spherical particles based on separation of variables SVM method, known as the Mie solution or Lorenz-Mie theory (Mie, 1908; Lorenz, 1890). In Mie solution, the incident, scattered, and internal fields are expanded in vector spherical harmonics. The field functions become linear combinations of terms that are products of separable functions of the three spherical coordinates: spherical Bessel functions of the distance from the sphere, associated Legendre polynomials of the zenith angle and sinusoidal functions of the azimuth angle (Sihvola, 1999). The unknown coefficients in these series are defined by the boundary conditions at the surface of the sphere; the tangential field components of the total fields have to be continuous across the particle surface, and the tangential components of the electric and magnetic fields have to approach zero as the distance from the origin approaches infinity (Kahnert, 2003). The scattered field is according to (Fung, 1994)

$$\begin{aligned} \bar{E}^s &= E^{inc} \sum_{n=1}^{\infty} j^n \frac{(2n+1)}{n\,(n+1)} \left\{ -b_n \bar{m}_{o1n}^{(3)} + j a_n \bar{n}_{e1n}^{(3)} \right\} \\ \bar{H}^s &= \frac{E^{inc}}{\eta} \sum_{n=1}^{\infty} j^n \frac{(2n+1)}{n\,(n+1)} \left\{ a_n \bar{m}_{e1n}^{(3)} + j b_n \bar{n}_{o1n}^{(3)} \right\}, \end{aligned} \tag{4.56}$$

where a_n and b_n are the Mie coefficients. The parameters $\bar{m}$ and $\bar{n}$ are spherical vector wave functions, where o and e denote odd and even cases corresponding the sinusoidal functions of the azimuth angle. The subscript n corresponds to the number of terms calculated for the $\sin$-function and m for the $\cos$-function, here $m = 1$. In addition, the vector wave functions are expressed in terms of spherical Hankel functions of the first kind $h_n^{(1)}(kr)$ (or also called as spherical Bessel functions of the third kind, thus the superscript $^{(3)}$) and the associated Legendre function of the first kind $P_n^{(1)}(\cos\theta)$ (Fung, 1994; Bohren and Huffman, 1983)

$$\begin{aligned} \bar{m}_{\substack{o \\ e}\,\ln}^{(3)} &= \pm \frac{\bar{\theta}}{\sin\theta} h_n^{(1)}(k_0 r)\, P_n^{(1)}(\cos\theta) \begin{bmatrix} \cos \\ \sin \end{bmatrix} (\phi) \\ &- \bar{\phi} h_n^{(1)}(k_0 r) \frac{\partial P_n^{(1)}(\cos\theta)}{\partial\theta} \begin{bmatrix} \sin \\ \cos \end{bmatrix} (\phi) \\ \bar{n}_{\substack{o \\ e}\,\ln}^{(3)} &= \pm \bar{r} \frac{n\,(n+1)}{k_0 r} h_n^{(1)}(k_0 r)\, P_n^{(1)}(\cos\theta) \begin{bmatrix} \sin \\ \cos \end{bmatrix} (\phi) \\ &+ \frac{\bar{\theta}}{k_0 r} \left[k_0 r h_n^{(1)}(k_0 r) \right] \frac{\partial P_n^{(1)}(\cos\theta)}{\partial\theta} \begin{bmatrix} \sin \\ \cos \end{bmatrix} (\phi) \\ &\pm \frac{\bar{\phi}}{k_0 r \sin\theta} \frac{\partial \left[k_0 r h_n^{(1)}(k_0 r) \right]}{\partial r} P_n^{(1)}(\cos\theta) \begin{bmatrix} \sin \\ \cos \end{bmatrix} (\phi), \end{aligned} \tag{4.57}$$

in which r is the range and $\bar{r}, \bar{\theta}, \bar{\phi}$ are the unit vectors. The Mie coefficients are given by (Bohren and Huffman, 1983)

$$\begin{aligned} a_n &= \frac{\sqrt{\varepsilon_r} j_n\left(\sqrt{\varepsilon_r} x\right)\left[x j_n(x)\right]' - j_n(x)\left[\left(\sqrt{\varepsilon_r} x\right) j_n \sqrt{\varepsilon_r}(x)\right]'}{\sqrt{\varepsilon_r} j_n\left(\sqrt{\varepsilon_r} x\right)\left[x h_n^{(1)}(x)\right]' - h_n^{(1)}(x)\left[\sqrt{\varepsilon_r} j_n \sqrt{\varepsilon_r}(x)\right]'} \\ b_n &= \frac{j_n\left(\sqrt{\varepsilon_r} x\right)\left[x j_n(x)\right]' - j_n(x)\left[\left(\sqrt{\varepsilon_r} x\right) j_n \sqrt{\varepsilon_r}(x)\right]'}{j_n\left(\sqrt{\varepsilon_r} x\right)\left[x h_n^{(1)}(x)\right]' - h_n^{(1)}(x)\left[\sqrt{\varepsilon_r} j_n \sqrt{\varepsilon_r}(x)\right]'}, \end{aligned} \tag{4.58}$$

where $j_n()$ is the spherical Bessel function of the first kind and $[]'$ denotes differentiation with respect to the argument. As a result, the scattered field is a convergent infinite sum of the partial waves. The number of terms N that needs to be calculated for an enough accurate estimate of the scattered field, is often defined according to (Wiscombe, 1980)

$$N = \begin{cases} x + 4\sqrt[3]{x} + 1 & 0.02 \leq x \leq 8 \\ x + 4.05\sqrt[3]{x} + 2 & 8 < x < 4200 \\ x + 4\sqrt[3]{x} + 2 & 4200 \leq x \leq 20000, \end{cases} \tag{4.59}$$

in which x is the size parameter.

The Mie solution or more generally the SVM is a precise method, and it is often used as a benchmark for computational scattering methods. The analytic solution is limited to spheres, though SVM can be applied also to any other coordinate system in which the scalar Helmholtz equation becomes separable, i.e. in the spheroidal coordinates the spherical vector wave functions are replaced with spheroidal vector wave functions, but in this case the solution can not be achieved analytically (Kahnert, 2003). The popularity of the Mie solution is partly explained by the well-documented computer algorithms (Wiscombe, 1980; Bohren and Huffman, 1983). Hence many scattering problems are treated by computing also non-spherical particles with Mie solution replacing the scatterers as equivalent-volume spheres and the effect of non-sphericity is discarded (Mishchenko et al., 2000). One drawback of SVM is that it can only be used for homogeneous particles, and for inhomogeneous particles it is commonly utilized with EMA (Section 4.3). Inhomogeneity can also be addressed with a solution for concentric layered spheres (Aden and Kerker, 1951). Melting particles are often modeled with two-layered spheres, where the inner core is ice or mixture of ice and air, and the upper cover is water. Botta et al. (2010) applied Generalized Multiparticle Mie (GMM) method for defining the scattering from dry and melting aggregates. In GMM the particle is constructed from a set of non-overlapping spheres with arbitrary position

and size, and the scattering solution is reached by taking into account the interaction fields between each sphere.

4.5.3 Rayleigh-Gans Approximation

Assuming the relative permittivity ε_r of the scattering particle to be close to the permittivity of the surrounding medium, and thus the higher-order interactions of the electromagnetic radiation within the particle can be ignored. In this case, the internal electric field is estimated to be same as the incident field

$$\bar{E}^{\text{int}} \approx \bar{E}^{\text{inc}}. \tag{4.60}$$

This is known as Born or Rayleigh-Gans approximation (RGA) (Bohren and Huffman, 1983; Tsang et al., 2000), where the scattered wave of a particle can be directly constructed as a superposition of the scattered waves originating from different parts of the particle. Inserting the Eq.(4.60) to scattering equation Eq.(4.20) with incident field plane wave described as Eq.(4.21) with $E_0 = 1$ (Tsang et al., 2000)

$$\bar{E}^s = -\frac{k_0^2}{4\pi}\frac{e^{-jk_0R}}{R}\int_{-\infty}^{\infty}\int\left(\varepsilon_r\left(\bar{r}'\right)-1\right)\bar{k}_s\times\left(\bar{k}_s\times\bar{e}_i\right)e^{-jk_0\bar{k}_d\cdot\bar{r}'}dx'dy'dz'. \tag{4.61}$$

The integration limits can be expanded now to infinity as the outside the particle the relative permittivity is 1, and the integrand is zero. Let $\bar{k}_d = \bar{k}_i - \bar{k}_s$ and polarization of the scattered field $\bar{k}_s \times \bar{k}_s \times \bar{e}_i$ depends only on scattered direction and incident polarization. It can be seen that the scattering amplitude matrix is a scalar integration over the particle volume and can be stated as

$$f(\bar{k}_s,\bar{k}_i) = -\frac{k_0^2}{4\pi}\left(-\bar{k}_s\times\left(\bar{k}_s\times\bar{e}_i\right)\right)\int_{-\infty}^{\infty}\int\left(\varepsilon_r\left(\bar{r}'\right)-1\right)e^{-jk_0\bar{k}_d\cdot\bar{r}'}dx'dy'dz' \tag{4.62}$$

where the form factor is

$$S(\bar{k}_s,\bar{k}_i) = \frac{1}{V}\int_{-\infty}^{\infty}\int\left(\varepsilon_r\left(\bar{r}'\right)-1\right)e^{-jk_0\bar{k}_d\cdot\bar{r}'}dx'dy'dz'. \tag{4.63}$$

In comparison to Rayleigh scattering, in RGA there is no assumption of a small particle relative to the wavelength, and applicability of RGA in the frequency range is wider (Matrosov, 1992). The requirement of the small difference in relative permittivity to surrounding must be filled, and additionally, the maximum phase shift of the incident wave through the

particle should be small (Bohren and Huffman, 1983)

$$\begin{cases} \left|\sqrt{\varepsilon_r} - 1\right| \ll 1 \\ x\left|\sqrt{\varepsilon_r} - 1\right| \ll 1. \end{cases} \tag{4.64}$$

Based on studies of fractal aggregates in (Berry and Percival, 1986), it is speculated that in an open structure, the first requirement can be relaxed for fluffy aggregates because of the large air gaps between the solid parts of the particle (Westbrook et al., 2006; Tyynelä et al., 2013). RGA is computationally faster than e.g. Discrete Dipole Approximation (DDA, in Section 4.5.5). When compared to DDA as shown in (Tyynelä et al., 2013), RGA provides more accurate backscattering for irregular snowflakes than can be obtained with Mie solution or Rayleigh approximation at higher frequencies. Given the mathematically simple solution, utilizing RGA offers a possibility to investigate the influence of the particle structure on the modeled scattering (Westbrook et al., 2006; Leinonen et al., 2013; Hogan and Westbrook, 2014). Westbrook et al. (2006) described snowflakes with a single universal function, where the form factor depends only on the overall shape of the aggregate and not on the details of the monomer crystals composing the snowflake. One of the shortcomings is that in its basic form, RGA cannot model the polarimetric radar observables. Lu et al. (2013) presented a modification to RGA adding the self-interactions between different parts of an ice crystal. Compared to GMM calculations this version improves the accuracy of the method and extends its applicability to polarization-dependent parameters, however, is it limited to single crystals at millimeter or longer wavelengths or low-density aggregates (Lu et al., 2014). Hogan and Westbrook (2014) presented parametrization of two modeled snowflake structures with five terms. The backscattering cross-sections of the ensemble of snowflakes can be retrieved with this parametrization, and because in this method the complex snowflake structures can be described with the fractal structure, it is called Self-Similar Rayleigh-Gans (SSRGA). The full scattering phase function can be obtained with SSRGA, and as compared with DDA calculations at 94 and 183 GHz, the earlier noticed underestimation in backscatter is reduced (Hogan et al., 2017). For dense particles resulting from riming, SSRGA is limited, and Hogan et al. (2017) reported that the backscattering cross-sections can be underestimated by a factor of 2.

4.5.4 T-matrix method

For non-spherical particles, T-matrix method (TMM) is widely used and is a computationally efficient technique. The TMM was originally introduced by Waterman (1965, 1971) for computing electromagnetic scattering of a single homogeneous particle by utilizing boundary conditions with the surface-integral equation form of the scattering problem in Eq.(4.15), but the comprehensive development work of Mishchenko *et al.* and providing public-domain Fortran T-matrix codes have increased the popularity of the method (Mishchenko and Travis, 2017). The formulation of T-matrix can be derived from many scattering methods i.e. either from the Null-Field Method (Kahnert, 2003) or by reformulating SVM (Schulz et al., 1998), and actually for spheres TMM formulation is equal to the standard Lorenz-Mie theory (Mishchenko et al., 2000). Similar to Mie solution, the incident, internal, and scattered field can be expanded to the regular vector wave functions and substituted into the scattering surface-integral equation. The surface integral over the boundary surface can be evaluated by numerical surface integration and the T-matrix is computed from the coefficient elements. The exact equations can be found e.g. (Tsang et al., 2000; Mishchenko et al., 2000; Kahnert, 2003).

The T-matrix contains the full information of particle scattering properties by connecting the derived expansion coefficients matrix of the scattered field $\mathbf{p}$ in terms of those of the incident field $\mathbf{a}$ (Kahnert, 2003)

$$\mathbf{p} = \mathbf{T}\mathbf{a}. \tag{4.65}$$

After the T-matrix is calculated, the major advantage of the method is that in comparison e.g. to DDA, the elements of T-matrix are independent of the incident and the scattered fields, and thus the T-matrix can be computed only once and then used for any incident or scattering directions. The T-matrix is dependent on the shape, size parameter, and permittivity of the scattering particle and on its orientation with respect to reference frame. The T-matrix formalism can be applied to any particle shape, but without rotational symmetry, the computational complexity is greater and the calculation time increases significantly (Mishchenko et al., 2000). Thus, TMM is typically applied to spheroids or rotationally symmetric particles. The disadvantage of the basic TMM in describing hydrometeors is that the method is only applicable to homogeneous particles and, even though with T-matrix the nonspherical particles can be modeled, the internal inhomogeneity cannot be directly considered.

TMM has been applied for describing snowflakes e.g. (Matrosov, 2007; Leinonen et al., 2011) and comparisons to more rigorous methods such as DDA are presented in (Tyynelä et al., 2011; Leinonen et al., 2012a). In the modeling of melting layer, TMM is utilized in (Matrosov, 2008) for spheroidal particles for defining the attenuation in the melting layer at X and Ka-band and in (Skaropoulos and Russchenberg, 2002) for S-band examining the Doppler spectrum in the melting layer.

4.5.5 Discrete Dipole Approximation

In the recent studies of the scattering properties of snowflakes, the emphasis is on more realistic modeling of the particles, and thus on deriving the scattering characteristics caused by the complexity of particle structure. In this respect the Lorenz-Mie solution or T-matrix method are limited, they can be exploited effectively only for spheres or spheroidal particles, and homogeneous particles. The ability to compute scattering of the non-spherical particles and to understand the effect of inner structure requires another kind of approach. The increasing computational power has created interest for numerical techniques, and their utilization is actively researched.

Volume integral equation methods are one of the numerical techniques, where the electromagnetic scattering problem can be solved for non-spherical particles. They are flexible techniques, which can be applied to arbitrary, inhomogeneous and anisotropic particles. In these methods, the scattering particle is divided into finite volume elements, and assuming that these elements are much smaller than the wavelength; the variation of permittivity and electric field inside the element are insignificant. Therefore, each element is considered homogeneous, both permittivity and electric field being constants inside, and the scattering properties of a single element can be defined. Modeling the particle will then lead to a system of linear equations that can be inverted numerically by standard techniques (Yurkin et al., 2007). Besides the requirements of static solution inside the elements, another restriction on the element size is their capability to provide an accurate enough representation of the scattering particle. Both of these requirements yield a great number of elements, and often the required calculations set high demands on CPU resources. For a scatterer with high relative permittivity, the needed amount of elements even increases. In general, the way to improve the accuracy of volume integral equation methods is to increase the number of elements (Kahnert, 2003) or by also considering the magnetic field description in addition to

the electric field (Mulholland et al., 1994; Merchiers et al., 2007). Both are resulting an increase in computations. Therefore, the usability of volume integral equation methods depends greatly on the choice of the computational method in solving this vast amount of equations. Another disadvantage of the methods is the need to repeat the calculations for each new incident angle.

Under the title of volume integral equation methods, several different approaches or techniques are presented in literature, Discrete Dipole Approximation (DDA) being the most popular one. Distinguishing one from other similar methods is not always so straightforward. For example, Digitized Green's Function (DGF) method (Goedecke and O'Brien, 1988) and Volume Integral Equation Formulation (VIEF) (Hage et al., 1991) were derived separately from DDA, but in fact, mathematically they are close to each other (Draine and Goodman, 1993; Lakhtakia and Mulholland, 1993; Kahnert, 2003; Yurkin et al., 2007). The DDA is also referred as the coupled dipole method (CDM) (Lakhtakia and Mulholland, 1993).

DDA is far more utilized and known than the other methods, thanks to the work by Draine and his co-workers, e.g. (Draine, 1988; Draine and Flatau, 1994, 2008), who are the pioneers in DDA modeling. In addition to publications, they have provided a free program (DDSCAT 7.3, 2017), which many scientists have used in their calculations, for snow particles e.g. (Foster et al., 1999, 2000; Evans and Stephens, 1995a,b). DDA was introduced already in 1964 in studying the optical properties of molecular aggregates by de Voe (1964, 1965) and after the research of Purcell and Pennypacker (1973), DDA became extensively applicable. Following DDSCAT also other free available DDA codes appeared later e.g. ADDA (2017) by Yurkin and Hoekstra (2007) and JSCAT (2017) by Peltoniemi (1996). A comparison of four different implementations of DDA, like ADDA and DDSCAT, is presented in (Penttilä et al., 2007) and comparisons to other methods are discussed in (Lakhtakia and Mulholland, 1993; Kahnert, 2003; Tsang et al., 2001; Mishchenko et al., 2002). There also exit extensive review articles of the method, e.g. by Draine and Flatau (1994); Yurkin et al. (2007).

The scattered field in DDA can be determined from the Eq.(4.18) by discretization of the particle into N small volume cells (ΔV_n), which are represented by dipoles. It is assumed that the incident field, the induced current and permittivity are uniform inside these small volumes. The excited field for each dipole consists of the incident field and the contributions

from all other cells $n \neq k$, $k = 1, ...N$,

$$\bar{E}^s(\bar{r}) \approx -j\omega\mu \sum_{n=1}^{N} \int_{\Delta V_n} \bar{\bar{G}}(\bar{r}, \bar{r}') J_n(\bar{r}') \, dV'. \tag{4.66}$$

The volume-current density is given by Eq.(4.14), and the dipole moment is related to $\bar{J}$ for the dipole $n = k$

$$\begin{aligned} \bar{p}_k &= -\frac{j}{\omega} V_k \bar{J}_k \\ &= \alpha_k \bar{E}_k^{inc}, \end{aligned} \tag{4.67}$$

where polarizability α_k is the linear relation of the dipole moment $\bar{p}_k$ and the external incident field $\bar{E}_k^{inc}$. The system matrix is defined following (Kahnert, 2003)

$$\bar{E}_k^s \approx -\omega^2 \mu_0 \sum_{n\neq 1, n\neq k}^{N} \bar{\bar{G}}_{kn} \alpha_n \bar{E}_n^{inc}. \tag{4.68}$$

The accuracy of DDA calculations depend directly on the polarizability α_n of the point dipoles. In the literature, there are several derivations to improve formulation of the α_n (Yurkin et al., 2007). Another requirement for accurate results is the needed amount of dipoles. Even though DDA is flexible regarding the geometry of the target, there is a limitation on the inter-dipole separation d. It must be small compared to (1) any structural lengths of the target, and (2) the wavelength λ. Numerical studies with DDSCAT indicate that the second criterion is adequately satisfied if

$$|\sqrt{\varepsilon_r}| \, kd < 1, \tag{4.69}$$

this criterion is valid, if $\left|\sqrt{\varepsilon_r} - 1\right| \leq 3$. If $(\sqrt{\varepsilon_r})$ is large, the used inter-dipole distances should decrease and fullfill the criterion

$$|\sqrt{\varepsilon_r}| \, kd < 0.5. \tag{4.70}$$

Therefore the primary application of DDA is for scattering computations of dielectric targets with sizes comparable to the wavelength, and the method is not suitable for larger values of the size parameters or the permittivity. The error in DDA calculations increases by abrupt permittivity changes between neighboring dipoles. For example, a thin coating of water on an otherwise dry snowflake produces relative errors in backscatter cross-sections in the order of 25% due to the high permittivity value of water in respect of ice in microwave frequencies (Tyynelä et al., 2009). DDA has been applied to modeling of the scattering from snowflakes as spheroids e.g. (Tyynelä et al., 2009) and more realistic snowflake models e.g. (Liu,

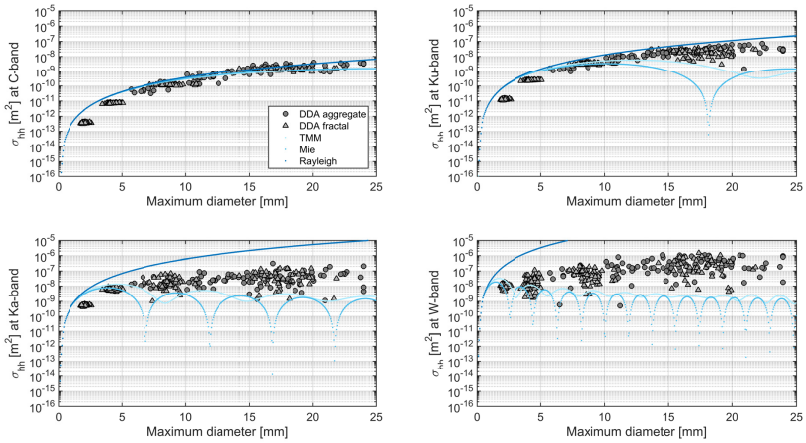

Figure 4.2. The horizontal backscattering cross-sections as a function of maximum diameter with different scattering methods at C-, Ku-, Ka- and W-bands are shown. The DDA and TMM scattering calculations are from (Tyynelä et al., 2011). The complex aggregates are marked as dark gray circles and fractals as lighter gray triangles, and scattering calculations are performed with ADDA. The spheroids (light blue dots) have an aspect ratio of 0.65, density is following the used $m(D)$ relations of the aggregates, and corresponding relative permittivity is calculated using Maxwell-Garnett effective medium approximation EMA with ice inclusions in air matrix. The scattering calculations are performed with TMM with Gaussian-distributed preferred orientation. The Lorentz-Mie solution (blue dots) and Rayleigh scattering (dark blue dots) are calculated with equi-volume spheres, and they have the same EMA as the corresponding spheroid.

2004; Kim, 2006; Liu, 2008; Tyynelä et al., 2011; Petty and Huang, 2010; Tyynelä et al., 2013; Nowell et al., 2013; Hogan et al., 2017) and melting snowflakes e.g. (Tyynelä et al., 2014; Ori et al., 2014). Other numerical models used for complex-shaped snowflakes are e.g. Finite-Difference-Time-Domain (FDTD) in (Aydin and Walsh, 1999) providing backscattering coefficients for single crystals at 35, 94, and 220 GHz frequencies and in (Ishimoto, 2008), for aggregates using a fractal approach at 9.8, 35, and 95 GHz.

4.5.6 Applicability of scattering methods in snowflake modeling

In remote sensing, snow particles are often modeled as spheres or spheroids, and the scattering properties are computed using Rayleigh approximation, Lorentz-Mie theory or TMM. The effective permittivity is derived by applying an EMA for air and ice mixture. These approaches for linking particle physical and scattering properties are called "soft-sphere" or "soft-spheroid" models. Another way is to construct more detailed shape model of the irregular snow particle, and compute the scattering properties

using numerical methods such as DDA or with RGA and GMM. There are two different approaches to create the detailed particle shape models and define their physical properties; physical-based and empirical-based methods (Tyynelä, 2017). In the physical-based method, the particle is formed by mimicking the growth processes, e.g., in (Westbrook, 2004; Tyynelä et al., 2011; Leinonen and Moisseev, 2015; Kuo et al., 2016) and in empirical-based method the physical properties of particles are determined by fitting to the measured quantities such as $m(D)$ relation, e.g. (Botta et al., 2011; Lu et al., 2016). The benefit of the empirical-based method is that the properties of the modeled particles are physical, but the drawback is that they are case-dependent and may not be representative with other measurements (Tyynelä, 2017).

The performance of different snowflake models at C-, Ku, Ka- and W-bands is illustrated in Figure 4.2 based on calculations by Tyynelä et al. (2011). It can be seen that all methods are showing similar backscattering cross-sections for this particle size range at C-band and utilization of the Rayleigh scattering approximation for spheres is not introducing a significant overestimation to the scattering computations at lower frequencies. Therefore, it is a reasonable assumption in Publication IV and Publication V to apply Rayleigh approximation for scattering calculations of snow particles when compared to C-band weather radar observations. For particles with higher permittivities, for example in melting, or at higher frequencies, the differences between the models increase, and more complex particle models and scattering methods should be applied. In Publication I, where melting snow particles were modeled at C-band, Lorenz-Mie theory was selected because of its simplicity and fast computational performance.

Publication II considers the scattering observations at higher frequencies. In general, Rayleigh approximation is strongly overestimating the backscattering cross-sections, whereas Mie-Lorentz theory seems to underestimate the backscattering compared to DDA computations. Leinonen et al. (2012a) demonstrated with observations at Ku, Ka, and W- bands that modeling with spheroids (TMM), the observed backscattering measurements cannot be explained consistently throughout the studied frequency range. Similar results were shown by (Petty and Huang, 2010; Botta et al., 2011). Tyynelä et al. (2011) concluded that backscattering cross-sections, calculated with ADDA for complex snowflakes and with T-matrix for corresponding soft spheroids, compare well at C-band and Ku-band, but spheroids are underestimating at higher frequencies by a factor

of 10 (Ka) and 50-100 (W) consistently with different sizes and shapes. One of the reasons for the observed limitations of the spheroid models can origin from applicability of EMA in the higher frequency range.

At present, it is understood that soft spheroid models are too simplistic and may not present consistent results especially at higher frequencies. The detailed and "realistic" particle models and DDA computations seem to be applicable at all frequency ranges. However, there is a question whether these "realistic" particle models are actually representative of snowflakes observed in nature. Because of the above-said, this topic is of current interest, and the applicability of the various particle models and scattering methods ranging over the microwave region is actively studied. Over the past decade, scientists have created databases of snow particle scattering properties at microwave frequencies and made them publicly available (Liu, 2008; Botta et al., 2011; Nowell et al., 2013; Tyynelä et al., 2014; Kuo et al., 2016; Lu et al., 2016). Databases contain polarimetric and non-polarimetric scattering properties of various types of modeled particles calculated with the different methods.

5. Microwave remote sensing observations

"What's a few dB among friends."

Cartoon in R.E. Reinhart: Radar for Meteorologists, 2004

The microwave remote sensing measurements can be divided into two categories according to the measurement principle, these are the active and passive techniques. In the active remote sensing, the instrument (radar or in the optical region working lidar) transmits electromagnetic wave to target and measures the backscattered wave and the elapsed time from the transmission to the return of the wave. Whereas in passive remote sensing, the radiometer observes electromagnetic radiation caused by thermal radiation of a target.

In the case of radars, the used wavelength is selected as a tradeoff between the measurement sensitivity, atmospheric attenuation and system design limitations. For precipitating-sized particles on the centimeter scale, the highest backscattering response is gained with centimeter-wavelength radar, while the attenuation of the atmosphere gases and constitutes is still small. Weather radars typically are operating at S (3 GHz)-, C (5.6 GHz)- or X (10.3 GHz) - bands with wavelengths between 10-3 cm. With shorter wavelengths, the radar is more sensitive for detecting smaller cloud particles (from 5 to 10 μm), although also attenuation increases with increasing frequency. The cloud radars are mainly operating at Ka- and W-bands. In Publication I, Publication IV and Publication V the C-band radar observations are analyzed and in Publication II the triple-frequency observations (X, Ka, and W) are investigated with surface measurements.

In general, the remote sensing retrievals with radiometer measurements are based on observations in different frequency channels and polariza-

tions, and often the targets of interest have a non-unique response at a given frequency. The radiometer measurements applied in this study are used to retrieve liquid water path (LWP) aloft utilizing the frequency channels of 23.8 GHz and 31.4 GHz in Publication II and Publication IV. Also, space-based estimates of snowfall are validated in Publication V. The estimate is retrieved from observations of GPM Microwave Imager (GMI)-instrument operating in thirteen microwave channels ranging from 10 GHz to 183 GHz.

5.1 Weather radars

The modern weather radars are typically dual-polarization Doppler pulse radars. A pulse radar transmits a short high-power pulse directed with an antenna to the observed target. The length of the pulse τ is in the order of microseconds. The pulse propagates with the speed of light, hits the object, which re-radiates part of the energy and part of this will be received at the radar. The received power is only a small fraction of the transmitted pulse. The receiver measures the power of backscattered pulse and the elapsed time of the traveled pulse to and from the object with a distance of R ($t = \frac{2R}{c}$). From the former, the amount and type of scatterers can be retrieved, and from the latter, the distance to the object can be obtained. Doppler radars retrieve the radial velocity of a moving object from the observed frequency shift in the returned pulse signal. Thus, Doppler weather radars can detect not only the intensity of precipitation but also track the storm movements and measure tracers of the wind and their radial velocities (Doviak and Zrnić, 1993). The Doppler radars can also effectively filter stationary clutter targets.

Weather radar is an ideal instrument to measure areal precipitation, because of the high temporal and spatial resolution of the observations. The physical characteristics of precipitation necessitate frequent measurements over a large range of scales (Kidd and Huffman, 2011), and the typical measurement resolution of minutes and hundreds of meters of an operational weather radar is superior in comparison, e.g., to a network of precipitation gauges. In Publication IV and Publication V the challenges of the conversion between the power measured by the radar and the precipitation rate are discussed. In addition to the uncertainties related to the retrievals, errors in weather radar measurements are generally related to hardware problems and miss-calibration (Joe and Smith, 2001), detec-

tion of clutter and false-echoes (Battan, 1973; Koistinen and Michelson, 2002), anomalous propagation (Doviak and Zrnić, 1993) and attenuation caused by heavy precipitation (Bringi and Chandrasekar, 2001) and wet radome (Kurri and Huuskonen, 2008; Frasier et al., 2013). Because of the vertical structure of precipitation, with increasing distance from the radar, scanning geometry introduces uncertainties in the radar-based precipitation estimates (Koistinen and Pohjola, 2014). Due to beam broadening, the sampling volume can contain precipitation in different phases or volume is only partly filled with precipitation. Also, at longer distances when the radar beam is located at higher altitudes, the correspondence of the measurement to precipitation on the ground is weaker, e.g., radar might measure an overhanging precipitation or overshoot a low precipitation system (Saltikoff et al., 2015).

Nowadays weather radars utilize usually dual-polarization by transmitting horizontally and vertically polarized electromagnetic waves and receiving polarized backscattered signals. Given that the hydrometeors are not spherical, their scattering characteristics are not the same for different polarizations. By comparing the signal properties in two perpendicular directions, more detailed information can be obtained about the particle sizes, shapes, phase, orientation, and particle size distributions. Dual-polarization measurements lead to improved rainfall estimation, attenuation correction, hydrometeor classification and overall data quality (Bringi and Chandrasekar, 2001).

5.1.1 Radar equation

The amount of energy received at the receiver antenna is (Rinehart, 1997)

$$P_r = \frac{P_t G_t}{4\pi R^2} \frac{\sigma_b}{4\pi R^2} A_{eff} \frac{1}{L_{at}}, \tag{5.1}$$

where P_r is the received power, P_t is the transmitted power, G_t is the gain of the transmitting antenna describing the directivity of the antenna, $1/4\pi R^2$-term counts for the power expanding isotropically, L_{at} is the atmospheric attenuation, A_{eff} is the effective area of the receiving antenna and σ_b is the backscattering cross-section of the object. Weather radars are usually monostatic i.e. single antenna is used for transmitting and receiving the signal, therefore the $A_{eff} = G_t \lambda^2 / 4\pi$ and inserting this to Eq.(5.1) leads to

$$P_r = \frac{P_t G_t^2 \lambda^2 \sigma_b}{(4\pi)^3 R^4 L_{at}}. \tag{5.2}$$

This is a general form of radar equation. For meteorological targets, there are many scatterers (total amount n) inside a radar measurement volume, for which the volume backscattering cross-section is defined as

$$\sigma_b = \frac{1}{V_{rdr}} \sum_{i}^{n} \sigma_{b,i}, \tag{5.3}$$

where $\sigma_{b,i}$ is the backscattering cross-section of a single scatterer i. Here single-scattering is assumed, and no the effect of multiple scattering is considered. The measurement volume V_{rdr} can be determined as a function of the half pulse length $\tau/2$ (Rinehart, 1997)

$$V_{rdr} = \pi \frac{R\theta}{2} \frac{R\phi}{2} \frac{\tau c}{2} \frac{1}{2\ln 2}, \tag{5.4}$$

where θ is the elevation angle and ϕ is the azimuth angle of the antenna in radians also considering the half-power beamwidths and R is the distance from the radar. The additional term $1/2 \log 2$ is added assuming the main lobe of the antenna to be Gaussian. Considering now the spherical Rayleigh-scatterer defined in Eq.(4.55) and combining this with Eqs.(5.2), (5.3) and (5.4), the radar equation can be written for spherical raindrops

$$P_r = \frac{P_t G_t^2 \theta \phi \tau c \pi^3 \left|K_w\right|^2 Z}{1024 \ln 2 \lambda^2 R^2 L_{at}} = \frac{Z}{C_r L_{at} R^2}, \tag{5.5}$$

when C_r is a radar constant containing the parameters related to the radar hardware properties as a function of the operating wavelength. Radar reflectivity factor Z is defined as (Rinehart, 1997)

$$Z = \frac{1}{V_{rdr}} \sum_{i}^{n} D_i^6, \tag{5.6}$$

or following a particle size distribution (Bringi and Chandrasekar, 2001)

$$Z = \int_D D^6 N(D) dD. \tag{5.7}$$

Reflectivity factor is expressed in $\mathrm{mm^6 m^{-3}}$, with D in mm and $N(D)$ in $\mathrm{mm^{-1} m^{-3}}$. Because of the wide range of values, the reflectivity factor is usually defined in logarithmic scale $Z = 10 \log_{10} \left(z / 1 \mathrm{mm^6 m^{-3}}\right)$.

The radar reflectivity factor is defined assuming that the observed hydrometeors are small spherical scatterers, where Rayleigh scattering approximation is valid. This is generally true for weather radars with longer wavelength, however, for higher frequencies or non-spherical hydrometeors either solid or mixed-phased, the equivalent reflectivity factor can be generalized as (Bringi and Chandrasekar, 2001)

$$Z_e = \frac{\lambda^4}{\pi^5 \left|K_w\right|^2} \int_D \sigma_b(D) N(D) dD, \tag{5.8}$$

with backscattering cross-section $\sigma_b(D)$ determined with other scattering methods. In addition, the radar constant with dielectric factor of water $|K_w|$ is usually applied to radar measurements directly and for scatterers other than raindrops the dielectric factor must be defined as $|K_p|^2$. For snow with known density of ρ_s, the dielectric constant $|K_s|^2 \approx \frac{{\rho_s}^2}{\rho_i^2}|K_i|^2$ can be computed by the two-phased Maxwell Garnett mixing formula of a mixture of ice and air (Bringi and Chandrasekar, 2001). The equivalent reflectivity factor of spherical snow particles (assuming a volume-equivalent diameter for snow) is given then as (Battan, 1973)

$$Z_e = \frac{|K_i|^2}{\rho_s^2 |K_w|^2} \int_D D^6 N(D) dD. \tag{5.9}$$

5.1.2 Radar observables

Reflectivity factor can be calculated for both horizontally and vertically polarized waves Z_h and Z_v; typically the horizontal polarization is used. Other dual-polarimetric observables can be determined from the scattering amplitude matrix defined in Eq.(4.33) and computed the corresponding scattering cross-sections from Eq.(4.27). This thesis is mostly applying only single polarization measurements, but to provide a general view of the current status of weather radar measurements, the polarimetric variables are briefly explained. The **reflectivity factor** in horizontal polarization is

$$Z_h = \frac{\lambda^4}{\pi^5 \left|K_w\right|^2} \int_D \sigma_{b,hh}(D) N(D) dD, \tag{5.10}$$

The value of the cross-section is dependent on the actual shape and size of the scattering particle, but also on permittivity value. In microwave region, ice produces lower Z_h and Z_v than liquid precipitation because of lower dielectric effects. The reflectivity factor is sensitive to calibration and the attenuation in heavy precipitation affects Z even at lower frequencies.

The Doppler radars observe the **reflectivity-weighted fall-velocity** (Russchenberg and Ligthart, 1996)

$$v_Z = \frac{\int_D v\,(D)\,\sigma_{b,hh}\,(D) N\,(D)\,dD}{\int_D \sigma_{b,hh}\,(D) N\,(D)\,dD}. \tag{5.11}$$

The **differential reflectivity** Z_{dr} is a measure describing the reflectivity weighted mean axis ratio of hydrometeors in a volume (Straka et al., 2000) and it is also expressed in logarithmic scale. For scatterers, which are oriented with their symmetry axis vertical in the plane of polarization, axis ratios less than unity (oblate particles) produce positive Z_{dr} and axis

ratios larger than unity (prolate particles) produce negative Z_{dr}. Canting angle changes the effective lengths of the scatterers along the directions of orthogonal polarized transmitted electric fields, and hence also Z_{dr} is affected. Likewise also the nonuniform structure of scatterer, especially if the permittivities of components are different, has an impact on Z_{dr}.

$$Z_{dr} = \frac{Z_h}{Z_v} = \frac{\int_D \sigma_{b,hh}(D) N(D)\, dD}{\int_D \sigma_{b,vv}(D) N(D)\, dD}. \tag{5.12}$$

The **linear depolarization ratio** (LDR) describes the ratio between the backscattered power in the cross-polarization channel and the co-polarization channel

$$LDR_h = \frac{Z_{hv}}{Z_{hh}} = \frac{\int_D \sigma_{hv}(D) N(D)\, dD}{\int_D \sigma_{hh}(D) N(D)\, dD}. \tag{5.13}$$

For a perfect sphere LDR has value of negative infinity, and with a more complex shape or with canting effects it increases. For hydrometeors, the value is usually between -35 and - 15 dB.

The **co-polarized correlation coefficient** using the backscattering alignment with the scattering amplitudes is

$$\rho_{hv} \exp(-j\delta_{hv}) = \frac{\left\langle \bar{f}_{hh} \bar{f}^*_{vv} \right\rangle}{\left[\left\langle \left| \bar{f}_{hh} \right|^2 \right\rangle \left\langle \left| \bar{f}_{vv} \right|^2 \right\rangle \right]^{1/2}}, \tag{5.14}$$

with $\langle\rangle$ indicating ensemble averaging. The argument of the co-polarized correlation coefficient δ_{hv} is also called **backscatter differential phase**. Its nonzero values for partially aligned hydrometeors correspond that the scattering is no longer in Rayleigh regime (Straka et al., 2000). For resonance regime scatterers it depends on the size of nonspherical hydrometeors and can be used to interpret their size and type. The amplitude ρ_{hv} measures the correlation between the horizontally and vertically polarized waves. It is a useful quantity to distinguish hydrometeors from non-meteorological scatterers and e.g. the melting layer has a distinct ρ_{hv} signature.

The **specific differential phase** is the difference between propagation constants for horizontally and vertically polarized waves. It is defined by the forward scattering amplitudes (Bringi and Chandrasekar, 2001)

$$K_{dp} = 10^3 \left(\frac{180\lambda}{\pi} \right) \int_D \mathrm{Re}\left[\left\langle \bar{f}_{hh} - \bar{f}_{vv} \right\rangle \right] N(D) dD. \tag{5.15}$$

Basically, K_{dp} discriminates between statistically isotropic and anisotropic hydrometeors. Isotropic hydrometeors produce similar phase shifts for horizontal and vertical polarized waves, and the detected differences are

then due to anisotropic constituents. Generally, the magnitude of K_{dp} increases as both oblateness (or prolateness) and also as the dielectric constant increase. The specific differential phase is independent of receiver/transmitter calibration and attenuation. It is also less sensitive than reflectivity factor to variations of size distributions. It can be used to define the difference in attenuation between the two polarizations.

The **specific attenuation** for both polarizations and differential attenuation are calculated with the forward scattering amplitudes (Bringi and Chandrasekar, 2001)

$$A_h = 8.686 \cdot 10^3 \left(\frac{2\pi}{k}\right) \int_D \mathrm{Im}\left[\langle \bar{f}_{hh} \rangle\right] N(D) dD \tag{5.16}$$

$$A_v = 8.686 \cdot 10^3 \left(\frac{2\pi}{k}\right) \int_D \mathrm{Im}\left[\langle \bar{f}_{vv} \rangle\right] N(D) dD \tag{5.17}$$

$$A_{dr} = A_h - A_v. \tag{5.18}$$

5.2 Modeling of bright band

The melting layer appears as a bright band in weather radar reflectivity measurements (Figure 5.1). Since the beginning of the weather radar era, many experimental or theoretical studies have been carried out to quantify fine characteristics of microphysics in the melting layer, e.g. habit of the primary snowflakes, influence of the temperature and humidity gradients, impact of the vertical air velocity, and effect of the snowflake aggregation and break-up, these are discussed in Section 2.3.

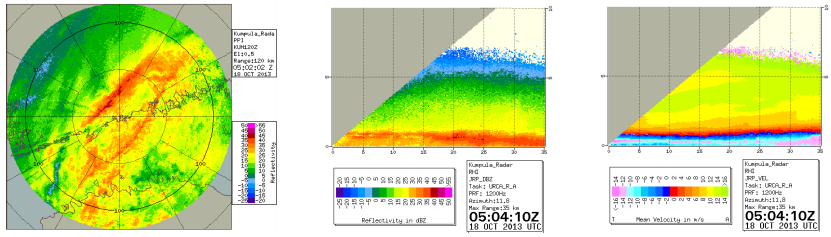

(a) **(b)** **(c)**

Figure 5.1. a) PPI - scan of stratiform precipitation with the distinguishable bright band. RHI - scan of the vertical structure of precipitation with the bright band observed b) in reflectivity factor profile and c) in fall velocity profile. Image credits: Matti Leskinen with permission.

The main cause for the observed increase in the reflectivity factor is the change in particle permittivity due to melting, as this is substantially higher for water than ice in the microwave region. The melting starts at

the periphery of the particle, and the melted particle appears to radar like a large and slowly falling liquid hydrometeor leading to higher backscattering and extinction cross-sections. As the melting process continues, the size of the mixed-phase particles will decrease reducing the backscattering, and their fall velocity will increase. Due to the increased fall velocity, particle number concentration decreases and this further decreases the observed reflectivity factor value. Eventually the melting particles will collapse into raindrops. Figure 5.2 shows typical vertical profiles of reflectivity factor and fall velocity in melting layer. The original snow particle habit and density, the temperature and the relative humidity profiles and the precipitation rate also affect to the shape and intensity of a bright band. Klaassen (1990) stated that the higher the density of ice particles above the melting layer, the weaker the bright band is. This was also shown in (Fabry and Zawadzki, 1995) by studying the long-term observations of bright band dependence on precipitation intensity, and in (Fabry and Szyrmer, 1999) by testing the melting layer model with different $m(D)$ relations for snow before melting. Zawadzki et al. (2005) modeled also the effect of riming at the top of the melting layer and compared the results to radar observations. In a case of low-density snow aggregates, the increase of reflectivity can be 15 dB relative to the corresponding rain reflectivity. For rimed snow, the enhanced peak is less than 8 dB, and the fall speed is between 2-4 ms^{-1} at the top of the bright band, and with denser graupel, the peak is around 5 dB with a fall speed of 3-4 ms^{-1} at the top (Zawadzki et al., 2005). Other aspects such as changes in particle size distribution, indicating aggregation and breakup of precipitation, were found to affect little to the average bright band intensity (Fabry and Zawadzki, 1995).

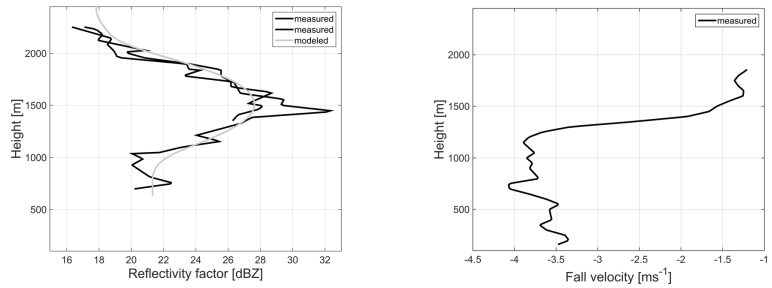

(a) **(b)**

Figure 5.2. Precipitation profile from 21 September, 2010. a) Black solid lines: radar reflectivity factor measured with scanning C-band radar and a gray line: modeled profile b) a black solid line: measured with vertical pointing airborne W-band radar.

The microphysical model utilizes the temperature and humidity profile and defines the rate of melting, the changes in size distribution and fall speed of hydrometeors. It specifies the volume fractions of ice, air, and water in an ensemble of particles at the specific height. The electromagnetic model calculates the scattering properties of hydrometeors as a function of their size, the melted mass fraction, and the radar wavelength, and connects these to radar observations. Due to computational reasons, Rayleigh approximation, Mie solution or T-matrix method is usually used for scattering calculations and therefore the permittivity of melting particles needs to be estimated with some form of EMA. Formulas such as Maxwell Garnett, Bruggeman, and Wiener, using various approaches on how to mix the components (three-phase or two consecutive two-phase, selection of matrix and inclusion media) are presented in the literature and the methods are compared in (Meneghini and Liao, 1996; Fabry and Szyrmer, 1999; Olson et al., 2001; Battaglia et al., 2003; Matrosov, 2008) and in Publication I. The used scattering methods and EMAs are shown in Table 5.1

One of the pioneering works in the bright band modeling is the model presented by Dissanayake and McEwan (1978a). It was one of the first simplistic, but effective models, and e.g. Hardaker et al. (1995) use this model with some modifications. Where as Dissanayake and McEwan (1978a) modeled the melting particles with ice core and water shell, Hardaker et al. (1995) used a solution of snow core and water shell, both applying analytic Lorenz-Mie solution for coated spheres by Aden and Kerker (1951). Coated spheres are also utilized in (Yokoyama and Tanaka, 1984). Both models utilized the Wiener mixing rule to define permittivity of snow. For snowflakes, in which the melted water is drifting to the inner parts of the particle, the water layer at the particle surface is not representative. This is more descriptive for modeling of melting high-density graupel or hail. If melting snowflake is modeled with water coating, the enhanced reflectivity factor is generally overestimated. Klaassen (1988) defined a more realistic dielectric constant of melting particles by consecutively mixing the two-phase Maxwell-Garnett mixing rule of random elliptical spheroids from (Bohren and Battan, 1982). He applied the rule firstly mixing the ice inclusions to water matrix and then air inclusions to wet ice matrix. Fabry and Szyrmer (1999) used six different models to define the permittivity, and they also utilized the solution of concentric spheres with different densities and orders of mixing, these are stated in Table 5.1. It was demonstrated that the various mixing ways and assumed topologies

Researchers	Shape	EMA	Method
Dissanayake and McEwan (1978a)	sphere	two-layered with water shell and ice core	Aden and Kerker (1951)
Hardaker et al. (1995)	sphere	two-layered with water shell and air-ice core Wiener mixing rule, Oguchi (1983)	Aden and Kerker (1951)
Yokoyama and Tanaka (1984)	sphere	two-layered with water shell and ice-air core Wiener mixing rule	Aden and Kerker (1951)
Klaassen (1988)	sphere	air inclusions in ice-water mixture Maxwell Garnett mixing rule, Bohren and Battan (1982)	Lorenz-Mie Theory
Russchenberg and Ligthart (1996)	spheroid $a_{xs} = a_{x1} + \frac{a_{x2}-a_{x1}}{D_2-D_1} D_s - \frac{a_{x2}-a_{x1}}{D_2-D-1} D_1$, with $D_{1,2}$ diameters of smallest and largest particle and $a_{x1,x2}$ axis ratios of smallest and largest particle $a_{xr} = 1.0 - 0.05 D_r$ Morrison and Cross (1974) $a_{xms} = a_{xs} + f_V^8 (a_{xr} - a_{xs})$ orientation $\Delta\delta_{ms} = \Delta\delta_s + (\Delta\delta_r - \Delta\delta_s) f_V^3$	average of two effective permittivities snow (ice inclusions in air matrix) inclusions in water matrix and air inclusions in water-ice (ice inclusions in water) matrix Maxwell Garnett mixing rule, de Wolf et al. (1990)	Rayleigh approximation
Meneghini and Liao (1996)	sphere	comparing different methods ice-water CG-FFT, Meneghini and Liao (1996) ice-water Bruggeman mixing rule in Eq.(4.46) ice-water Maxwell Garnett mixing rule, Bohren and Battan (1982) ice-water Debye mixing rule Bohren and Battan (1982)	Lorenz-Mie theory
Fabry and Szyrmer (1999)	sphere	Model 0:two-layered, water shell and ice inclusions in air matrix core Model 1: [Ice inclusions in air matrix] inclusions in a water matrix Model 2: Air inclusions in [Ice inclusions in water matrix] Model 3: [Ice inclusions in water matrix] inclusions in as air matrix Model 4: Like model 3, two-layered with core denser that shell Model 5: two-layered core like Model 2, outer shell like Model 3 Maxwell Garnett mixing rule, Bohren and Battan (1982)	Lorenz-Mie theory Aden and Kerker (1951)
Giangrande (2007)	spheroid $a_{xms} = a_{xs} + f_m (a_{xr} - 0.8)$, with $a_{xs} = 0.8$ and a_{xr}, Brandes et al. (2002) canting angle $\Delta\delta_{ms} = \Delta\delta_s + f_m (\Delta\delta_r - \Delta\delta_s)$, with $\Delta\delta_s = 40^\circ$ and $\Delta\delta_r = 10^\circ$	Model A: snow (ice in an air matrix) inclusions in water matrix Model B: water inclusions in snow matrix (air matrix with ice inclusions) Model C: $\epsilon_{ms} = \frac{1}{2}\left[(1-p)\epsilon^A + (1+p)\epsilon^B\right]$, with $p = erf\left[\frac{1-f_V}{f_V} - 0.2\right]$, with $f_V > 0.01$ Maxwell Garnett mixing rule, Bohren and Battan (1982)	Rayleigh, TMM
Botta et al. (2010)	strings of touching spheres with restricting shape taken as a spheroid of axis ratio of 0.6	mixture of spheres with permittivity of ice, water	GMM
Tyynelä et al. (2014)	spheroid of axis ratio 0.6	upper part: mixture of ice and air, lower part: mixture of ice and water Maxwell Garnett mixing rule Bohren and Battan (1982)	DDA, Rayleigh TMM, Lorenz-Mie theory
Johnson et al. (2016)	needle aggregate and dendrite aggregate	ice dipoles are replaced to water dipoles simulating early stage melting process	DDA

Table 5.1. Scattering properties of melting snow particles.

had a significant effect on the bright band peak intensity, the difference of the mixing topologies can be in the order of 10 dB (Fabry and Szyrmer, 1999). The six different mixing topologies were compared with two precipitation cases, for light (1 mmh^{-1}) and moderate (5 mmh^{-1}) stratiform rain observed at X-band and UHF radars. It was shown that with the most realistic and complex model, Model 5, the calculated reflectivity factor profile corresponded best with the observations in both cases. Similar results were obtained in the other comparisons as well, a common conclusion was that a mixture, where dry snow (ice inclusions in air matrix) inclusions are set in water matrix overestimates the reflectivity factor peak by around 5 dB and more accurate approach is to use a mixture of wet ice (ice inclusions in water matrix) inclusions in air matrix (Fabry and Szyrmer, 1999; Olson et al., 2001; Battaglia et al., 2003) and Publication I. In (Fabry and Szyrmer, 1999) this effective permittivity topology was chosen for the outer shell of the concentric sphere in the Model 5. The CG-FFT - model of (Meneghini and Liao, 2000) seem to underestimate the formed reflectivity peak and is more suitable for modeling weak bright bands (Battaglia et al., 2003). Giangrande (2007) changed the mixing order as a function of melted volume fraction (Model C in Table 5.1); for small volume fractions the permittivity was weighted towards the value of Model B (snow matrix with water inclusions) and for higher volume fractions toward that of Model A (water matrix with ice inclusions). Compared with S-band radar observations, the Model C seem to catch scattering behavior of the both initial and final stage of melting, where using a single mixing topology would fail.

Melting layer has discernible signatures also in polarimetric observables, Z_{dr}, ρ_{hv}, K_{dp}, and LDR. There are peaks in Z_{dr} and LDR profiles and a drop in the ρ_{hv}, and these are employed in melting layer detection algorithms e.g. (Tabary et al., 2006; Brandes and Ikeda, 2004; Matrosov et al., 2007; Giangrande et al., 2008). The polarimetric profiles of melting layer have been modeled in e.g. (Russchenberg and Ligthart, 1996; Giangrande, 2007; Ryzhkov et al., 2008; Trömel et al., 2014). It is shown in (Giangrande, 2007) that without presence of large particles inside the melting layer grown through aggregation process the pronounced polarimetric signatures of Z_{dr} and ρ_{hv} cannot be modeled, and also the large observed values of backscatter differential phase cannot be produced (Trömel et al., 2014).

One of the driving forces in the melting layer research, both in radar me-

teorology and telecommunications, is the attenuation effect of the melting layer (Smith, 1986; Klaassen, 1990; Leitao and Watson, 1986; Dissanayake et al., 1997; Battaglia et al., 2003). The bright band attenuation is notably higher than for the corresponding rain. Even though the melting layer is relatively thin, its extinction can be significant for slant beam measurements or at higher frequencies (Matrosov, 2008). In Publication I the focus is on estimating the attenuation at C-band weather radar measurements related microphysical conditions of snow above the melting layer.

5.3 Radar-based snowfall estimate

The connection between the equivalent radar reflectivity Z_e and snowfall rate S is typically given in power-law format, which is determined through a regression fit for some snowstorms

$$Z_e = a_{zs} S^{b_{zs}}. \tag{5.19}$$

Since the research of Marshall and Gunn (1952), many relations are presented in literature e.g. (Fujiyoshi et al., 1990; Langille and Thain, 1951; Marshall and Gunn, 1952; Imai, 1960; Ohtake and Hemni, 1970; Sekhon and Srivastava, 1970; Carlson and Marshall, 1972; Puhakka, 1975; Rasmussen et al., 2003; Saltikoff et al., 2015). Tables listing many of the factors are found e.g. in (Gray and Male, 1981; Rasmussen et al., 2003) and Publication IV.

However, despite the extensive research, quantitative snowfall estimates are still challenging, because of the significant variability of the microphysical properties of snow. In Figure 5.3 the wide range of $Z_e - S$ relation can be observed, especially the prefactor a_{zs}, is deviating strongly and is dependent on various parameters such as the crystal type, degree of riming and aggregation, density, and terminal velocity (Rasmussen et al., 2003). In Publication IV the dependence of the factors are studied, and it is shown, how the prefactor a_{zs} is affected by the $m(D)$ and $v(D)$ relation parameters and the PSD parameters. These properties can change even inside a snow storm, and thus one relation suitable for all snowfalls may be impossible to reach (Passarelli, 1978; Rasmussen et al., 2003; Saltikoff et al., 2015). The variability of the factors of $Z_e - S$ relation in one snowfall event is demonstrated in Figure 5.4 from one of the studied cases in Publication IV. The theoretical exponent b_{zs} is derived by assuming an exponential PSD and calculated from the exponents of $m(D)$ and $v(D)$ relations, and the

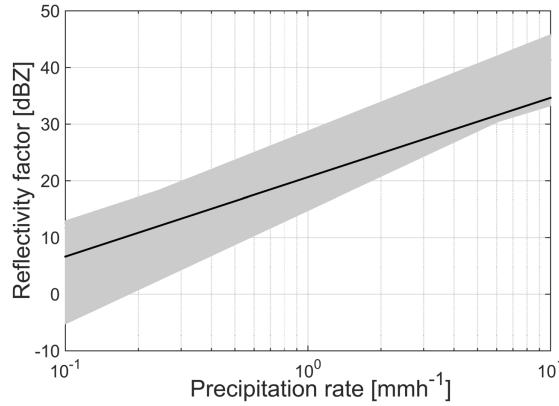

Figure 5.3. The gray area is depicted from different $Z_e - S$ relations from the literature (Gray and Male, 1981; Rasmussen et al., 2003; Huang et al., 2010, 2015; Saltikoff et al., 2015) and in Publication IV, and black solid line is the long-term averaged relation determined in Publication V. The relations are determined for frequencies in Rayleigh scattering regime (S-, C-, and X-band).

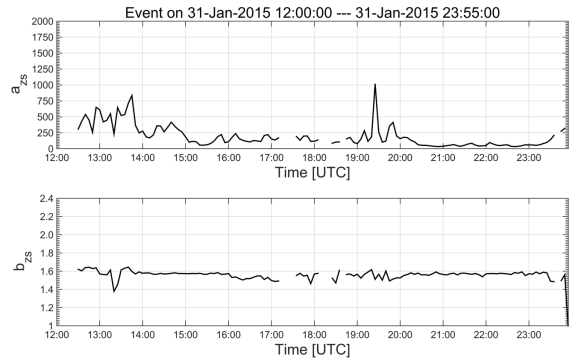

Figure 5.4. Time series of the prefactor a_{zs} and theoretical exponent b_{zs} of $Z_e - S$ relation assuming exponential PSD for 31 January, 2015.

variety is small with a mean value of 1.56. The prefactor a_{zs} is determined from retrieved Z_e and S from measurements of video-disdrometer PIP and theoretical b_{zs}. The value of a_{zs} is changing from 34 to 1020 during this snowfall event.

Research has mainly been focusing on determining a so-called climatological $Z_e - S$ relation that could determine snowfall rate as a local solution. For example, Finnish Meteorological Institute (FMI) has defined experimental factors $Z_e = 100S^2$ based on gauge comparison (Saltikoff et al., 2010) and utilizing this relation decreased the underestimation of the snowfall rate based on earlier applied factors from (Sekhon and Srivastava, 1970). However, it must be remembered that the systematical overesti-

mation of radar measurements can be related to $Z_e - S$ relation, but also to underestimation by the gauges. Nevertheless, it is shown in (Huang et al., 2015) that the normalized bias between radar-derived and gauge-measured accumulation was reduced from 96% of the fixed experimental FMI relation to 28% when using event specific $Z_e - S$ relations. Also, it is stated in (Matrosov et al., 2009) that there can be a factor of two difference in precipitation rate with different factors selected for the $Z_e - S$ relation. Hence for accurate snowfall estimate in addition to equivalent radar reflectivity, some extra information is needed, e.g. the classification of the prevailing snow type, at least on coarse scale, whether the prevailing particle type is low-density aggregates or denser rimed particles.

The quantitative snowfall precipitation estimation can be improved by using adjustable $Z_e - S$ relation. Challenges are, firstly to derive parametrization for adaptive $Z_e - S$ relation, and secondly to retrieve from operational measurements the conditions to guide the relation (Saltikoff et al., 2015). In Rasmussen et al. (2003) an algorithm for adaptive $Z_e - S$ relation is demonstrated, where the exponent b_{zs} was changing between fixed values for rain and snow, and the prefactor a_{zs} was adjusted by gauge comparison. The algorithm is also utilized in nowcasting snowfall with a lead time of 1 h. A strong dependence of the prefactor a_{zs} of the $Z_e - S$ on PSD parameters is shown in (Rasmussen et al., 2003; Bukovcic et al., 2015) and in Publication IV, but the current routinely recorded meteorological data or single-frequency radar measurements do not have established procedure to retrieve these parameters. With low precipitation intensity, the prefactor of the $m(D)$ relation can partly explain the different values of the prefactor a_{zs}. Here the recent advances in polarimetric radar algorithms, e.g. in (Kennedy and Rutledge, 2011; Bechini et al., 2013; Moisseev et al., 2015; Thompson et al., 2014; Grazioli et al., 2015), have shown skill to identify the prevailing snow type from the radar measurements and the prefactor could be changed accordingly. In some countries a fixed $Z - R$ relation is assumed regardless of the phase of the precipitation, and the introduced error is corrected by the gauge-adjustment (Smalley et al., 2014; Norin et al., 2015). On U.S. continent a MRMS/Q3 precipitation product classifies precipitation to snow if the wet-bulb temperature is below 0 °C and thus $Z_e = 75S^{2.0}$ for snowfall estimate is applied (Zhang et al., 2011b). Because Q3 is based on the S-band radars in NEXRAD network, the quality-control threshold of 5 dBZ prevents the detection of light snowfall. According to Chen et al. (2015) Q3 product is underestimating precipitation in winter

and spring, and Q3 snowfall estimate has not been validated with e.g. to independent gauge observations (Chen et al., 2016).

5.4 Satellite-based snowfall estimate

Since the late 1990s, satellite instrumentation suitable for observing snowfall have been launched, e.g. multi-frequency radiometers Advanced Microwave Sounding Unit-B (AMSU-B) or Microwave Humidity Sounder (MHS), Atmospheric Technology Microwave Sounder (ATMS) and GPM Microwave Imager (GMI). So far there are only a few suitable active sensors operating such as Cloud Profiling Radar (CPR) at W-band and Dual-Frequency Precipitation Radar (DPR) at Ku/Ka-band. Snowfall retrieval is challenging for both active and passive instruments, because of weak and complex signatures of snow in microwave frequencies e.g. (Kidd and Huffman, 2011; Ferraro et al., 2005; Liu, 2008; Liu and Seo, 2013; Skofronick-Jackson et al., 2013b) and comparing to rain, there are still significant uncertainties with detection and, especially, with quantitative estimation of snowfall.

5.4.1 Active sensors

The advantage of active sensors compared with passive sensors, is the high spatial resolution, which is in the order of kilometers with respect to tens of kilometers. Active sensors can also provide a 3D profile of the cloud structure. The nadir-looking CPR on board of polar orbiting satellite CloudSat (Stephens et al., 2008) has been utilized for snowfall surface estimates e.g.(Hudak et al., 2008; Liu, 2008; Kulie and Bennartz, 2009; Hiley et al., 2011; Norin et al., 2015; Chen et al., 2016). It is sensitive enough to detect light precipitation including drizzle and snowfall (Tanelli et al., 2008). The disadvantages of the relatively high frequency of CPR, is the significant attenuation of the signal and the issue of multiple scattering, both of these influencing intense snowfall observations (Hudak et al., 2008). Active sensors also suffer from surface clutter contamination e.g. the lowest five bins of CPR are filtered. Thus the closest observations to the ground are measured at the height of 1.3 km (Kulie and Bennartz, 2009) and microphysical processes affecting to precipitation intensity at low altitudes can be missed. The effect of this blind zone on global statistics was studied in (Maahn et al., 2014) and concluded to cause an underestimation

of reflectivity up to 1 dB, resulting in the number of observed events to alter by $\pm 5\%$ and the precipitation amount being underestimated approximately 10%. DPR on board of GPM Core Observatory has two radars for measuring precipitation, also designed to capture light precipitation and snowfall. The operating wavelengths are Ku-band and Ka-band, with the minimum detectable signal level of 12-14 dBZ (Toyoshima et al., 2015) and 12 dBZ, respectively (Hou et al., 2014). The sensitivity of the radars is too high for detecting the majority of the snowfall events and a significant amount of the total global snowfall accumulation will be missed by the GPM radars if compared to CPR (Kulie and Bennartz, 2009).

As with weather radars, the observed equivalent reflectivity factor Z_e for space-borne radars is usually converted to the precipitation rate S with experimental factors that have a power-law relation. The factors are dependent on e.g. particle type, particle size distribution, but also strongly related to the used measurement frequency. With high-frequency radars in the millimeter range, scattering is in a resonance region, and therefore $Z_e - S$ relations differ from those that are typically used for the centimeter-wavelength radars (Matrosov et al., 2008). It is discussed in (Kulie and Bennartz, 2009) that the modeled Z_e for a given snowfall rate is sensitive to the chosen scattering method and the used particle model. At a snowfall rate of 1.0 mmh^{-1}, the potential range, with different model assumptions of Z_e, can be close to 14 dB, representing a large potential source of uncertainty in the retrieved snowfall rates from radar data. Different $Z_e - S$ relations are derived for W-band e.g. in (Matrosov et al., 2008; Kulie and Bennartz, 2009; Liu, 2008).

5.4.2 Passive sensors

In the microwave frequency regime the atmosphere is relative transparent, especially for frequencies below 100 GHz. The specific attenuation at frequencies 1-300 GHZ is plotted in Figure 5.5 for dry air and for air containing water vapor density of 7.5 gm^{-3}. At lower microwave frequencies, attenuation by clouds is relatively small and surface emissivity is dominant when observed from space. Passive microwave satellite sensors measure the electromagnetic radiation emitted and scattered by Earth's surface and atmospheric particles integrated over a vertical column. The underlying assumption is that precipitation can be identified either by the emission of rain droplets, which increase the observed radiation at the sensor, or from the decrease of the radiation caused by the scattering effect

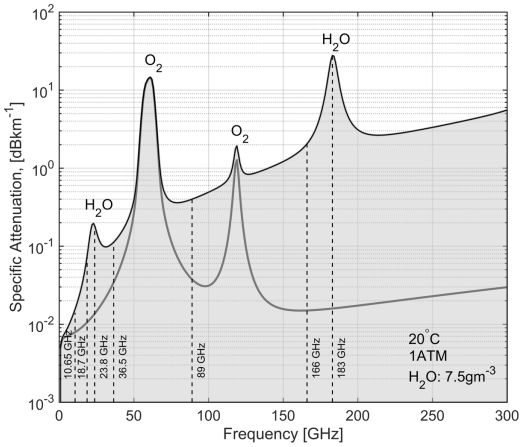

Figure 5.5. Specific attenuation for dry air with gray line and for air containing water vapor density of 7.5 gm^{-3} at each frequency between 1-300 GHz according to the International Telecommunication Union (ITU) atmospheric gas attenuation model (ITU-R Recommendation, P.676-10, 2013). The frequencies of GMI radiometer are plotted with dashed line.

of ice particles (Kidd and Huffman, 2011). However, passive measurements have difficulties in distinguishing the weak scattering signature of snowfall from the higher ground emissivity, especially from the snow-covered surfaces (Bennartz and Bauer, 2003; Noh et al., 2006; Munchak and Skofronick-Jackson, 2013; Kongoli et al., 2015). At higher frequencies, above 100 GHz, the scattering of ice particles is shown to be significant and the surface emission component can be screened by the water vapor absorption as shown in Figure 5.5. However, the scattering effect is also impacted by water vapor in the upper atmosphere (Skofronick-Jackson et al., 2004).

The observed radiation at the passive microwave sensor at single frequency has a non-unique response to precipitation (Bennartz and Bauer, 2003; Skofronick-Jackson et al., 2013a), and usually, multi-channel algorithms are used for precipitation detection (Kidd and Huffman, 2011). For example with GMI 13 channels ranging from 10 - 183 GHz are employed, these are shown in Figure 5.5. The lower channels are for observing the liquid precipitation, channel close to 21 GHz is for correction of the water vapor emission, and higher channels (> 89 GHz) are used for snowfall detection (Hou et al., 2014).

Passive algorithms are divided into two groups according to the used technique; empirical and physical algorithms (Kidd and Huffman, 2011). Empirical algorithms are based on comparison between the surface mea-

surements and responses of the different frequency channels e.g. (Kongoli et al., 2003, 2015; Chen et al., 2003; Liu and Seo, 2013). These methods are simple to implement, but suffer from uncertainties induced from the measurement setup and require a regional calibration, because of the inherent differences in precipitation systems (Kidd and Huffman, 2011). In physical algorithms, the measured radiation is coupled with either modeled or observed profiles. The benefit of physical approach is that by utilizing the Bayesian approach with the modeled or observed *a priori* database of atmospheric profiles, also the vertical structure of the precipitation can be retrieved and more information on precipitation can be obtained e.g. (Skofronick-Jackson et al., 2004; Skofronick-Jackson and Johnson, 2011; Kim et al., 2008; Noh et al., 2006, 2009; Kummerow et al., 2015). In a Bayesian GPROF (Goddard Profiling)-algorithm the observational database has been utilized since 2010, when modeled database was replaced with operationally generated database of the Precipitation Radar (PR) and TRMM Microwave Imager (TMI) of the Tropical Rainfall Measuring Mission (TRMM)-satellite (Kummerow et al., 2011, 2015). Precipitation algorithms based on the Bayesian scheme are sensitive to the accuracy of the *a priori* databases, and the majority of the errors induced to the algorithms, are from the incompleteness of the created *a priori* profiles (Bauer et al., 2001; Kummerow et al., 2006).

The snow detection threshold for passive radiometers operating at 166 GHz was modeled to be close to 0.5 - 1.0 mmh^{-1} in LWE rate, and in ideal conditions around 0.2 mmh^{-1} (Skofronick-Jackson et al., 2013a). Similarly, based on observations, it was demonstrated that the snowfall rate threshold over a snow-covered surface is 0.89 mmh^{-1}, and can be approved to 0.44 mmh^{-1} by applying *a priori* information of the snow cover (Munchak and Skofronick-Jackson, 2013). The snowfall detection is dependent on the cloud vertical structure as well as the scattering particle type, precipitation intensity, and surface conditions. The performance of the algorithms varies in different precipitation events, for example, heavy blizzards, with high cloud system and large ice particle content, can be easily detected e.g. with AMSU-B instrument over bare ground (Skofronick-Jackson et al., 2004; Foster et al., 2012; Noh et al., 2006; Skofronick-Jackson et al., 2013b). However, light snow events, such as "diamond dust", have a weak signal-to-noise ratio and is challenging to observe with passive instruments (Radok and Lile, 2013).

5.4.3 Ground validation

The target of ground validation is to identify uncertainties in satellite-based products and to improve satellite-based algorithms. In the GPM satellite mission the ground validation is divided into three approaches (Hou et al., 2014)

- **Direct product validation** is performed between the satellite- and ground-based precipitation products of national/international validation networks. The goal is to identify significant discrepancies and provide information for the physical validation.

- **Physical validation** concentrates on testing and improving the algorithm retrieval assumptions based on modeling and microphysical studies.

- **Integrated science validation** couples the satellite-products to prediction models to assess the integrated performance.

In Publication V a method to validate space-based surface snowfall estimate is proposed. The method is based on a combination of detailed microphysical surface observations and radar measurements. Hence it is addressing both the direct as well as the physical validation and providing insight into the snow retrieval algorithm development.

Conventionally the detection of space-based products is quantified by utilizing the well-known forecasting skill scores. The skill scores are scalar attributes to the joint distribution of forecasts and observations describing the relative accuracy of forecast performance to some reference set (Wilks, 2011). Typically non-probabilistic verification is displayed as a combination of forecast and event pairs as a contingency table as shown in Figure 5.6. The 2×2 contingency table presents correctly estimated hits a, false alarms b, misses c and correct rejections d. There are a large number of different skills scores developed based on the contingency table such as **Heidke Skill Score (HSS), Critical Success Index (CSI), Probability of Detection (POD) and False Alarm Rate (FAR)** (Wilks, 2011). Scalar skill scores are convenient to use, but there is a variety of ways for forecasts to go right or wrong. Thus referring the performance in a single scalar number, involves a loss of information.

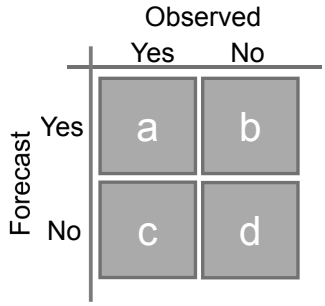

Figure 5.6. One-to-one correspondence between the forecast and observed values presented in the 2×2 contingency table. (Wilks, 2011)

HSS is the proportion correctly estimated events related to random forecasts that are statistically independent observations

$$HSS = \frac{2(ad - bc)}{(a + c)(c + d) + (a + b)(b + d)}. \tag{5.20}$$

CSI is a metric presenting the skill to detect correctly the event relative to all the correctly or falsely detected snowfall, but it excludes the analysis of detecting correctly also the non-occurrences of the event. CSI is defined as

$$CSI = \frac{a}{a + b + c}. \tag{5.21}$$

POD is also called the hit rate, it describes the ratio of correctly detected events to number of all occurred events

$$POD = \frac{a}{a + c}. \tag{5.22}$$

FAR is the number of false alarms divided by the total amount of non-occurrences of the event, which can be stated as

$$FAR = \frac{b}{b + d}. \tag{5.23}$$

The snowfall rate estimated by CPR of CloudSat has been widely validated, and both the detection and the retrieved snowfall rate estimate are comparing well with ground observations (Matrosov et al., 2008; Hudak et al., 2008; Kulie and Bennartz, 2009; Smalley et al., 2014; Norin et al., 2015; Chen et al., 2016). Hudak et al. (2008) compared the snowfall detection of CPR with C-band weather radar observations and noted that the most frequent cause of a missed snowfall was the filtered echoes due to the ground clutter, and the most common cause of a false detection was an incorrect precipitation threshold in the used algorithm. Matrosov et al. (2008) compared the CloudSat snowfall retrieval to vertically pointing ground-based 8-mm cloud radar and to S-band precipitation radar. They

demonstrated that millimeter-wavelength cloud radars could be used effectively also for snowfall retrievals, and a typical difference between the CPR and S-band radar estimates of snowfall rate was within a factor of 2, which is of the order of the uncertainty of both estimates. Norin et al. (2015) compared the snowfall estimates of CPR over the Swedish ground-based radar network (Swerad) for winter observations during 2008-2010. Intercomparison showed that both instruments gave similar precipitation rate values in the range of 0.01 - 1.0 mmh^{-1}, and the best agreement is achieved when the measured volumes are located 46-82 km distance from the nearest radar. This study strengthens earlier results, e.g. with higher precipitation rates (> 1 mmh^{-1}) CPR suffers from attenuation and multiple scattering effects, and underestimates the rate as also shown e.g. in (Cao et al., 2014). The skill scores, POD and FAR, demonstrated that both instruments have difficulties with shallow snow events; CPR because of the filtered lower bins to avoid ground clutter and Swerad because of the decreased sensitivity with increasing distance from the radar and of the overshooting lower precipitation systems with long distances. In the vicinity of the radar, the precipitation rate of Swerad suffers from ground clutter. The general agreement of precipitation rates of the two instruments is good, and no clear bias is observed. The snowfall estimate of CPR is also compared with ground observations of NOAA/National Severe Storms Laboratory's Multi-Radar-Multi-Sensor (MRMS/Q3) in (Chen et al., 2016). The CPR estimate shows a high POD of 86.10% for snowfall detection, but for heavy snow ($\geq$ 2.5 mmh^{-1}) the score drops to 36.76%. It seems that the CPR snowfall algorithm underestimates the precipitation rate with shallow events below 3 km. Generally, the algorithm is found to overestimate light snowfall events (< 1 mmh^{-1}) by 7.53%, but underestimate rate in moderate (1-2.5 mmh^{-1}) and heavy snowfall (> 2.5 mmh^{-1}) by 42.33% and 68.73%, respectively (Chen et al., 2016).

Passive space-based snowfall estimates have been validated e.g. in (Kim et al., 2008; Noh et al., 2006; Kongoli et al., 2015). The experimental algorithm of (Kongoli et al., 2015) applied to ATMS measurements is validated against surface meteorological data during two winters 2012-2013 and 2013-2014. The National Centers for Environmental Prediction (NCEP) multi-sensor Stage IV hourly data set is used for validation with 480 weather stations. NCEP Stage IV is frequently used as a benchmark. The snow events were divided into warmer and colder temperature regimes. FAR for the warmer events was low with 4.0%, and POD was 73%, for

colder cases these were 14% and 55%, respectively.

5.5 Multi-frequency radar signatures of snowflakes

Snowfall rate estimate based on single frequency radar measurements exhibit a wide range of uncertainty due to the unknown microphysical properties of snowfall (Liu, 2008; Kulie and Bennartz, 2009; Hiley et al., 2011). The equivalent reflectivity factor (Eq.5.9) and precipitation rate (Eq.3.2) are dependent differently on the particle size, PSD and $m(D)$ (Matrosov, 1998). In addition, the $v(D)$ relation influences the precipitation rate. The PSD, if described with gamma distribution, has three unknown parameters, and the $m(D)$ and $v(D)$ both are typically described with two unknown parameters. Of the three PSD parameters, N_w and D_0 are the most important. The D_0 can be estimated by dual-frequency radar measurements (Matrosov, 1992, 1998; Liao et al., 2005).

In the dual-wavelength method, simultaneous and collocated radar measurements are utilized at two wavelengths. One wavelength is selected to be in the Rayleigh scattering regime, i.e., the wavelength is much larger than a typical size of the measured hydrometeors. The other wavelength should be sufficiently beyond the Rayleigh scattering regime, on the order of the hydrometeor size (Matrosov, 1998; Hogan et al., 2000; Liao et al., 2005). In this way with large hydrometeors, the equivalent reflectivity factor of the shorter wavelength is in the resonance regime and falls below that of the longer wavelength. Thus the ratio of the equivalent reflectivity factors provides an estimate of the characteristic hydrometeor size such as median volume diameter D_0 and can be used to constrain the uncertainty in PSD. The difference between the equivalent reflectivity factor values (dB) at the two wavelengths is called Dual Wavelength Ratio (DWR)

$$DWR_{1/2} = Z_{\lambda_1} - Z_{\lambda_2}. \tag{5.24}$$

When λ_1 is selected as the longer wavelength, DWR increases with larger snow particles (Matrosov et al., 2005b). There is an intrinsic lower limit for the retrieved characteristic size; the DWR signature should be higher than a random variance in the reflectivity signals (Hogan et al., 2000). The beam alignment and the calibration of the two radars are important (Hogan et al., 2000; Kulie et al., 2014), and the attenuation at both wavelengths should be small enough to be neglected or then corrected.

As discussed in Section 4.5.6, at higher frequencies the connection be-

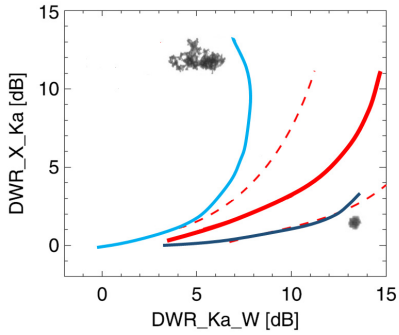

Figure 5.7. Schematic illustration of $DWR_{Ka/W}$ -$DWR_{X/Ka}$ plane reconstructed from images in Publication II. The red solid line describes the averaged spheroidal shapes calculated with T-matrix method, and the red dashed lines are 5% and 95% percentiles from spheroidal shapes assuming an EMA of ice and air with different PSDs, axis ratios, and canting angles from (Leinonen et al., 2012a). The blue lines represent the most extreme curves of large, low-density aggregates (light blue) and heavily rimed particles (dark blue) from the observations in Publication II.

tween microphysical and scattering particle properties is more complex. The methods assuming particles as spheres or spheroids and applying an EMA (soft spheroid models) may not represent the scattering properties with enough accuracy (Liu, 2004; Petty and Huang, 2010; Kulie et al., 2010; Botta et al., 2010, 2011; Tyynelä et al., 2011; Leinonen et al., 2012a; Nowell et al., 2013). Adding one more frequency to the analysis (Triple Wavelength Ratio, TWR), is one way to diagnose the performance of the different snow particle models. This is demonstrated in Kneifel et al. (2011), where the two DWRs between frequencies Ku and Ka and Ka and W for different modeled particles (soft spheres, randomly oriented pristine nonspherical particles, complex aggregates, and horizontally aligned spheroids) are plotted in the $DWR_{Ka/W}$-$DWR_{Ku/Ka}$ plane. This reveals a separation between the results of the complex aggregate models and the spheroidal models; for large low-density aggregates a characteristic “comma” shape in the triple-frequency space can be seen, but this cannot be retrieved with the spheroidal models. A similar feature is also observed in modeling studies (Tyynelä et al., 2014; Leinonen and Moisseev, 2015) and in the observations in (Leinonen et al., 2012a; Kulie et al., 2014) and in Publication II. Leinonen et al. (2012a) estimated that the complex modeling methods are required for snowflakes roughly of the wavelength size. In a modeling study, Leinonen and Moisseev (2015) showed that the different primary crystal habits constituting the aggregates are not significant for

the triple frequency signatures, whereas the size of the habits define the lowest $DWR_{Ka/W}$ value, where the "comma" feature starts deviating from the spheroid models.

In Publication II the ground-based triple-frequency radar observations are investigated with collocated surface measurements (Figure 5.7). In this study, the ground observations verify the comma-shaped feature to appear in the presence of large (> 5 mm) snow aggregates. It is also observed that rimed particles produce an almost horizontal line in the triple-frequency space, and observations indicate a potential of using TWR observations for particle classification.

6. Summary of results

"Passing with relief from the tossing sea of Cause and Theory to the firm ground of Result and Fact."

Sir Winston Churchill, The Story of the Malakand Field Force: An Episode of Frontier War, 1898.

The measuring of winter precipitation is challenging, because of the variability in the properties of snow crystals and snowflakes, which evolve through microphysical processes aloft. Thus the uncertainty in the electromagnetic scattering characteristics and the microphysical parametrization of snow particles propagate to the remote sensing retrievals. The research of this thesis focuses on investigating, how properties of snow particles change through microphysical processes and how these can be connected to the observed changes in remote sensing measurements. Given that observations of the microphysical properties in snowfall change with temporal resolution of minutes, the changes in surface measurements and the retrieved properties are studied in time series.

Two microphysical growth processes, which influence the mass-dimensional ($m(D)$) and fall velocity-dimensional ($v(D)$) relations of snowfall, are aggregation and riming. The contribution of this thesis is to investigate the possible radar signatures of these processes with detailed microphysical retrievals. Typically airborne or ground-based images of snow particles are used qualitatively to validate the remote sensing signatures, whereas measurements of microphysical properties are often determined for a longer time period, and the outcome is an average relation for the whole snowstorm. There are also studies concentrated on retrieving the microphysical properties for rimed or aggregated snow particles without connection to the occurrence of the process and remote sensing measurements. These

studies have acted as validation for snow particle properties of short-time period retrieved here, to indicate that the determined $v(D)$ relations and retrieved $m(D)$ and $Z_e - S$ relations are meaningful.

Retrieval of $m(D)$ relation on short temporal scales

The main ground instrument used in this thesis is the video-disdrometer Particle Imaging Package (PIP). Two methods have been implemented to retrieve automatically ice particle mass-dimensional $m(D)$ relations utilizing co-located PIP and precipitation gauge observations in Publication III and Publication IV. In Publication III, ensemble mean density was derived by combining the measured PSD and determined $v(D)$ relations of PIP with the gauge-measured LWE accumulation. The process seemed to be highly sensitive to the integration time. Therefore, a variable integration time determined by the gauge accumulation was used. The median temporal resolution was 5 minutes and typically between 10^3 and 10^4 particles were observed within this time interval. The same integration time was applied to compute PSD parameters and $v(D)$ relations. The retrieved relation between the ensemble mean snow density and median volume diameter is in general agreement with previous studies and cross-comparison of the retrieved density was performed with snow depth measurements with the good agreement of RMSE of 0.30 cm, the linear correlation coefficient of 0.88 and the normalized bias as low as -0.06. The retrieved ensemble mean snow density in Publication III was utilized in Publication II to show a connection between mean snow density and multi-frequency radar observations and in (Moisseev et al., 2017) together with PSD to quantify the effect of riming on snowfall.

In Publication IV, the $m(D)$ relation was retrieved by utilizing the general hydrodynamic theory, where mass is computed from the observed dimension, fall velocity and area ratio of a snow particle. As all the ground-based disdrometers, PIP observes falling particles from the side, whereas the particle dimensions projected to the flow are needed for the hydrodynamic calculations. To study a ratio between observed and true particle dimensions, the approach similar to (Wood et al., 2013) was adopted. The mean ratios between the true and the observed dimension on single projection were defined by rotating and tilting an ellipsoid with different axis ratios and averaging over different orientations. The errors associated with the observation geometry and the measured particle size distribution

were addressed by devising a simple correction procedure; the value of the correction was chosen for each snow event by comparing the estimated accumulated precipitation to gauge measurements. The $m(D)$ was retrieved for every 5-minutes, as this time period was believed to be short enough to detect changes in the prevailing particle types, but sufficiently long to have enough observations for the reliable retrievals. The obtained relations are corresponding well with the values presented in the literature. The $m(D)$-relations were exploited in Publication IV and Publication V to obtain improved $Z_e - S$-relations for quantitative snowfall estimates.

Connecting properties of snow particles to microphysical processes

In Publication III the dependence of $v(D)$ relation on the ensemble mean density was studied. The particle fall velocity versus diameter data points were divided into three categories according to the snow ensemble mean density of the observed time interval. The prefactor a_v of the power law $v = a_v D^{b_v}$ increased with the density indicating higher fall velocities with more dense particles and also there was a clear increase in the exponent b_v for higher densities. This result is in agreement with the conclusion made by e.g. Barthazy and Schefold (2006).

It was found in Publication III that the median volume diameter D_0 and intercept parameter N_w of gamma PSD are correlated with the ensemble mean density. The density and D_0 are inherently connected, whereas the correlation between N_w and density arises from the observed connection between N_w and D_0 indicating that for heavier precipitation aggregation (> 0.2 mmh^{-1}) is a significant snow growth process.

In Publication IV, it was shown that a transition from one snow growth processes to another, e.g. between aggregation and riming, can be observed in the retrieved $m(D)$ relation, especially in the prefactor a_m, as demonstrated in Figure 6.1. Changes in microphysical properties can also be linked to radar and microwave radiometer observations.

The median values of the prefactors and exponents of $m(D)$ and $v(D)$ relations were computed in three different regions defined by the radiometer-measured LWP to illustrate the changes in values between different particle properties in various processes. The values of LWP can be considered as a proxy for riming. The change from unrimed to rimed particles can be seen as increased values of a_m , whereas the exponent b_m is more or less the same for unrimed and rimed particles, but increases noticeably for

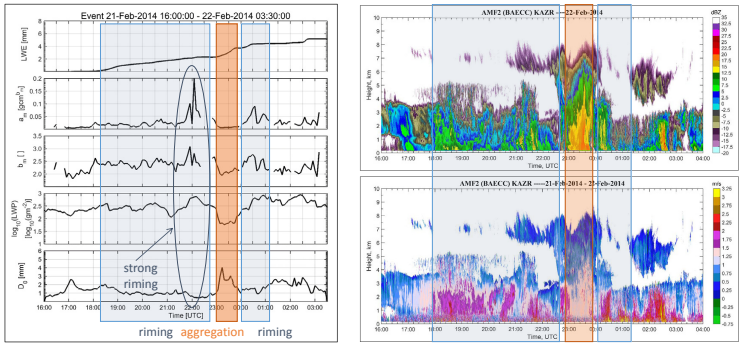

Figure 6.1. An example snowfall event where both riming and aggregation are present. At left: Time series of accumulated LWE retrieved with PIP, factors of $m(D)$ relation, liquid water path LWP measured by two-channel radiometer and median volume diameter of D_0. At right: Vertically profiling Ka-band radar observations show increasing in fall velocities indicating possibly riming process, and the maximum accumulation of the event is between Feb 21 23:00 – Feb 22 00:00 UTC (Publication IV).

graupel. This is in line with the conceptional study of Heymsfield (1982), and aircraft measurements of Erfani and Mitchell (2017). As in Publication III, both prefactor a_v and exponent b_v of $v(D)$ relation increased with riming.

Improved event specific $Z_e - S$ relation for snowfall estimation

In Publication IV and Publication V with the observed PSDs, fitted $v(D)$ and retrieved $m(D)$ relations of PIP and gauge observations, the time-series of the equivalent reflectivity factor Z_e and precipitation rate S were computed. The Rayleigh scattering approximation was utilized as the derived relations were applied for C-band weather radars. For each studied event, a single $Z_e - S$ relation in power-law form was derived by linear regression in log-log scale with the total least-squares method. The event specific prefactor of $Z_e - S$ gained values varied between 39 - 782 mm$^{b_{zs}}$$^{-6}$m^{-3}h^{-1} and the exponent ranged between 1.2-1.6 in the studied events. Using the event-specific relations by applying them to Ikaalinen C-band weather radar (IKA) PPI-scans, the radar-based snowfall estimates were compared with gauge observations and with the FMI operational $Z_e - S$ relation. In general, the event-specific $Z_e - S$ improve the quantitative snowfall estimates compared to the operational relation of FMI, with smaller RMSE of 1.36 mm in respect to 1.96 mm and correlation of 0.80 in respect to 0.54 shown in Publication IV. Although, the event-specific rela-

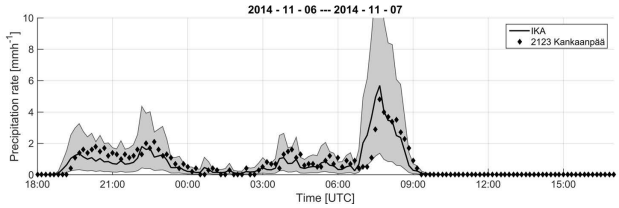

Figure 6.2. Precipitation rate estimated with IKA radar compared to gauge-measured rate for the snowfall event on 6-7 November, 2014 at gauge located at Kankaanpää. With black solid line is shown the radar-estimated precipitation rate utilizing the event-specific factors of $Z_e - S$ relation averaged over 3x3 km area at the precipitation gauge location, the light gray shaded area presents the error limits determined with the upper and lower values of prefactor a_{zs} of the instantaneous $Z_e - S$ relation, and diamonds show the averaged precipitation rate of 10 minutes measured with gauge (Publication V).

tions seemed to overestimate the snowfall rate, the discrepancy between radar-estimated and gauge-measured accumulation can also be explained by the known underestimation of gauges.

In addition to event-specific $Z_e - S$ relation, also analytical instantaneous $Z_e - S$ relations are determined in time series. These were applied in Publication IV to investigate the dependence of $Z_e - S$ relation to microphysical parameters and in Publication V to define the error limits for the event-specific relations. The upper and lower error limits of the prefactor a_{zs} were evaluated from CDF at percentiles of 25% and 75% when the exponent b_{zs} was kept as a mean constant value. An example of the event-specific relation with defined error limits is shown in Figure 6.2. In Publication V a long-term average $Z_e - S$ relation was determined based on 24 snowfall cases during two consecutive winters 2014-2015. This relation can be applied, when detailed ground observations are not available. The relation is at the moment under test for the FMI airport snowfall product.

Dependence of $Z_e - S$ on microphysical parameters

Publication IV investigated with instantaneous $Z_e - S$ relations the dependence of factors on $m(D)$, $v(D)$ and PSD assuming gamma distributed PSD. It was found that the exponent of $Z_e - S$ mainly depends on the exponent of the $m(D)$, but also shape parameter μ of PSD has an influence. However, μ is variable in snowfall and the connection of values to physical changes is not established; therefore exponential distribution is usually assumed for snow (μ = 0). The prefactor a_{zs} is dependent on the intercept parameter

N_0 of PSD and prefactors of the $m(D)$ and $v(D)$ relations. The changes in the prefactors a_m and a_v can be attributed to changes in microphysical processes, such as riming. It was shown that N_0 is the main contributor to the changes in a_{zs}. The role of riming is small but still noticeable. The parametrization expressing a_{zs} as a function N_0 and LWP was also derived. Because of the strong dependence of the prefactor a_{zs} on N_0, the prefactor of an adaptive $Z_e - S$ relation should be determined with measurements of N_0.

Validation of GMI snowfall observations

A method to estimate the snowfall rate from combined measurements of weather radar, video-disdrometer and precipitation gauge was developed in Publication IV and it was utilized for validation of a space-based snowfall product in Publication V. The detection and retrieved surface snowfall precipitation of GMI GPROF - algorithm, versions V04 and V05, were assessed over Southern Finland. The GMI snowfall observations were found to underestimate the surface precipitation, by a factor of 6 with older version V04, and by a factor of 3 with the newer version V05. Based on the 26 studied overpasses, GPROF- algorithm seemed to detect snowfall well, with Probability of Detection of 0.90 for the version V04 and 0.84 for the version V05, and corresponding False Alarm Rates are 0.09 and 0.10 respectively. In Publication V a clear dependence of detection skill on cloud echo top height was shown.

Combined observations of TWR signatures and microphysical properties in snowfall

Radar measurements and modeling studies have shown that naturally occurring snowflakes exhibit scattering signatures that are in some cases consistent with spheroidal particle models and in others can only be explained by complex models of aggregates. Based on ground observations in Publication II the link between the snow microphysics, radar measurements and modeled scattering properties was shown and the potential of triple-frequency radar observations to derive snowfall microphysical properties was demonstrated. On a $DWR_{Ka/W}$-$DWR_{X/Ka}$ plane a typical bending away from the average spheroid line was found to be connected to the presence of larger (> 5 mm) aggregates measured by disdrometer and

signature of riming was observed as a nearly horizontal curve. Riming signatures agree well with DDA scattering computations of graupel particles in (Tyynelä et al., 2014).

Estimating melting layer attenuation at C-band related to snow microphysics

In the case, where melting layer is close to the ground, the weather radar signal with low elevation angle must travel a long distance inside the layer. In Publication I, it was demonstrated that the resulting attenuation of the signal, even at C-band, can be significant, in the order of 7 dB or higher over distance of 40 km. This affects accuracy of radar-based quantitative precipitation estimates. In the study, the specific attenuation of melting layer was investigated as a function of microphysical properties of snow at the top of the melting layer. Based on modeling and fitting $m(D)$ and $v(D)$ relations of snow with vertical pointing radar observations separately for unrimed and rimed snow, two sets of relations between specific attenuation and two-way attenuation as a function of rain rate and reflectivity factor in melting layer were derived. The impact of these relations were demonstrated with a case study.

7. Conclusions

“It’s snowing still," said Eeyore gloomily.

"So it is."

"And freezing."

"Is it?"

"Yes," said Eeyore. "However," he said, brightening up a little, "we haven’t had an earthquake lately.”

A. A. Milne, Winnie the Pooh

Quantified snowfall estimation is important in hydrology, aviation, road maintenance, climate studies and weather services. Remote sensing instrumentation either ground- or space-based can provide the needed spatial coverage and temporal resolution for the environmental monitoring. The challenge in observing winter precipitation remotely stems from the large uncertainty in snowfall microphysical properties i.e. mass, density and size of snow particles, which sets high demands for the retrieval algorithms to describe microphysical properties of snow with adequate accuracy.

The contribution of this thesis is in parameterizing the microphysical properties of falling snow based on surface observations and connecting these to the simultaneous radar observations. The main emphasis is on investigating time series of the properties of snowflakes to understand, how the microphysical processes affect to them. Studying changes in properties with temporal resolution of minutes, the signatures of different growth processes can be observed. In Publication IV changes in properties were linked to aggregation and riming. In (Sinclair et al., 2016), time series were applied to identify secondary ice production process based on observed particle types in right temperature regime, and corresponding signatures in polarimetric radar observations.

The research performed in this thesis ranges between the basic and applied sciences. The final goal is to improve the operational quantitative snowfall estimation, and some of the findings are already applicable for operational use such as the long-term averaged $Z_e - S$ relation defined in Publication V with error limits or the estimation of the expected snow depth from snowfall in Publication III, and some findings are still part of the ongoing research work.

The specific attenuation estimates of melting layer at C-band were presented in Publication I and it was shown that the attenuation is dependent on snow characteristics at the top of the melting layer. In recent years, advances have been taken to retrieve the snow type from polarimetric radar measurements and thus the attenuation estimate could be improved. However, the implemented melting layer model in Publication I was based on single polarization observations and it neglected the aggregation process inside the melting layer. Next steps for improving the model in Publication I is to add stochastic aggregation model and to include shape-properties to scattering calculations.

In this thesis two methods for retrieving $m(D)$ relations, implemented in Publication III and Publication IV, were applied for analyzing all snowfall cases of two winters 2014- 2015 at the University of Helsinki Hyytiälä Forestry Field Station, creating a valuable validation data set for several studies. As an example, based on the ensemble mean density data set gathered in Publication III, Moisseev et al. (2017) constructed a method to retrieve a rime mass fraction from surface-based snowfall measurements. In combination with precipitation rate and accumulation observations, the rime mass fraction is used to quantify the impact of riming on precipitation mass, and in future, the method can be used to validate microphysical parametrization of numerical weather prediction (NWP) models.

In Publication IV based on the retrieved $m(D)$ relations, the dependence of $Z_e - S$ relation on snow microphysics was investigated, and it was shown that the quantitative precipitation snowfall estimation could be improved by using adjustable $Z_e - S$ relation. Given that $Z_e - S$ relation is highly depended on the N_0 parameter of gamma PSD, a method diagnose the N_0 is needed. Unfortunately, there is no established method yet for retrieving this parameter from single-frequency radar measurements. With low precipitation intensity also the prefactor of the $m(D)$ relation can partly explain the different values of the prefactor a_{zs} of $Z_e - S$ relation. Polarimetric radar observables can be applied for identifying the snow type,

and the prefactor a_{zs} could be changed accordingly. Creating an adaptive relation for operational use remains a future challenge.

From the scattering calculations point of view, for weather radar frequencies (S- and C-bands), simple approximations such as Rayleigh or Lorenz-Mie are still valid. However, at frequencies higher than X-band, where the size parameter of larger aggregates or melting particles is close to wavelength size, more complex methods and more detailed shape models are needed. The retrieved masses of snow particles in Publication IV and Publication V connected with their other measured properties such as dimension, area ratio, orientation, and fall velocity can be used as a database for creating complex snowflake models for scattering calculations (Kneifel et al., 2017). Alternatively, the retrieved $m(D)$ relations in Publication IV can be applied for investigating the differences of $Z_e - S$ relations at higher frequencies (Falconi et al., 2017). In Publication II surface observations and the retrieved ensemble mean density in Publication III acted as confirmation for the triple-frequency observation building a link between the TWR signatures and snow microphysics and in Publication V the ground-based snowfall estimates were applied for validating a satellite snowfall algorithm based on multi-frequency radiometer observations. In this way, this thesis is addressing the need for high-quality ground validation data sets for refinement and testing of the retrieval algorithms.

References

Abraham, F. F., 1970: Functional dependence of drag coefficient of a sphere on Reynolds number. *Physics of Fluids*, **13 (8)**, 2194–2195, doi:10.1063/1.1693218.

ADDA, 2017: userguide. https://github.com/adda-team/adda.

Aden, A., and M. Kerker, 1951: Scattering of electromagnetic waves by two concentric spheres. *Journal of Applied Physics*, **22 (10)**, 1242–1246, doi:10.1063/1.1699834.

Atlas, D., R. Srivastava, and R. Sekhon, 1973: Doppler radar characteristics of precipitation at vertical incidence. *Reviews of Geophysics and Space Physics*, **11 (1)**, 1–35, doi:10.1029/RG011i001p00001.

Atlas, D., and C. W. Ulbrich, 1990: *Early Foundations of the Measurement of Rainfall by Radar*. American Meteorological Society, Boston, MA, 806 pp., doi:10.1007/978-1-935704-15-7_12.

Austin, P., and A. Bemis, 1950: A quantitative study of the bright band in radar precipitation echoes. *Journal of Meteorology*, **7 (2)**, 145–151, doi:10.1175/1520-0469(1950)007<0145:AQSOTB>2.0.CO;2.

Aydin, K., and T. Walsh, 1999: Millimeter wave scattering from spatial and planar bullet rosettes. *IEEE Transactions on Geoscience and Remote Sensing*, **37 (2)**, 1138–1150, doi:10.1109/36.752232.

Baran, A. J., 2012: From the single-scattering properties of ice crystals to climate prediction: A way forward. *Atmospheric Research*, **112**, 45 – 69, doi:10.1016/j.atmosres.2012.04.010.

Barthazy, E., S. Göke, R. Schefold, and D. Högl, 2004: An optical array instrument for shape and fall velocity measurements of hydrometeors. *Journal of Atmospheric and Oceanic Technology*, **21**, 1400–1416, doi:10.1175/1520-0426(2004)021<1400:AOAIFS>2.0.CO;2.

Barthazy, E., and R. Schefold, 2006: Fall velocity of snowflakes of different riming degree and crystal types. *Atmospheric Research*, **82 (1-2)**, 391 – 398, doi:10.1016/j.atmosres.2005.12.009.

Battaglia, A., C. Kummerow, D. Shin, and C. Williams, 2003: Constraining microwave brightness temperatures by radar brightband observations. *Journal of the Atmospheric and Oceanic Technology*, **20 (6)**, 856–871, doi:10.1175/1520-0426(2003)020<0856:CMBTBR>2.0.CO;2.

Battaglia, A., E. Rustemeier, A. Tokay, U. Blahak, and C. Simmer, 2010a: PARSIVEL snow observations: A critical assessment. *Journal of Atmospheric and Oceanic Technology*, **27**, 333–344, doi:10.1175/2009JTECHA1332.1.

Battaglia, A., S. Tanelli, S. Kobayashi, D. Zrnić, R. J. Hogan, and C. Simmer, 2010b: Multiple-scattering in radar systems: A review. *Journal of Quantitative Spectroscopy and Radiative Transfer*, **111 (6)**, 917 – 947, doi:https://doi.org/10.1016/j.jqsrt.2009.11.024.

Battan, L., 1973: *Radar Observation of the Atmosphere*. The University of Chicago Press, doi:10.1002/qj.49709942229.

Bauer, P., P. Amayenc, C. D. Kummerow, and E. A. Smith, 2001: Over-ocean rainfall retrieval from multisensor data of the Tropical Rainfall Measuring Mission. Part II: Algorithm implementation. *Journal of Atmospheric and Oceanic Technology*, **18 (11)**, 1838–1855, doi:10.1175/1520-0426(2001)018<1838:OORRFM>2.0.CO;2.

Beard, K., 1976: Terminal velocity and shape of cloud and precipitation drops aloft. *Journal of the Atmospheric Sciences*, **33 (5)**, 851–864, doi:10.1175/1520-0469(1976)033<0851:TVASOC>2.0.CO;2.

Bechini, R., L. Baldini, and V. Chandrasekar, 2013: Polarimetric radar observations in the ice region of precipitating clouds at C-band and X-band radar frequencies. *Journal of Applied Meteorology and Climatology*, **52 (5)**, 1147–1169, doi:10.1175/JAMC-D-12-055.1.

Bennartz, R., and P. Bauer, 2003: Sensitivity of microwave radiances at 85–183 GHz to precipitating ice particles. *Radio Science*, **38 (4)**, doi:10.1029/2002RS002626.

Bernauer, F., K. Hürkamp, W. Rühm, and J. Tschiersch, 2015: On the consistency of 2-D video disdrometers in measuring microphysical parameters of solid precipitation. *Atmospheric Measurement Techniques*, **8 (8)**, 3251–3261, doi:10.5194/amt-8-3251-2015.

Bernauer, F., K. Hürkamp, W. Rühm, and J. Tschiersch, 2016: Snow event classification with a 2D video disdrometer - A decision tree approach. *Atmospheric Research*, **172**, 186–195, doi:10.1016/j.atmosres.2016.01.001.

Berry, M., and I. Percival, 1986: Optics of fractal clusters such as smoke. *Optica Acta: International Journal of Optics*, **33 (5)**, 577–591, doi:10.1080/713821987.

Best, A., 1950: Empirical formulae for the terminal velocity of water drops falling through the atmosphere. *Quarterly Journal of the Royal Meteorological Society*, **76 (329)**, 302–311, doi:10.1002/qj.49707632905.

Böhm, H., 1989: A general equation for the terminal fall speed of solid hydrometeors. *Journal of Atmospheric Sciences*, **46 (15)**, 2419 – 2427, doi:10.1175/1520-0469(1989)046<2419:AGEFTT>2.0.CO;2.

Böhm, J., 1992: A general hydrodynamic theory for mixed-phase microphysics. Part I: Drag and fall speed of hydrometeors. *Atmospheric Research*, **27 (4)**, 253 – 274, doi:10.1016/0169-8095(92)90035-9.

Bohren, C., and L. Battan, 1982: Radar backscattering of microwaves by spongy ice spheres. *Journal of the Atmospheric Sciences*, **39**, 2623–2628.

Bohren, G., and D. Huffman, 1983: *Absorption and scattering of light by small particles*. John Wiley and Sons, USA.

Botta, G., K. Aydin, and J. Verlinde, 2010: Modeling of microwave scattering from cloud ice crystal aggregates and melting aggregates: A new approach. *Geoscience and Remote Sensing Letters, IEEE*, **7 (3)**, 572 –576, doi:10.1109/LGRS.2010.2041633.

Botta, G., K. Aydin, J. Verlinde, A. E. Avramov, A. S. Ackerman, A. M. Fridlind, G. M. McFarquhar, and M. Wolde, 2011: Millimeter wave scattering from ice crystals and their aggregates: Comparing cloud model simulations with X- and Ka-band radar measurements. *Journal of Geophysical Research: Atmospheres*, **116 (D1)**, doi:10.1029/2011JD015909, d00T04.

Brandes, E., K. Ikeda, G. Zhang, M. Schönhuber, and R. Rasmussen, 2007: A statistical and physical description of hydrometeor distributions in Colorado snowstorms using a video disdrometer. *Journal of applied meteorology and climatology*, **46 (5)**, 634 – 650, doi:10.1175/JAM2489.1.

Brandes, E. A., and K. Ikeda, 2004: Freezing-level estimation with polarimetric radar. *Journal of Applied Meteorology*, **43 (11)**, 1541–1553, doi:10.1175/JAM2155.1.

Brandes, E. A., K. Ikeda, G. Thompson, and M. Schönhuber, 2008: Aggregate terminal velocity/temperature relations. *Journal of Applied Meteorology and Climatology*, **47 (10)**, 2729–2736, doi:10.1175/2008JAMC1869.1.

Brandes, E. A., G. Zhang, and J. Vivekanandan, 2002: Experiments in rainfall estimation with a polarimetric radar in a subtropical environment. *Journal of Applied Meteorology*, **41 (6)**, 674–685, doi:10.1175/1520-0450(2002)041<0674:EIREWA>2.0.CO;2.

Bringi, V., and V. Chandrasekar, 2001: *Polarimetric Doppler Weather Radar*. Cambridge University Press, Cambridge.

Bringi, V. N., P. C. Kennedy, G.-J. Huang, C. Kleinkort, M. Thurai, and B. M. Notaroš, 2017: Dual-polarized radar and surface observations of a winter graupel shower with negative Zdr column. *Journal of Applied Meteorology and Climatology*, **56 (2)**, 455–470, doi:10.1175/JAMC-D-16-0197.1.

Brown, P., and P. Francis, 1995: Improved measurements of the ice water content in cirrus using a total-water probe. *Journal of Atmospheric and Oceanic Technology*, **12**, 410 – 414, doi:10.1175/1520-0426(1995)012<0410:IMOTIW>2.0.CO;2.

Bruintjes, R. T., A. J. Heymsfield, and T. W. Krauss, 1987: An examination of double-plate ice crystals and the initiation of precipitation in continental cumulus clouds. *Journal of the Atmospheric Sciences*, **44 (9)**, 1331–1350, doi:10.1175/1520-0469(1987)044<1331:AEODPI>2.0.CO;2.

Bukovcic, P., D. Zrnić, G. Zhang, and A. Ryzhkov, 2015: Snow variability in Oklahoma and Colorado characterized by 2D-video disdrometer and dual-polarization radar measurements. *37th Conference on Radar Meteorology, American Meteorological Society*, 14 - 18 September, Norman, Oklahoma, USA.

Cao, Q., Y. Hong, S. Chen, J. Gourley, J. Zhang, and P. Kirstetter, 2014: Snowfall detectability of NASA's CloudSat: The First cross-investigation of its 2c-Snow-Profile Product and National Multi-Sensor Mosaic QPE (NMQ) snowfall data. **148**, 55–61, doi:10.1002/2013WR014555.

Carlson, P. E., and J. S. Marshall, 1972: Measurement of snowfall by radar. *Journal of Applied Meteorology*, **11 (3)**, 494–500, doi:10.1175/1520-0450(1972)011<0494:MOSBR>2.0.CO;2.

Chandrasekar, V., R. Keränen, S. Lim, and D. Moisseev, 2013: Recent advances in classification of observations from dual polarization weather radars. *Atmospheric Research*, **119**, 97–111, doi:http://doi.org/10.1016/j.atmosres.2011.08.014.

Chen, K., T.-D. Wu, L. Tsang, Q. Li, J. Shi, and A. Fung, 2003: Emission of rough surfaces calculated by the integral equation method with comparison to three-dimensional moment method simulations. *Geoscience and Remote Sensing, IEEE Transactions on*, **41 (1)**, 90–101.

Chen, S., and Coauthors, 2015: Intercomparison of precipitation estimates from WSR-88D radar and TRMM measurement over continental united states. *IEEE Transactions on Geoscience and Remote Sensing*, **53 (8)**, 4444–4456, doi:10.1109/TGRS.2015.2399307.

Chen, S., and Coauthors, 2016: Comparison of snowfall estimates from the NASA CloudSat Cloud Profiling Radar and NOAA/NSSL Multi-Radar Multi-Sensor System. *Journal of Hydrology*, **541, Part B**, 862 – 872, doi:http://dx.doi.org/10.1016/j.jhydrol.2016.07.047.

Cho, H.-R., J. Iribarne, and W. Richards, 1981: On the orientation of ice crystals in a cumulonimbus cloud. *Journal of Atmospheric Sciences*, **38**, 1111–1114, doi:10.1175/1520-0469(1981)038<1111:OTOOIC>2.0.CO;22.

Cotton, R. J., and Coauthors, 2013: The effective density of small ice particles obtained from in situ aircraft observations of mid-latitude cirrus. *Quarterly Journal of the Royal Meteorological Society*, **139 (676)**, 1923–1934, doi:10.1002/qj.2058.

DDSCAT 7.3, 2017: userguide. https://arxiv.org/abs/1305.6497.

de Voe, H., 1964: Optical properties of molecular aggregates. I. Classical model of electronic absorption and refraction. *Journal of Chemical Physics*, **41 (2)**, 393–400, doi:10.1063/1.1725879.

de Voe, H., 1965: Optical properties of molecular aggregates. II. Classical theory of the refraction, absorption and optical activity of solutions and crystals. *Journal of Chemical Physics*, **43 (9)**, 3199–3208, doi:10.1063/1.1697294.

de Wolf, D. A., H. W. J. Russchenberg, and L. P. Ligthart, 1990: Effective permittivity of and scattering from wet snow and ice droplets at weather radar wavelengths. *IEEE Transactions on Antennas and Propagation*, **38 (9)**, 1317–1325, doi:10.1109/8.56981.

Dissanayake, A., J. Allnutt, and F. Haidara, 1997: A prediction model that combines rain attenuation and other propagation impairments along earth-satellite paths. *IEEE Transactions on Antennas and Propagation*, **45 (10)**, 1546–1558, doi:10.1109/8.633864.

Dissanayake, A., and N. McEwan, 1978a: Radar and attenuation properties of rain and bright band. *IEE Conference Publication on Antenna and Propagation*, Vol. 169-2, 161–166.

Doviak, R. J., and D. S. Zrnić, 1993: *Doppler Radar and Weather Observations*. Second edition ed., Academic Press, 562 pp., doi:10.1016/B978-0-12-221422-6.50001-2.

Draine, B., 1988: The discrete-dipole approximation and its application to interstellar graphite grains. *Astrophysical Journal*, **333**, 848–872, doi:10.1086/166795.

Draine, B., and P. Flatau, 1994: Discrete-dipole approximation for scattering calculations. *Journal of Optical Society of America A*, **11 (4)**, 1491–1499, doi:10.1364/JOSAA.11.001491.

Draine, B., and P. Flatau, 2008: Discrete-dipole approximation for periodic targets: Theory and tests. *Journal of Optical Society of America A*, **25 (11)**, 2693–2703, doi:10.1364/JOSAA.25.002693.

Draine, B., and J. Goodman, 1993: Beyond Clausius-Mossotti: Wave propagation on a polarizable point lattice and the discrete dipole approximation. *Astrophysical Journal*, **405 (2)**, 685–697, doi:10.1086/172396.

Drummond, F. J., R. R. Rogers, S. A. Cohn, W. L. Ecklund, D. A. Carter, and J. S. Wilson, 1996: A new look at the melting layer. *Journal of the Atmospheric Sciences*, **53 (5)**, 759–769, doi:10.1175/1520-0469(1996)053<0759:ANLATM>2.0.CO;2.

DuToit, P. S., 1967: Doppler radar observation of drop sizes in continuous rain. *Journal of Applied Meteorology*, **6 (6)**, 1082–1087, doi:10.1175/1520-0450(1967)006<1082:DROODS>2.0.CO;2.

Erfani, E., and D. L. Mitchell, 2016: Developing and bounding ice particle mass- and area-dimension expressions for use in atmospheric models and remote sensing. *Atmospheric Chemistry and Physics*, **16 (7)**, 4379–4400, doi:10.5194/acp-16-4379-2016.

Erfani, E., and D. L. Mitchell, 2017: Growth of ice particle mass and projected area during riming. *Atmospheric Chemistry and Physics*, **17 (2)**, 1241–1257, doi:10.5194/acp-17-1241-2017.

Evans, K., and G. Stephens, 1995a: Microwave radiative transfer through clouds composed of realistically shaped ice crystals. Part I: Single scattering properties. *Journal of the Atmospheric Sciences*, **52 (11)**, 2041–2057, doi:10.1175/1520-0469(1995)052<2041:MRTTCC>2.0.CO;2.

Evans, K., and G. Stephens, 1995b: Microwave radiative transfer through clouds composed of realistically shaped ice crystals. Part II: Remote sensing of ice clouds. *Journal of the Atmospheric Sciences*, **52 (11)**, 2058–2072, doi:10.1175/1520-0469(1995)052<2058:MRTTCC>2.0.CO;2.

Fabry, F., and W. Szyrmer, 1999: Modeling of the melting layer. Part II: Electromagnetic. *Journal of the Atmospheric Sciences*, **56 (26)**, 3593–3600, doi:10.1175/1520-0469(1999)056<3593:MOTMLP>2.0.CO;2.

Fabry, F., and I. Zawadzki, 1995: Long-term radar observations of the melting layer of precipitation and their interpretation. *Journal of the Atmospheric Sciences*, **52 (7)**, 838–851, doi:10.1175/1520-0469(1995)052<0838:LTROOT>2.0.CO;2.

Falconi, M., , A. von Lerber, D. Ori, F. S. Marzano, and D. Moisseev, 2017: Snowfall retrievals at X/Ka/W-band: Consistency between scattering and microphysical properties of snow using ground-based data from BAECC. *Atmospheric Measurement Techniques*, under preparation.

Ferraro, R. R., and Coauthors, 2005: NOAA operational hydrological products derived from the advanced microwave sounding unit. *IEEE Transactions on Geoscience and Remote Sensing*, **43 (5)**, 1036–1049, doi:10.1109/TGRS.2004.843249.

Field, P. R., 1999: Aircraft observations of ice crystal evolution in an altostratus cloud. *Journal of the Atmospheric Sciences*, **56 (12)**, 1925–1941, doi:10.1175/1520-0469(1999)056<1925:AOOICE>2.0.CO;2.

Field, P. R., and A. J. Heymsfield, 2015: Importance of snow to global precipitation. *Geophysical Research Letters*, **42 (21)**, 9512–9520, doi:10.1002/2015GL065497.

Field, P. R., A. J. Heymsfield, A. Bansemer, and C. H. Twohy, 2008: Determination of the combined ventilation factor and capacitance for ice crystal aggregates from airborne observations in a tropical anvil cloud. *Journal of the Atmospheric Sciences*, **65 (2)**, 376–391, doi:10.1175/2007JAS2391.1.

Field, P. R., and Coauthors, 2017: Secondary ice production: Current state of the science and recommendations for the future. *Meteorological Monographs*, **58**, 7.1–7.20, doi:10.1175/AMSMONOGRAPHS-D-16-0014.1.

Foote, G. B., and P. S. D. Toit, 1969: Terminal velocity of raindrops aloft. *Journal of Applied Meteorology*, **8 (2)**, 249–253, doi:10.1175/1520-0450(1969)008<0249:TVORA>2.0.CO;2.

Foster, J., J. Barton, A. Chang, and D. Hall, 2000: Snow crystal orientation effects on the scattering of passive microwave radiation. *IEEE Transactions on Geoscience and Remote Sensing*, **38 (5)**, 2430–2434, doi:10.1109/36.868899.

Foster, J., D. Hall, A. Chang, A. Rango, W. Wergin, and E. Erbe, 1999: Effects of snow crystal shape on the scattering of passive microwave radiation. *IEEE Transactions on Geoscience and Remote Sensing*, **37 (2)**, 1165–1168.

Foster, J. L., and Coauthors, 2012: Passive microwave remote sensing of the historic February 2010 snowstorms in the Middle Atlantic region of the USA. *Hydrological Processes*, **26 (22)**, 3459–3471, doi:10.1002/hyp.8418.

Frasier, S. J., F. Kabeche, J. F. i Ventura, H. Al-Sakka, P. Tabary, J. Beck, and O. Bousquet, 2013: In-place estimation of wet radome attenuation at X band. *Journal of Atmospheric and Oceanic Technology*, **30 (5)**, 917–928, doi:10.1175/JTECH-D-12-00148.1.

Fujiyoshi, Y., 1986: Melting snowflakes. *Journal of the Atmospheric Sciences*, **43 (3)**, 307–311, doi:10.1175/1520-0469(1986)043<0307:MS>2.0.CO;2.

Fujiyoshi, Y., T. Endoh, T. Yamada, K. Tsuboki, Y. Tachibana, and G. Wakahama, 1990: Determination of a Z-R relationship for snowfall using a radar and high sensitivity snow gauges. *Journal of Applied Meteorology*, **29 (2)**, 147–152, doi:10.1175/1520-0450(1990)029<0147:DOARFS>2.0.CO;2.

Fung, A., 1994: *Microwave Scattering and Emission Models and Their Applications*. Artech House, USA.

Garrett, T., C. Fallgatter, K. Shkurko, and D. Howlett, 2012: Fall speed measurement and high-resolution multi-angle photography of hydrometeors in free fall. *Atmospheric Measurement Techniques*, **5**, 2625 – 2633, doi: 10.5194/amt-5-2625-2012.

Garrett, T., and S. Yuter, 2014: Observed influence of riming, temperature, and turbulence on the fallspeed of solid precipitation. *Geophysical Research Letters*, **41 (18)**, 6515–6522, doi:10.1002/2014GL061016.

Garrett, T. J., S. E. Yuter, C. Fallgatter, K. Shkurko, S. Rhodes, and J. L. Endries, 2015: Orientations and aspect ratios of falling snow. *Geophysical Research Letters*, **42 (11)**, 4617–4622, doi:10.1002/2015GL064040.

Gavrilov, S., and Coauthors, 2015: Feature analysis and classification of particle data from two-dimensional video disdrometer. *Advances in Remote Sensing*, **4**, 1–14, doi:10.4236/ars.2015.41001.

Giangrande, S. E., 2007: Investigation of polarimetric measurements of rainfall at close and distant ranges. Ph.D. thesis, University of Oklahoma.

Giangrande, S. E., J. M. Krause, and A. V. Ryzhkov, 2008: Automatic designation of the melting layer with a polarimetric prototype of the WSR-88D radar. *Journal of Applied Meteorology and Climatology*, **47 (5)**, 1354–1364, doi:10.1175/2007JAMC1634.1.

Goedecke, G., and S. O'Brien, 1988: Scattering by irregular inhomogeneous particles via the digitized Green's function algorithm. *Applied Optics*, **27 (12)**, 2431–2438, doi:10.1364/AO.27.002431.

Göke, S., 1999: Microphysics of the melting layer. Ph.D. thesis, ETH Zürich, Switzerland, 158 pp., 10.3929/ethz-a-003906768.

Goodison, B., P. Louie, and D. Yang, 1998: WMO solid precipitation measurement intercomparison final report. Tech. Rep. WMO/TD No.872, IOM No. 67, 212 pp.

Goodison, B., P. Louie, and D. Yang, 2014: WMO guide to meteorological instruments and methods of observation. Tech. Rep. WMO-No. 8, 1139 pp.

Gray, D., and D. Male, 1981: *Handbook of snow*. Pergamon Press.

Grazioli, J., D. Tuia, and A. Berne, 2015: Hydrometeor classification from polarimetric radar measurements: a clustering approach. *Atmospheric Measurement Techniques*, **8 (1)**, 149–170, doi:10.5194/amt-8-149-2015.

Grazioli, J., D. Tuia, S. Monhart, M. Schneebeli, T. Raupach, and A. Berne, 2014: Hydrometeor classification from two-dimensional video disdrometer data. *Atmospheric Measurement Techniques*, **7 (9)**, 2869–2882, doi:10.5194/amt-7-2869-2014.

Gunn, R., and G. D. Kinzer, 1949: The terminal velocity of fall for water droplets in stagnant air. *Journal of Meteorology*, **6 (4)**, 243–248, doi:10.1175/1520-0469(1949)006<0243:TTVOFF>2.0.CO;2.

Hage, J., J. Greenberg, and R. Wang, 1991: Scattering from arbitrarily shaped particles: Theory and experiment. *Applied Optics*, **30 (9)**, 1141–1152, doi:10.1364/AO.30.001141.

Hallett, J., and S. C. Mossop, 1974: Production of secondary ice particles during the riming process. *Nature*, **249**, 26–28, doi:10.1038/249026a0.

Hanesch, M., 1999: Fall Velocity and shape of snowflakes. Ph.D. thesis, ETH Zürich, Switzerland, 10.3929/ethz-a-003837623.

Hardaker, P. J., A. R. Holt, and C. G. Collier, 1995: A melting-layer model and its use in correcting for the bright band in single-polarization radar echoes. *Quarterly Journal of the Royal Meteorological Society*, **121 (523)**, 495–525, doi:10.1002/qj.49712152303.

Harimaya, T., 1975: The riming properties of snow crystals. *Journal of the Meteorological Society of Japan. Series II*, **53 (6)**, 384–392, doi:10.2151/jmsj1965.53.6_384.

Harimaya, T., and M. Sato, 1989: Measurement of the riming amount on snowflakes. *J. Fac. Sci., Hokkaido Univ. Ser.VII*, **8 (4)**, 355–366.

Heymsfield, A., 1982: A comparative study of the rates of development of potential graupel and hail embryos in high plains storms. *Journal of Atmospheric Sciences*, **39 (12)**, 2867–2897, doi:10.1175/1520-0469(1982)039<2867:ACSOTR>2.0.CO;2.

Heymsfield, A., and M. Kajikawa, 1987: An improved approach to calculating terminal velocities of plate-like crystals and graupel. *Journal of the Atmospheric Sciences*, **44 (7)**, 1088–1099, doi:10.1175/1520-0469(1987)044<1088:AIATCT>2.0.CO;2.

Heymsfield, A., S. Lewis, A. Bansemer, J. Iaquinta, L. Miloshevich, M. Kajikawa, C. Twohy, and M. Poellot, 2002: A general approach for deriving the properties of cirrus and stratiform ice cloud particles. *Journal of Atmospheric Sciences*, **59 (1)**, 3–29, doi:10.1175/1520-0469(2002)059<0003:AGAFDT>2.0.CO;2.

Heymsfield, A., and C. Westbrook, 2010: Advances in the estimation of ice particle fall speeds using laboratory and field measurements. *Journal of Atmospheric Sciences*, **67 (8)**, 2469–2482, doi:10.1175/2010JAS3379.1.

Heymsfield, A. J., A. Bansemer, M. R. Poellot, and N. Wood, 2015: Observations of ice microphysics through the melting layer. *Journal of the Atmospheric Sciences*, **72 (8)**, 2902–2928, doi:10.1175/JAS-D-14-0363.1.

Heymsfield, A. J., A. Bansemer, C. Schmitt, C. Twohy, and M. Poellot, 2004: Effective ice particle densities derived from aircraft data. *Journal of the Atmospheric Sciences*, **61 (9)**, 982–1003, doi:10.1175/1520-0469(2004)061<0982:EIPDDF>2.0.CO;2.

Heymsfield, A. J., A. Bansemer, and C. H. Twohy, 2007: Refinements to ice particle mass dimensional and terminal velocity relationships for ice clouds. Part I: Temperature dependence. *Journal of the Atmospheric Sciences*, **64 (4)**, 1047–1067, doi:10.1175/JAS3890.1.

Heymsfield, A. J., C. Schmitt, A. Bansemer, and C. H. Twohy, 2010: Improved representation of ice particle masses based on observations in natural clouds. *Journal of the Atmospheric Sciences*, **67 (10)**, 3303–3318, doi: 10.1175/2010JAS3507.1.

Hiley, M. J., M. S. Kulie, and R. Bennartz, 2011: Uncertainty analysis for CloudSat snowfall retrievals. *Journal of Applied Meteorology and Climatology*, **50 (2)**, 399–418, doi:10.1175/2010JAMC2505.1.

Hogan, R., P. Francis, H. Flentje, A. J. Illingworth, M. Quante, and J. Pelon, 2003: Characteristics of mixed-phase clouds. I: Lidar, radar and aircraft observations from CLARE'98. *Quarterly Journal of the Royal Meteorological Society*, **129 (592)**, 2089–2116, doi:10.1256/rj.01.208.

Hogan, R. J., R. Honeyager, J. Tyynelä, and S. Kneifel, 2017: Calculating the millimetre-wave scattering phase function of snowflakes using the self-similar Rayleigh–Gans Approximation. *Quarterly Journal of the Royal Meteorological Society*, **143 (703)**, 834–844, doi:10.1002/qj.2968.

Hogan, R. J., A. J. Illingworth, and H. Sauvageot, 2000: Measuring crystal size in cirrus using 35- and 94-GHz radars. *Journal of Atmospheric and Oceanic Technology*, **17 (1)**, 27–37, doi:10.1175/1520-0426(2000)017<0027:MCSICU>2.0.CO;2.

Hogan, R. J., and C. D. Westbrook, 2014: Equation for the microwave backscatter cross section of aggregate snowflakes using the self-similar Rayleigh–Gans Approximation. *Journal of the Atmospheric Sciences*, **71 (9)**, 3292–3301, doi: 10.1175/JAS-D-13-0347.1.

Hoose, C., and O. Möhler, 2012: Heterogeneous ice nucleation on atmospheric aerosols: A review of results from laboratory experiments. *Atmospheric Chemistry and Physics*, **12 (20)**, 9817–9854, doi:10.5194/acp-12-9817-2012.

Hou, A. Y., and Coauthors, 2014: The Global Precipitation Measurement Mission. *Bulletin of the American Meteorological Society*, **95 (5)**, 701–722, doi:10.1175/BAMS-D-13-00164.1.

Huang, G.-J., V. N. Bringi, R. Cifelli, D. Hudak, and W. A. Petersen, 2010: A methodology to derive radar reflectivity - liquid equivalent snow rate relations using C - band radar and a 2D - video disdrometer. *Journal of Atmospheric and Oceanic Technology*, **27 (4)**, 637–651, doi:10.1175/2009JTECHA1284.1.

Huang, G.-J., V. N. Bringi, D. Moisseev, W. A. Petersen, L. Bliven, and D. Hudak, 2015: Use of 2D - video disdrometer to derive mean density - size and Ze - SR relations: Four snow cases from the Light Precipitation Validation EXperiment. *Atmospheric Research*, **153**, 34–48, doi:10.1016/j.atmosres.2014.07.013.

Hudak, D., P. Rodriguez, and N. Donaldson, 2008: Validation of the CloudSat precipitation occurrence algorithm using the Canadian C band radar network. *Journal of Geophysical Research: Atmospheres*, **113 (D8)**, doi: 10.1029/2008JD009992, d00A07.

Hufford, G., 1991: A model for the complex permittivity of ice at frequencies below 1 THz. *International Journal of Infrared and Millimeter Waves*, **12 (7)**, 677–682, doi:10.1007/BF01008898.

Iguchi, T., and Coauthors, 2012: Numerical analysis using WRF-SBM for the cloud microphysical structures in the C3VP field campaign: Impacts of supercooled droplets and resultant riming on snow microphysics. *Journal of Geophysical Research: Atmospheres*, **117 (D23)**, doi:10.1029/2012JD018101, d23206.

Imai, I., 1960: Raindrop size distribution and the Z-R relationship. *Eighth Weather AMS Radar Conference*, Boston, USA, 321–326.

Ishimaru, A., 1978: *Wave Propagation and Scattering in Random Media vols. I-II*. Academic Press, New York.

Ishimoto, H., 2008: Radar backscattering computations for fractal-shaped snowflakes. *Journal of the Meteorological Society of Japan. Ser. II*, **86 (3)**, 459–469, doi:10.2151/jmsj.86.459.

ITU-R Recommendation, P.676-10, 2013: Attenuation by atmospheric gases. Radiocommunication Sector of International Telecommunication Union, Geneve.

Jensen, A. A., and J. Y. Harrington, 2015: Modeling ice crystal aspect ratio evolution during riming: A single-particle growth model. *Journal of the Atmospheric Sciences*, **72 (7)**, 2569–2590, doi:10.1175/JAS-D-14-0297.1.

Jiang, J. H., and D. L. Wu, 2004: Ice and water permittivities for millimeter and sub-millimeter remote sensing applications. *Atmospheric Science Letters*, **5 (7)**, 146–151, doi:10.1002/asl.77.

Jiusto, J. E., and G. E. Bosworth, 1971: Fall velocity of snowflakes. *Journal of Applied Meteorology*, **10 (6)**, 1352–1354, doi:10.1175/1520-0450(1971)010<1352:FVOS>2.0.CO;2.

Jiusto, J. E., and H. K. Weickmann, 1973: Types of snowfall. *Bulletin of the American Meteorological Society*, **54 (11)**, 1148–1162, doi:10.1175/1520-0477(1973)054<1148:TOS>2.0.CO;2.

Joe, P., and P. Smith, 2001: Summary of the radar calibration workshop. *30th International Conference on Radar Meteorology*, Münich, Germany, 174–176.

Johnson, B., W. Olson, and G. Skofronick-Jackson, 2016: The microwave properties of simulated melting precipitation particles: Sensitivity to initial melting. *Atmospheric Measurement Techniques*, **9 (1)**, 9–21, doi:10.5194/amt-9-9-2016.

Joss, J., and A. Waldvogel, 1967: A raindrop spectograph with automatic analysis (Ein Spektrograph für Niederschlagstropfen mit automatischer Auswertung). *Pure and Applied Geophysics*, **68 (1)**, 240–246, doi:doi:10.1007/BF00874898.

JSCAT, 2017: userguide. https://scattport.org/index.php/programs-menu/volume-integral-menu/51-jscat.

Kahnert, F., 2003: Numerical methods in electromagnetic scattering theory. *Journal of Quantative Spectroscopy & Radiative Transfer*, **79-80**, 775–824.

Kaikkonen, V., D. Ekimov, and A. Mäkynen, 2014: A holographic in-line imaging system for meteorological applications. *IEEE Transactions on Instrumentation and Measurement*, **63 (5)**, 1137–1144, doi:10.1109/TIM.2013.2295658.

Kaikkonen, V. A., and A. J. Mäkynen, 2016: A high sampling rate digital holographic imager instrument for the in situ measurements of hydrometeors. *Optical Review*, **23 (3)**, 493–501, doi:10.1007/s10043-016-0182-1.

Kajikawa, M., 1972: Measurement of falling velocity of individual snow crystals. *Journal of the Meteorological Society of Japan*, **50 (6)**, 276–283, doi:10.2151/jmsj1965.50.6_577.

Kajikawa, M., 1974: On the collection efficiency of snow crystals for cloud droplets. *Journal of the Meteorological Society of Japan. Series II*, **52 (3)**, 328–336, doi:10.2151/jmsj1965.52.3_328.

Kajikawa, M., 1989: Observation of the falling motion of early snow flakes. *Journal of the Meteorological Society of Japan. Ser. II*, **67 (5)**, 731–738.

Kennedy, P., and S. Rutledge, 2011: S-band dual-polarization radar observations of winter storms. *Journal of Applied Meteorology and Climatology*, **50 (4)**, 844–858, doi:10.1175/2010JAMC2558.1.

Khvorostyanov, V., and J. A. Curry, 2002: Terminal velocities of droplets and crystals: Power laws with continuous parameters over the size spectrum. *Journal of Atmospheric Sciences*, **59 (11)**, 1872 – 1884, doi:10.1175/1520-0469(2002)059<1872:TVODAC>2.0.CO;2.

Khvorostyanov, V., and J. A. Curry, 2005: Fall velocities of hydrometeors in the atmosphere: Refinements to a continuous analytical power law. *Journal of Atmospheric Sciences*, **62 (12)**, 4343–4357, doi:10.1175/JAS3622.1.

Kidd, C., and G. Huffman, 2011: Global precipitation measurement. *Meteorological Applications*, **18 (3)**, 334–353, doi:10.1002/met.284.

Kidd, C., and V. Levizzani, 2011: Status of satellite precipitation retrievals. *Hydrology and Earth System Sciences*, **15 (4)**, 1109–1116, doi:10.5194/hess-15-1109-2011.

Kim, M.-J., 2006: Single scattering parameters of randomly oriented snow particles at microwave frequencies. *Journal of Geophysical Research: Atmospheres*, **111 (D14)**, doi:10.1029/2005JD006892, d14201.

Kim, M.-J., J. A. Weinman, W. S. Olson, D.-E. Chang, G. Skofronick-Jackson, and J. R. Wang, 2008: A physical model to estimate snowfall over land using AMSU-B observations. *Journal of Geophysical Research: Atmospheres*, **113 (D9)**, doi:10.1029/2007JD008589, d09201.

Klaassen, W., 1988: Radar observations and simulation of the melting layer of precipitation. *Journal of the Atmospheric Sciences*, **45 (24)**, 3741–3753, doi:10.1175/1520-0469(1988)045<3741:ROASOT>2.0.CO;2.

Klaassen, W., 1990: Attenuation and reflection of radio waves by a melting layer of precipitation. *IEE Proceedings H on Microwaves, Antennas and Propagation*, **137 (1)**, 39 – 44.

Kneifel, S., M. S. Kulie, and R. Bennartz, 2011: A triple-frequency approach to retrieve microphysical snowfall parameters. *Journal of Geophysical Research: Atmospheres*, **116 (D11)**, doi:10.1029/2010JD015430.

Kneifel, S., and Coauthors, 2017: The First International Summer Snowfall Workshop: Scattering properties of realistic frozen hydrometeors from simulations and observations, as well as defining a new standard for scattering databases. *Bulletin of the American Meteorological Society*, doi:10.1175/BAMS-D-17-0208.1.

Knight, C. A., 1979: Observations of the morphology of melting snow. *Journal of the Atmospheric Sciences*, **36 (6)**, 1123–1130, doi:10.1175/1520-0469(1979)036<1123:OOTMOM>2.0.CO;2.

Koistinen, J., and D. Michelson, 2002: BALTEX weather radar-based precipitation products and their accuracies. *Boreal Environment Research*, **7**, 253–263.

Koistinen, J., and H. Pohjola, 2014: Estimation of ground-level reflectivity factor in operational weather radar networks using VPR-based correction ensembles. *Journal of Applied Meteorology and Climatology*, **53 (10)**, 2394–2411, doi:10.1175/JAMC-D-13-0343.1.

Kongoli, C., H. Meng, J. Dong, and R. Ferraro, 2015: A snowfall detection algorithm over land utilizing high-frequency passive microwave measurements—application to ATMS. *Journal of Geophysical Research: Atmospheres*, **120 (5)**, 1918–1932, doi:10.1002/2014JD022427, 2014JD022427.

Kongoli, C., P. Pellegrino, R. R. Ferraro, N. C. Grody, and H. Meng, 2003: A new snowfall detection algorithm over land using measurements from the Advanced Microwave Sounding Unit (AMSU). *Geophysical Research Letters*, **30 (14)**, doi:10.1029/2003GL017177.

Koop, T., B. Luo, A. Tsias, and T. Peter, 2000: Water activity as the determinant for homogeneous ice nucleation in aqueous solutions. *Nature*, **406**, 611–614, doi:10.1038/35020537.

Kruger, A., and W. Krajewski, 2002: Two-dimensional video disdrometer: A description. *Journal of Atmospheric and Oceanic Technology*, **19 (5)**, 602–617, doi:10.1175/1520-0426(2002)019<0602:TDVDAD>2.0.CO;2.

Kulie, M. S., and R. Bennartz, 2009: Utilizing spaceborne radars to retrieve dry snowfall. *Journal of Applied Meteorology and Climatology*, **48 (12)**, 2564–2580, doi:10.1175/2009JAMC2193.1.

Kulie, M. S., R. Bennartz, T. J. Greenwald, Y. Chen, and F. Weng, 2010: Uncertainties in microwave properties of frozen precipitation: Implications for remote sensing and data assimilation. *Journal of the Atmospheric Sciences*, **67 (11)**, 3471–3487, doi:10.1175/2010JAS3520.1.

Kulie, M. S., M. J. Hiley, R. Bennartz, S. Kneifel, and S. Tanelli, 2014: Triple-frequency radar reflectivity signatures of snow: Observations and comparisons with theoretical ice particle scattering models. *Journal of Applied Meteorology and Climatology*, **53 (4)**, 1080–1098, doi:10.1175/JAMC-D-13-066.1.

Kumar, L. S., Y. H. Lee, and J. T. Ong, 2011: Two-parameter gamma drop size distribution models for Singapore. *IEEE Transactions on Geoscience and Remote Sensing*, **49 (9)**, 3371–3380, doi:10.1109/TGRS.2011.2124464.

Kummerow, C., W. Berg, J. Thomas-Stahle, and H. Masunaga, 2006: Quantifying global uncertainties in a simple microwave rainfall algorithm. *Journal of Atmospheric and Oceanic Technology*, **23 (1)**, 23–37, doi:10.1175/JTECH1827.1.

Kummerow, C. D., D. L. Randel, M. Kulie, N.-Y. Wang, R. Ferraro, S. J. Munchak, and V. Petkovic, 2015: The evolution of the goddard profiling algorithm to a fully parametric scheme. *Journal of Atmospheric and Oceanic Technology*, **32 (12)**, 2265–2280, doi:10.1175/JTECH-D-15-0039.1.

Kummerow, C. D., S. Ringerud, J. Crook, D. Randel, and W. Berg, 2011: An observationally generated a priori database for microwave rainfall retrievals. *Journal of Atmospheric and Oceanic Technology*, **28 (2)**, 113–130, doi:10.1175/2010JTECHA1468.1.

Kuo, K.-S., and Coauthors, 2016: The microwave radiative properties of falling snow derived from nonspherical ice particle models. Part I: An extensive database of simulated pristine crystals and aggregate particles, and their scattering properties. *Journal of Applied Meteorology and Climatology*, **55 (3)**, 691–708, doi:10.1175/JAMC-D-15-0130.1.

Kurri, M., and A. Huuskonen, 2008: Measurements of the transmission loss of a radome at different rain intensities. *Journal of Atmospheric and Oceanic Technology*, **25 (9)**, 1590–1599, doi:10.1175/2008JTECHA1056.1.

Lakhtakia, A., and G. Mulholland, 1993: On two numerical techniques for light scattering by dielectric agglomerated structures. *Journal of Research of the National Institute of Standards and Technology*, **98 (6)**, 699–716, doi:10.6028/jres.098.046.

Lamb, D., and J. Verlinde, 2011: *Physics and Chemistry of Clouds*. Cambridge University Press, doi:10.1017/CBO9780511976377.

Langille, R. C., and R. S. Thain, 1951: Some quantitative measurements of three-centimeter radar echoes from falling snow. *Canadian Journal of Physics*, **29 (6)**, 482–490, doi:10.1139/p51-052.

Langleben, M. P., 1954: The terminal velocity of snowflakes. *Quarterly Journal of the Royal Meteorological Society*, **80 (346)**, 640–642, doi:10.1002/qj.49708034619.

Lawson, R. P., S. Woods, and H. Morrison, 2015: The microphysics of ice and precipitation development in tropical cumulus clouds. *Journal of the Atmospheric Sciences*, **72 (6)**, 2429–2445, doi:10.1175/JAS-D-14-0274.1.

Lee, J.-E., S.-H. Jung, H.-M. Park, S. Kwon, P.-L. Lin, and G.-W. Lee, 2015: Classification of precipitation types using fall velocity-diameter relationships from 2D-video distrometer measurements. *Advances in Atmospheric Sciences*, **32 (9)**, 1277–1290, doi:10.1007/s00376-015-4234-4.

Leinonen, J., S. Kneifel, D. Moisseev, J. Tyynelä, S. Tanelli, and T. Nousiainen, 2012a: Evidence of non-spheroidal behavior in millimeter-wavelength radar observations of snowfall. *Journal of Geophysical Research: Atmospheres*, **117 (D18)**, doi:10.1029/2012JD017680, d18205.

Leinonen, J., and D. Moisseev, 2015: What do triple-frequency radar signatures reveal about aggregate snowflakes? *Journal of Geophysical Research: Atmospheres*, **120 (1)**, 229–239, doi:10.1002/2014JD022072.

Leinonen, J., D. Moisseev, V. Chandrasekar, and J. Koskinen, 2011: Mapping radar reflectivity values of snowfall between frequency bands. *IEEE Transactions on Geoscience and Remote Sensing*, **49 (8)**, 3047–3058, doi:10.1109/TGRS.2011.2117432.

Leinonen, J., D. Moisseev, M. Leskinen, and W. Petersen, 2012b: A climatology of five-year disdrometer observations of rainfall in Finland with implications

for global radar observations. *Journal of Applied Meteorology and Climatology*, **51 (2)**, 392–404, doi:10.1175/JAMC-D-11-056.1.

Leinonen, J., D. Moisseev, and T. Nousiainen, 2013: Linking snowflake microstructure to multi-frequency radar observations. *Journal of Geophysical Research: Atmospheres*, **118 (8)**, 3259–3270, doi:10.1002/jgrd.50163.

Leinonen, J., and A. von Lerber, 2017: Snowflake melting simulation using smoothed particle hydrodynamics. *Journal of Geophysical Research*, under preparation.

Leitao, M., and P. Watson, 1986: Method for prediction of attenuation on earth-space links based on radar measurements of the physical structure of rainfall. *Communications, Radar and Signal Processing, IEE Proceedings F*, **133 (4)**, 429 –440.

Liao, L., R. Meneghini, T. Iguchi, and A. Detwiler, 2005: Use of dual-wavelength radar for snow parameter estimates. *Journal of Atmospheric and Oceanic Technology*, **22 (10)**, 1494–1506, doi:10.1175/JTECH1808.1.

Libbrecht, K. G., 2005: The physics of snow crystals. *Reports on Progress in Physics*, **68 (4)**, 855, doi:10.1088/0034-4885/68/4/R03.

Liebe, H. J., G. A. Hufford, and T. Manabe, 1991: A model for the complex permittivity of water at frequencies below 1 THz. *International Journal of Infrared and Millimeter Waves*, **12 (7)**, 659–675, doi:10.1007/BF01008897.

List, R., and R. Schemenauer, 1971: Free-fall behavior of planar snow crystals, conical graupel and small hail. *Journal of the Atmospheric Sciences*, **28**, 110–115, doi:10.1175/1520-0469(1971)028<0110:FFBOPS>2.0.CO;2.

Liu, G., 2004: Approximation of single scattering properties of ice and snow particles for high microwave frequencies. *Journal of the Atmospheric Sciences*, **61**, 2441 – 2456, doi:10.1175/1520-0469(2004)061<2441:AOSSPO>2.0.CO;2.

Liu, G., 2008: Deriving snow cloud characteristics from CloudSat observations. *Journal of Geophysical Research: Atmospheres*, **113 (D8)**, doi:10.1029/2007JD009766, d00A09.

Liu, G., and E.-K. Seo, 2013: Detecting snowfall over land by satellite high-frequency microwave observations: The lack of scattering signature and a statistical approach. *Journal of Geophysical Research: Atmospheres*, **118 (3)**, 1376–1387, doi:10.1002/jgrd.50172.

Locatelli, J., and P. Hobbs, 1974: Fall speeds and masses of solid precipitation particles. *Journal of Geophysical Research*, **79 (15)**, 2185–2197, doi:10.1029/JC079i015p02185.

Löffler-Mang, M., and U. Blahak, 2001: Estimation of the equivalent radar reflectivity factor from measured snow size spectra. *J. Appl. Meteor.*, **40**, 843–849, doi:{10.1175/1520-0450(2001)040<0843;EOTERR>2.0.CO;2}.

Löffler-Mang, M., and J. Joss, 2000: An optical disdrometer for measuring size and velocity of hydrometeors. *Journal of Atmospheric and Oceanic Technology*, **17**, 130–139, doi:{10.1175/1520-0426(2000)017<0130;AODFMS>2.0.CO;2}.

Logvin, A. I., L. P. Ligthart, and A. I. Kozlov, 2002: Methods for solving inverse problems in radar remote sensing. *14th International Conference on Microwaves, Radar and Wireless Communications. MIKON - 2002. Conference Proceedings (IEEE Cat.No.02EX562)*, Vol. 2, 681–685 vol.2, doi:10.1109/MIKON.2002.1017936.

Lorenz, L., 1890: Lysbevægelsen i og uden for en af plane lysbølger belyst kugle. *Det Kongelige Danske Videnskabernes Selskabs Skrifter*, **1**, 1–62.

Lu, Y., E. E. Clothiaux, K. Aydin, G. Botta, and J. Verlinde, 2013: Modeling variability in dendritic ice crystal backscattering cross sections at millimeter wavelengths using a modified Rayleigh–Gans theory. *Journal of Quantitative Spectroscopy and Radiative Transfer*, **131**, 95 – 104, doi:https://doi.org/10.1016/j.jqsrt.2013.05.008.

Lu, Y., E. E. Clothiaux, K. Aydin, and J. Verlinde, 2014: Estimating ice particle scattering properties using a modified Rayleigh-Gans approximation. *Journal of Geophysical Research: Atmospheres*, **119 (17)**, 10 471–10 484, doi:10.1002/2014JD021850, 2014JD021850.

Lu, Y., Z. Jiang, K. Aydin, J. Verlinde, E. E. Clothiaux, and G. Botta, 2016: A polarimetric scattering database for non-spherical ice particles at microwave wavelengths. *Atmospheric Measurement Techniques*, **9 (10)**, 5119–5134, doi:10.5194/amt-9-5119-2016.

Maahn, M., C. Burgard, S. Crewell, I. V. Gorodetskaya, S. Kneifel, S. Lhermitte, K. Van Tricht, and N. P. M. van Lipzig, 2014: How does the spaceborne radar blind zone affect derived surface snowfall statistics in polar regions? *Journal of Geophysical Research: Atmospheres*, **119 (24)**, 13,604–13,620, doi:10.1002/2014JD022079, 2014JD022079.

Magono, C., and T. Nakamura, 1965: Aerodynamic studies of falling snowflakes. *Journal of Meteorological Society of Japan*, **43**, 139–147.

Mallet, C., and L. Barthes, 2009: Estimation of gamma raindrop size distribution parameters: Statistical fluctuations and estimation errors. *Journal of Atmospheric and Oceanic Technology*, **26 (8)**, 1572–1584, doi:10.1175/2009JTECHA1199.1.

Marshall, J. S., and K. L. S. Gunn, 1952: Measurement of snow parameters by radar. *Journal of Meteorology*, **9 (5)**, 322–327, doi:10.1175/1520-0469(1952)009<0322:MOSPBR>2.0.CO;2.

Marshall, J. S., and W. M. K. Palmer, 1948: The distribution of raindrops with size. *Journal of Meteorology*, **5 (4)**, 165–166, doi:10.1175/1520-0469(1948)005<0165:TDORWS>2.0.CO;2.

Matrosov, S., 1992: Radar reflectivity in snowfall. *IEEE Transactions on Geoscience and Remote Sensing*, **30 (3)**, 454–461, doi:10.1109/36.142923.

Matrosov, S., 2007: Modeling backscatter properties of snowfall at millimeter wavelengths. *Journal of the Atmospheric Sciences*, **64 (5)**, 1727 –1736, doi:10.1175/JAS3904.1.

Matrosov, S., 2008: Assessment of radar signal attenuation caused by the melting hydrometeor layer. *IEEE Transactions on Geoscience and Remote Sensing*, **46 (4)**, 1039 –1047.

Matrosov, S., R. Reinking, and I. Djalalova, 2005a: Inferring fall attitudes of pristine dendritic crystals from polarimetric radar data. *Journal of Atmospheric Sciences*, **62**, 241–250, doi:10.1175/JAS-3356.1.

Matrosov, S. Y., 1998: A dual-wavelength radar method to measure snowfall rate. *Journal of Applied Meteorology*, **37 (11)**, 1510–1521, doi:10.1175/1520-0450(1998)037<1510:ADWRMT>2.0.CO;2.

Matrosov, S. Y., C. Campbell, D. Kingsmill, and E. Sukovich, 2009: Assessing snowfall rates from X-band radar reflectivity measurements. *Journal of Atmospheric and Oceanic Technology*, **26 (11)**, 2324–2339, doi:10.1175/2009JTECHA1238.1.

Matrosov, S. Y., K. A. Clark, and D. E. Kingsmill, 2007: A polarimetric radar approach to identify rain, melting-layer, and snow regions for applying corrections to vertical profiles of reflectivity. *Journal of Applied Meteorology and Climatology*, **46 (2)**, 154–166, doi:10.1175/JAM2508.1.

Matrosov, S. Y., A. J. Heymsfield, and Z. Wang, 2005b: Dual-frequency radar ratio of nonspherical atmospheric hydrometeors. *Geophysical Research Letters*, **32 (13)**, doi:10.1029/2005GL023210, l13816.

Matrosov, S. Y., M. D. Shupe, and I. V. Djalalova, 2008: Snowfall retrievals using millimeter-wavelength cloud radars. *Journal of Applied Meteorology and Climatology*, **47 (3)**, 769–777, doi:10.1175/2007JAMC1768.1.

Matsuo, T., and Y. Sasyo, 1981a: Empirical formula for the melting rate of snowflakes. *Journal of the Meteorological Society of Japan*, **59**, 1–8.

Matsuo, T., and Y. Sasyo, 1981b: Melting of snowflakes below freezing level in the atmosphere. *Journal of the Meteorological Society of Japan*, **59 (1)**, 10–24.

Mätzler, C., and U. Wegmüller, 1987: Dielectric properties of freshwater ice at microwave frequencies. *Journal of Physics D: Applied Physics*, **20 (12)**, 1623–1630, doi:10.1088/0022-3727/20/12/013.

Meneghini, R., and L. Liao, 1996: Comparisons of cross sections for melting hydrometeors as derived from dielectric mixing formulas and a numerical method. *Journal of Applied Meteorology*, **35 (10)**, 1658–1670, doi:10.1175/1520-0450(1996)035<1658:COCSFM>2.0.CO;2.

Meneghini, R., and L. Liao, 2000: Effective dielectric constants of mixed-phase hydrometeors. *Journal of Atmospheric and Oceanic Technology*, **17 (5)**, 628–640, doi:10.1175/1520-0426(2000)017<0628:EDCOMP>2.0.CO;2.

Merchiers, O., F. Moreno, F. González, and J. Saiz, 2007: Light scattering by an ensemble of interacting dipolar particles with both electric and magnetic polarizabilities. *Physical Review A*, **76**, 043 834, doi:10.1103/PhysRevA.76.043834.

Michelson, D. B., 2004: Systematic correction of precipitation gauge observations using analyzed meteorological variables. *Journal of Hydrology*, **290 (3–4)**, 161–177, doi:https://doi.org/10.1016/j.jhydrol.2003.10.005.

Mie, G., 1908: Beiträge zur optik trüber medien, speziell kolloidaler metallösungen. *Annalen der Physik, vierte Folge*, **Band 25 (3)**, 377–445.

Mishchenko, M., J. Hovenier, and L. Travis, Eds., 2000: *Light Scattering by Nonspherical Particles*. Academic Press, San Diego, USA.

Mishchenko, M., L. Travis, and A. Lacis, 2002: *Scattering, absorption, and emission of light by small particles*. Cambridge University Press, USA, 462 pp.

Mishchenko, M. I., and L. D. Travis, 2017: T-matrix, electromagnetic scattering by particles and surfaces. URL https://www.giss.nasa.gov/staff/mmishchenko/.

Mishima, O., D. Klug, and E. Whalley, 1983: The far-infrared spectrum of ice in the range 8-25 cm^{-1}. Sound waves and difference bands, with application to saturn's rings. *The Journal of Chemical Physics*, **78 (11)**, 6399–6404, doi:10.1063/1.444700.

Mitchell, D., 1996: Use of mass- and area-dimensional power laws for determining precipitation particle terminal velocities. *Journal of the Atmospheric Sciences*, **53 (12)**, 1710–1723, doi:10.1175/1520-0469(1996)053<1710:UOMAAD>2.0.CO;2.

Mitchell, D., A. Huggins, and V. Grubisic, 2006: A new snow growth model with application to radar precipitation estimates. *Atmospheric Research*, **82 (1)**, 2–18, doi:https://doi.org/10.1016/j.atmosres.2005.12.004.

Mitchell, D., R. Zhang, and R. Pitter, 1990: Mass-dimensional relationships for ice particles and the influence of riming on snowfall rates. *Journal of Applied Meteorology*, **29**, 153–163, doi:10.1175/1520-0450(1990)029<0153:MDRFIP>2.0.CO;2.

Mitchell, D. L., 1988: Evolution of snow-size spectra in cyclonic storms. Part I: Snow growth by vapor deposition and aggregation. *Journal of the Atmospheric Sciences*, **45 (22)**, 3431–3451, doi:10.1175/1520-0469(1988)045<3431:EOSSSI>2.0.CO;2.

Mitchell, D. L., and A. J. Heymsfield, 2005: Refinements in the treatment of ice particle terminal velocities, highlighting aggregates. *Journal of Atmospheric Sciences*, **62 (5)**, 1637–1644, doi:10.1175/JAS3413.1.

Mitra, S., O. Vohl, M.Ahr, and H. Pruppacher, 1990: A wind-tunnel and theoretical study of melting behavior of atmospheric ice particles IV. Experiment and theory for snow flakes. *Journal of the Atmospheric Sciences*, **47 (5)**, 584–591, doi:10.1175/1520-0469(1990)047<0584:AWTATS>2.0.CO;2.

Moisseev, D., A. von Lerber, and J. Tiira, 2017: Quantifying the effect of riming on snowfall using ground-based observations. *Journal of Geophysical Research: Atmospheres*, **122 (7)**, 4019–4037, doi:10.1002/2016JD026272.

Moisseev, D. N., and V. Chandrasekar, 2007: Examination of the μ–Λ relation suggested for drop size distribution parameters. *Journal of Atmospheric and Oceanic Technology*, **24 (5)**, 847–855, doi:10.1175/JTECH2010.1.

Moisseev, D. N., S. Lautaportti, J. Tyynelä, and S. Lim, 2015: Dual-polarization radar signatures in snowstorms: Role of snowflake aggregation. *Journal of Geophysical Research: Atmospheres*, **120 (24)**, 12 644–12 655, doi:10.1002/2015JD023884.

Morrison, J. A., and M. J. Cross, 1974: Scattering of a plane electromagnetic wave by axisymmetric raindrops. *The Bell System Technical Journal*, **53 (6)**, 955–1019, doi:10.1002/j.1538-7305.1974.tb02779.x.

Mosimann, L., E. Weingartner, and A. Waldvogel, 1994: An analysis of accreted drop sizes and mass on rimed snow crystals. *Journal of the Atmospheric Sciences*, **51 (11)**, 1548–1558, doi:10.1175/1520-0469(1994)051<1548:AAOADS>2.0.CO;2.

Moss, S., and D. Johnson, 1994: Aircraft measurements to validate and improve numerical model parametrisations of ice to water ratios in clouds. *Atmospheric Research*, **34 (1)**, 1 – 25, doi:http://dx.doi.org/10.1016/0169-8095(94)90078-7.

Mulholland, G. W., C. F. Bohren, and K. A. Fuller, 1994: Light scattering by agglomerates: Coupled electric and magnetic dipole method. *Langmuir*, **10 (8)**, 2533–2546, doi:10.1021/la00020a009.

Munchak, S. J., and G. Skofronick-Jackson, 2013: Evaluation of precipitation detection over various surfaces from passive microwave imagers and sounders. *Atmospheric Research*, **131**, 81 – 94, doi:http://dx.doi.org/10.1016/j.atmosres.2012.10.011.

Muramoto, K.-I., K. Matsuura, and T. Shiina, 1995: Measuring the density of snow particles and snowfall rate. *Electronics and Communications in Japan (Part III: Fundamental Electronic Science)*, **78 (11)**, 71–79, doi:10.1002/ecjc.4430781107.

Nakaya, U., and T. Tereda, 1935: Simultaneous observations of the mass, falling velocity and form of individual snow crystals. *Journal of the Faculty of Science, Hokkaido Imperial University. Ser. 2, Physics*, **1 (7)**, 191–200.

Nešpor, V., W. F. Krajewski, and A. Kruger, 2000: Wind-induced error of raindrop size distribution measurement using a two-dimensional video disdrometer. *Journal of Atmospheric and Oceanic Technology*, **17 (11)**, 1483–1492, doi:10.1175/1520-0426(2000)017<1483:WIEORS>2.0.CO;2.

New, M., M. Todd, M. Hulme, and P. Jones, 2001: Precipitation measurements and trends in the twentieth century. *International Journal of Climatology*, **21 (15)**, 1889–1922, doi:10.1002/joc.680.

Newman, A., P. Kucera, and L. Bliven, 2009: Presenting the Snowflake Video Imager (SVI). *Journal of Atmospheric and Oceanic Technology*, **26 (2)**, 167–179, doi:10.1175/2008JTECHA1148.1.

Noh, Y.-J., G. Liu, A. S. Jones, and T. H. Vonder Haar, 2009: Toward snowfall retrieval over land by combining satellite and in situ measurements. *Journal of Geophysical Research: Atmospheres*, **114 (D24)**, doi:10.1029/2009JD012307, d24205.

Noh, Y.-J., G. Liu, E.-K. Seo, J. R. Wang, and K. Aonashi, 2006: Development of a snowfall retrieval algorithm at high microwave frequencies. *Journal of Geophysical Research: Atmospheres*, **111 (D22)**, doi:10.1029/2005JD006826, d22216.

Norin, L., A. Devasthale, T. S. L'Ecuyer, N. B. Wood, and M. Smalley, 2015: Intercomparison of snowfall estimates derived from the CloudSat Cloud Profiling Radar and the ground-based weather radar network over Sweden. *Atmospheric Measurement Techniques*, **8 (12)**, 5009–5021, doi:10.5194/amt-8-5009-2015.

Nowell, H., G. Liu, and R. Honeyager, 2013: Modeling the microwave single-scattering properties of aggregate snowflakes. *Journal of Geophysical Research: Atmospheres*, **118 (14)**, 7873–7885, doi:10.1002/jgrd.50620.

Oguchi, T., 1983: Electromagnetic wave propagation and scattering in rain and other hydrometeors. *Proceedings of the IEEE*, **71 (9)**, 1029–1078.

Ohtake, T., 1969: Observations of size distributions of hydrometeors through the melting layer. *Journal of the Atmospheric Sciences*, **26 (3)**, 545–557, doi: 10.1175/1520-0469(1969)026<0545:OOSDOH>2.0.CO;2.

Ohtake, T., and T. Hemni, 1970: Radar reflectivity on aggregated snowflakes. *14th Conference on Radar Meteorology, American Meteorological Society*, Tuscon, Arizona, USA, 209–210.

Olson, W., P. Bauer, N. Viltard, D. Johnson, W. Tao, R. Meneghini, and L. Liao, 2001: A melting-layer model for passive/active microwave remote sensing application. Part I: Model formulation and comparison with observations. *Journal of the Applied Meteorology*, **40 (7)**, 1145–1163, doi:10.1175/1520-0450(2001) 040<1145:AMLMFP>2.0.CO;2.

Oraltay, R. G., and J. Hallett, 2005: The melting layer: A laboratory investigation of ice particle melt and evaporation near 0°C. *Journal of Applied Meteorology*, **44 (2)**, 206–220, doi:10.1175/JAM2194.1.

Ori, D., T. Maestri, R. Rizzi, D. Cimini, M. Montopoli, and F. S. Marzano, 2014: Scattering properties of modeled complex snowflakes and mixed-phase particles at microwave and millimeter frequencies. *Journal of Geophysical Research: Atmospheres*, **119 (16)**, 9931–9947, doi:10.1002/2014JD021616.

Passarelli, R., 1978: A theoretical explanation for Z-R relationships in snow. *18th Conference on Radar Meteorology, American Meteorological Society*, Atlanta, Georgia, USA, 332–335.

Peltoniemi, J., 1996: Variational volume integral equation method for electromagnetic scattering by irregular grains. *Journal of Quantitative Spectroscopy & Radiative Transfer*, **55 (5)**, 637–647.

Penttilä, A., E. Zubko, K. Lumme, K. Muinonen, M. Yurkin, B. Draine, J. R. A. Hoekstra, and Y. Shkuratov, 2007: Comparison between discrete dipole implementations and exact techniques. *Journal of Quantitative Spectroscopy & Radiative Transfer*, **106 (1-3)**, 417–436, doi:10.1016/j.jqsrt.2007.01.026.

Petäjä, T., and Coauthors, 2016: BAECC: A field campaign to elucidate the impact of Biogenic Aerosols on Clouds and Climate. *Bulletin of the American Meteorological Society*, **97 (10)**, 1909–1928, doi:10.1175/BAMS-D-14-00199.1.

Peterson, T. C., and Coauthors, 1998: Homogeneity adjustments of in situ atmospheric climate data: A review. *International Journal of Climatology*, **18 (13)**, 1493–1517, doi:10.1002/(SICI)1097-0088(19981115)18:13<1493::AID-JOC329> 3.0.CO;2-T.

Petty, G. W., and W. Huang, 2010: Microwave backscatter and extinction by soft ice spheres and complex snow aggregates. *Journal of the Atmospheric Sciences*, **67 (3)**, 769–787, doi:10.1175/2009JAS3146.1.

Petty, G. W., and W. Huang, 2011: The modified gamma size distribution applied to inhomogeneous and nonspherical particles: Key relationships and conversions. *Journal of the Atmospheric Sciences*, **68 (7)**, 1460–1473, doi: 10.1175/2011JAS3645.1.

Pitter, R., and H. Pruppacher, 1974: A numerical investigation of collision efficiencies of simple ice plates colliding with supercooled water drops. *Journal of the Atmospheric Sciences*, **31 (2)**, 551–559, doi:10.1175/1520-0469(1974)031<0551:ANIOCE>2.0.CO;2.

Power, B. A., P. W. Summers, and J. D'Avignon, 1964: Snow crystal forms and riming effects as related to snowfall density and general storm conditions. *Journal of the Atmospheric Sciences*, **21 (3)**, 300–305, doi:10.1175/1520-0469(1964)021<0300:SCFARE>2.0.CO;2.

Praz, C., Y.-A. Roulet, and A. Berne, 2017: Solid hydrometeor classification and riming degree estimation from pictures collected with a Multi-Angle Snowflake Camera. *Atmospheric Measurement Techniques*, **10 (4)**, 1335–1357, doi:10.5194/amt-10-1335-2017.

Pruppacher, H., and J. Klett, 1997: *Microphysics of Clouds and Precipitation*. Kluwer Academic, Netherlands.

Puhakka, T., 1975: On the dependence of the Z-R relation on the temperature in snowfall. *16th Conference on Radar Meteorology, American Meteorological Society*, Houston, Texas, USA, 504–507.

Purcell, E., and C. Pennypacker, 1973: Scattering and absorption of light by non-spherical dielectric grains. *Astrophysical Journal*, **186**, 705–714, doi:10.1086/152538.

Radok, U., and R. C. Lile, 2013: *A Year of Snow Accumulation at Plateau Station*, 17–26. American Geophysical Union, doi:10.1002/9781118664872.ch2.

Rangno, A. L., and P. V. Hobbs, 2001: Ice particles in stratiform clouds in the arctic and possible mechanisms for the production of high ice concentrations. *Journal of Geophysical Research: Atmospheres*, **106 (D14)**, 15 065–15 075, doi:10.1029/2000JD900286.

Rangno, A. L., and P. V. Hobbs, 2005: Microstructures and precipitation development in cumulus and small cumulonimbus clouds over the warm pool of the tropical Pacific Ocean. *Quarterly Journal of the Royal Meteorological Society*, **131 (606)**, 639–673, doi:10.1256/qj.04.13.

Rasmussen, R., M. Dixon, S. Vasiloff, F. Hage, S. Knight, J. Vivekanandan, and M. Xu, 2003: Snow nowcasting using a real-time correlation of radar reflectivity with snow gauge accumulation. *Journal of Applied Meteorology*, **42 (1)**, 20–36, doi:10.1175/1520-0450(2003)042<0020:SNUART>2.0.CO;2.

Rasmussen, R., and H. Pruppacher, 1982: A wind tunnel and theoretical study of the melting behavior of atmospheric ice particles I: A wind tunnel study of frozen drops of radius < 500 μm. *Journal of Atmospheric Sciences*, **39 (1)**, 152–158, doi:10.1175/1520-0469(1982)039<0152:AWTATS>2.0.CO;2.

Rasmussen, R. M., and A. J. Heymsfield, 1987: Melting and shedding of graupel and hail. Part I. Model physics. *Journal of the Atmospheric Sciences*, **44 (19)**, 2754–2763.

Rinehart, R., 1997: *Radar for Meteorologists*. third edition ed., Rinehart Publications, Grand Forks, USA.

Roebber, P. J., S. L. Bruening, D. M. Schultz, and J. V. J. Cortinas, 2003: Improving snowfall forecasting by diagnosing snow density. *Weather and Forecasting*, **18 (2)**, 264–287, doi:10.1175/1520-0434(2003)018<0264:ISFBDS>2.0.CO;2.

Russchenberg, H., and L. Ligthart, 1996: Backscattering by and propagation through the melting layer of precipitation: A new polarimetric model. *IEEE Transactions on Geoscience and Remote Sensing*, **34 (1)**, 3–14, doi:10.1109/36.481885.

Ryan, W. A., N. J. Doesken, and S. R. Fassnacht, 2008: Evaluation of ultrasonic snow depth sensors for U.S. snow measurements. *Journal of Atmospheric and Oceanic Technology*, **25 (5)**, 667–684, doi:10.1175/2007JTECHA947.1.

Ryzhkov, A., A. Giangrande, A. Khain, M. Pinsky, and A. Pokrovsky, 2008: Exploring model-based polarimetric retrieval of vertical profiles of precipitation. *The fifth European Conference on Radar Meteorology and Hydrology, ERAD 2008, Helsinki, Finland*.

Saltikoff, E., A. Huuskonen, H. Hohti, J. Koistinen, and H. Järvinen, 2010: Quality assurance in the FMI Doppler weather radar network. *Boreal Environment Research*, **15**, 579–594.

Saltikoff, E., P. Lopez, A. Taskinen, and S. Pulkkinen, 2015: Comparison of quantitative snowfall estimates from weather radar, rain gauges and a numerical weather prediction model. *Boreal Environment Research*, **20**, 667–678.

Schefold, R., 2004: Messungen von Schneeflocken: Die Fallgeschwindigkeit und eine Abschätzung weiterer Grössen. Ph.D. thesis, ETH Zürich, Switzerland, 182 pp., 10.3929/ethz-a-004714039.

Schiermeier, Q., 2010: The real holes in climate science. *Nature*, **463**, 284–287, doi:10.1038/463284a.

Schmitt, C., and A. Heymsfield, 2009: The size distribution and mass-weighted terminal velocity of low-latitude tropopause cirrus crystal populations. *Journal of the Atmospheric Sciences*, **66 (7)**, 2013–2028, doi:10.1175/2009JAS3004.1.

Schmitt, C., and A. Heymsfield, 2010: The dimensional characteristics of ice crystal aggregates from fractal geometry. *Journal of the Atmospheric Sciences*, **67 (5)**, 1605–1616, doi:10.1175/2009JAS3187.1.

Schönhuber, M., G. Lammer, and W. Randeu, 2007: One decade of imaging precipitation measurement by 2D-video-distrometer. *Advances in Geosciences*, **10**, 85–90, doi:10.5194/adgeo-10-85-2007.

Schulz, F. M., K. Stamnes, and J. J. Stamnes, 1998: Scattering of electromagnetic waves by spheroidal particles: A novel approach exploiting the T-matrix computed in spheroidal coordinates. *Applied Optics*, **37 (33)**, 7875–7896, doi:10.1364/AO.37.007875.

Sekhon, R., and R. Srivastava, 1971: Doppler radar observations of drop-size distributions in a thunderstorm. *Journal of the Atmospheric Sciences*, **28 (6)**, 983–994, doi:10.1175/1520-0469(1971)028<0983:DROODS>2.0.CO;2.

Sekhon, R. S., and R. C. Srivastava, 1970: Snow size spectra and radar reflectivity. *Journal of the Atmospheric Sciences*, **27 (2)**, 299–307, doi:10.1175/1520-0469(1970)027<0299:SSSARR>2.0.CO;2.

Sevruk, B., and S. Klemm, 1989: Catalogue of national standard precipitation gauges, *WMO Instruments and Observing Methods*. Tech. Rep. 39, 50 pp.

Sihvola, A., 1999: *Electromagnetic Mixing Formulas and Applications*. The Institution of Electrical Engineers, London.

Sinclair, V., D. Moisseev, and A. von Lerber, 2016: How dual-polarization radar observations can be used to verify model representation of secondary ice. *Journal of Geophysical Research*, **121 (18)**, 10 954–10 970, doi:10.1002/2016JD025381.

Skaropoulos, N., and H. Russchenberg, 2003: Simulations of Doppler spectra in the melting layer of precipitation. *Geophysical Research Letters*, **30 (12)**, 36–(1–4), doi:10.1029/2003GL016959.

Skaropoulos, N. C., and H. W. J. Russchenberg, 2002: Light scattering by arbitrarily oriented rotationally symmetric particles. *Journal of Optical Society of America A*, **19 (8)**, 1583–1591, doi:10.1364/JOSAA.19.001583.

Skofronick-Jackson, G., B. Johnson, and S. Munchak, 2013a: Detection thresholds of falling snow from satellite-borne active and passive sensors. *IEEE Transactions on Geoscience and Remote Sensing*, **51 (7)**, 4177–4189, doi:10.1109/TGRS.2012.2227763.

Skofronick-Jackson, G., and B. T. Johnson, 2011: Surface and atmospheric contributions to passive microwave brightness temperatures for falling snow events. *Journal of Geophysical Research: Atmospheres*, **116 (D2)**, doi:10.1029/2010JD014438, d02213.

Skofronick-Jackson, G., and Coauthors, 2015: Global Precipitation Measurement Cold Season Precipitation Experiment (GCPEX): For measurement's sake, let it snow. *Bulletin of the American Meteorological Society*, **96 (10)**, 1719–1741, doi:10.1175/BAMS-D-13-00262.1.

Skofronick-Jackson, G. M., B. T. Johnson, and S. J. Munchak, 2013b: Detection thresholds of falling snow from satellite-borne active and passive sensors. *IEEE Transactions on Geoscience and Remote Sensing*, **51 (7)**, 4177–4189, doi:10.1109/TGRS.2012.2227763.

Skofronick-Jackson, G. M., M.-J. Kim, J. A. Weinman, and D.-E. Chang, 2004: A physical model to determine snowfall over land by microwave radiometry. *IEEE Transactions on Geoscience and Remote Sensing*, **42 (5)**, 1047–1058, doi:10.1109/TGRS.2004.825585.

Smalley, M., T. L'Ecuyer, M. Lebsock, and J. Haynes, 2014: A comparison of precipitation occurrence from the NCEP Stage IV QPE product and the CloudSat Cloud Profiling Radar. *Journal of Hydrometeorology*, **15 (1)**, 444–458, doi:10.1175/JHM-D-13-048.1.

Smith, C. J., 1986: The reduction of errors caused by bright bands in quantitative rainfall measurements made using radar. *Journal of Atmospheric and Oceanic Technology*, **3 (1)**, 129–141, doi:10.1175/1520-0426(1986)003<0129:TROECB>2.0.CO;2.

Smith, P., and D. Kliche, 2005: The bias in moment estimators for parameters of drop size distribution functions: Sampling from exponential distributions. *Journal of Applied Meteorology*, **44 (8)**, 1195–1205, doi:10.1175/JAM2258.1.

Stephens, G. L., and C. D. Kummerow, 2007: The remote sensing of clouds and precipitation from space: A review. *Journal of the Atmospheric Sciences*, **64 (11)**, 3742–3765, doi:10.1175/2006JAS2375.1.

Stephens, G. L., and Coauthors, 2008: Cloudsat mission: Performance and early science after the first year of operation. *Journal of Geophysical Research: Atmospheres*, **113 (D8)**, doi:10.1029/2008JD009982, d00A18.

Stewart, R., J. Marwitz, and J. Pace, 1984: Characteristics through the melting layer of stratiform clouds. *Journal of the Atmospheric Sciences*, **41 (22)**, 3227–3237, doi:10.1175/1520-0469(1984)041<3227:CTTMLO>2.0.CO;2.

Straka, J., D. Zrnić, and A. Ryzhkov, 2000: Bulk hydrometeor classification and quantification using polarimetric radar data: Synthesis of relations. *Journal of Applied Meteorology*, **39 (8)**, 1341–1372, doi:10.1175/1520-0450(2000)039<1341:BHCAQU>2.0.CO;2.

Szyrmer, W., and I. Zawadzki, 1999: Modeling of the melting layer. Part I: Dynamics and microphysics. *Journal of the Atmospheric Sciences*, **56**, 3573–3592, doi:10.1175/1520-0469(1999)056<3573:MOTMLP>2.0.CO;2.

Szyrmer, W., and I. Zawadzki, 2010: Snow studies. Part II: Average relationship between mass of snowflakes and their terminal fall velocity. *Journal of the Atmospheric Sciences*, **67**, 3319 – 3335, doi:10.1175/2010JAS3390.1.

Szyrmer, W., and I. Zawadzki, 2014: Snow studies. Part III: Theoretical derivations for the ensemble retrieval of snow microphysics from dual-wavelength vertically pointing radars. *Journal of the Atmospheric Sciences*, **71 (3)**, 1158–1170, doi:10.1175/JAS-D-12-0285.1.

Tabary, P., A. Le Henaff, G. Vulpiani, J. Parent-du Châtelet, and J. Gourley, 2006: Melting layer characterization and identification with a C-band dual-polarization radar: A long-term analysis. *Fourth Europe an Conference on Radar in Meteorology and Hydrology (ERAD 2006)*, Barcelona, Spain.

Tanelli, S., S. L. Durden, E. Im, K. S. Pak, D. G. Reinke, P. Partain, J. M. Haynes, and R. T. Marchand, 2008: CloudSat's Cloud Profiling Radar after two years in orbit: Performance, calibration, and processing. *IEEE Transactions on Geoscience and Remote Sensing*, **46 (11)**, 3560–3573, doi:10.1109/TGRS.2008.2002030.

Testik, F. Y., and A. P. Barros, 2007: Toward elucidating the microstructure of warm rainfall: A survey. *Reviews of Geophysics*, **45 (2)**, doi:10.1029/2005RG000182.

Thompson, E. J., S. A. Rutledge, B. Dolan, V. Chandrasekar, and B. L. Cheong, 2014: A dual-polarization radar hydrometeor classification algorithm for winter precipitation. *Journal of Atmospheric and Oceanic Technology*, **31 (7)**, 1457–1481, doi:10.1175/JTECH-D-13-00119.1.

Tokay, A., A. Kruger, and W. F. Krajewski, 2001: Comparison of drop size distribution measurements by impact and optical disdrometers. *Journal of Applied Meteorology*, **40 (11)**, 2083–2097, doi:10.1175/1520-0450(2001)040<2083:CODSDM>2.0.CO;2.

Tokay, A., and D. A. Short, 1996: Evidence from tropical raindrop spectra of the origin of rain from stratiform versus convective clouds. *Journal of Applied Meteorology*, **35 (3)**, 355–371, doi:10.1175/1520-0450(1996)035<0355:EFTRSO>2.0.CO;2.

Toyoshima, K., H. Masunaga, and F. Furuzawa, 2015: Early evaluation of Ku- and Ka-band sensitivities for the GPM DPR. *Scientific Online Letters on the Atmosphere*, **11**, 14–17.

Trömel, S., A. V. Ryzhkov, P. Zhang, and C. Simmer, 2014: Investigations of backscatter differential phase in the melting layer. *Journal of Applied Meteorology and Climatology*, **53 (10)**, 2344–2359, doi:10.1175/JAMC-D-14-0050.1.

Tsang, L., and J. Kong, 2001: *Scattering of Electromagnetic Waves: Advanced Topics*. John Wiley & Sons, inc, New York, 413 pp.

Tsang, L., J. Kong, and K. Ding, 2000: *Scattering of Electromagnetic Waves: Theories and Applications*. John Wiley & Sons, New York, 426 pp.

Tsang, L., J. Kong, K. Ding, and C. Ao, 2001: *Scattering of the Electromagnetic waves: Numerical Simulations*. John Wiley & Sons, inc, New York, 705 pp.

Tyynelä, J., 2017: Scattering databases for ice and snow particles in the microwave region. *1st International Summer Snow Workshop*, 28th - 30th June, Cologne, Germany, URL http://snowport.meteo.uni-koeln.de/restricted-area/publications-repository/workshop_presentations-20170706t120755z-001.zip.

Tyynelä, J., J. Leinonen, D. Moisseev, and T. Nousiainen, 2011: Radar backscattering from snowflakes: Comparison of fractal, aggregate, and soft spheroid models. *Journal of Atmospheric and Oceanic Technology*, **28 (11)**, 1365–1372, doi:10.1175/JTECH-D-11-00004.1.

Tyynelä, J., J. Leinonen, D. Moisseev, T. Nousiainen, and A. von Lerber, 2014: Modeling radar backscattering from melting snowflakes using spheroids with nonuniform distribution of water. *Journal of Quantitative Spectroscopy and Radiative Transfer*, 504–519, doi:101016/jjqsrt201309013.

Tyynelä, J., T. Nousiainen, S. Göke, and K. Muinonen, 2009: Modeling C-band single scattering properties of hydrometeors using discrete-dipole approximation and T-matrix method. *Journal of Quantative Spectroscopy & Radiative Transfer*, **110**, 1654–1664.

Tyynelä, J., J. Leinonen, C. D. Westbrook, D. Moisseev, and T. Nousiainen, 2013: Applicability of the Rayleigh-Gans approximation for scattering by snowflakes at microwave frequencies in vertical incidence. *Journal of Geophysical Research: Atmospheres*, **118 (4)**, 1826–1839, doi:10.1002/jgrd.50167.

Tzivion, S., G. Feingold, and Z. Levin, 1987: An efficient numerical solution to the stochastic collection equation. *Journal of the Atmospheric Sciences*, **44 (21)**, 3139–3149, doi:10.1175/1520-0469(1987)044<3139:AENSTT>2.0.CO;2.

Ulbrich, C. W., 1983: Natural variations in the analytical form of the raindrop size distribution. *Journal of Climate and Applied Meteorology*, **22 (10)**, 1764–1775, doi:10.1175/1520-0450(1983)022<1764:NVITAF>2.0.CO;2.

Ulbrich, C. W., and D. Atlas, 1998: Rainfall microphysics and radar properties: Analysis methods for drop size spectra. *Journal of Applied Meteorology*, **37 (9)**, 912–923, doi:10.1175/1520-0450(1998)037<0912:RMARPA>2.0.CO;2.

Wang, P. K., and W. Ji, 2000: Collision efficiencies of ice crystals at low–intermediate reynolds numbers colliding with supercooled cloud droplets: A numerical study. *Journal of the Atmospheric Sciences*, **57 (8)**, 1001–1009, doi:10.1175/1520-0469(2000)057<1001:CEOICA>2.0.CO;2.

Ware, E. C., D. M. Schultz, H. E. Brooks, P. J. Roebber, and S. L. Bruening, 2006: Improving snowfall forecasting by accounting for the climatological variability of snow density. *Weather and Forecasting*, **21 (1)**, 94–103, doi:10.1175/WAF903.1.

Warren, S., 1984: Optical constants of ice from the ultraviolet to the microwave. *Journal of Physics, D, Applied Physics*, **23 (8)**, 1206–1225, doi:10.1364/AO.23.001206.

Waterman, P., 1965: Matrix formulation of electromagnetic scattering. *Proceedings of the IEEE*, **53 (8)**, 805–812, doi:10.1109/PROC.1965.4058.

Waterman, P. C., 1971: Symmetry, unitarity, and geometry in electromagnetic scattering. *Phys. Rev. D*, **3 (4)**, 825–839, doi:10.1103/PhysRevD.3.825.

Westbrook, C., 2004: Universality in snowflake formation. Ph.d. thesis, University of Reading, Great Britannia, 84 pp.

Westbrook, C. D., R. C. Ball, and P. R. Field, 2006: Radar scattering by aggregate snowflakes. *Quarterly Journal of the Royal Meteorological Society*, **132 (616)**, 897–914, doi:10.1256/qj.05.82.

Wilks, D., 2011: *Statistical Methods in the Atmospheric Sciences*. Academic Press, Elsevier.

Willis, P. T., and A. J. Heymsfield, 1989: Structure of the melting layer in mesoscale convective system stratiform precipitation. *Journal of the Atmospheric Sciences*, **46 (13)**, 2008–2025, doi:10.1175/1520-0469(1989)046<2008:SOTMLI>2.0.CO;2.

Wiscombe, W., 1980: Improved Mie scattering algorithms. *Applied Optics*, **19 (9)**, 1505–1509, doi:10.1364/AO.19.001505.

WMO SPICE, 2017: Solid precipitation intercomparison experiment (2012-2015). URL www.wmo.int/pages/prog/www/IMOP/intercomparisons/SPICE/SPICE.html.

Wood, N., T. L'Ecuyer, F. Bliven, and G. Stephens, 2013: Characterization of video disdrometer uncertainties and impacts on estimates of snowfall rate and radar reflectivity. *Atmospheric Measurement Techniques*, **6**, 3635 – 3648, doi:10.5194/amt-6-3635-2013.

Wood, N. B., T. S. L'Ecuyer, A. J. Heymsfield, G. L. Stephens, D. R. Hudak, and P. Rodriguez, 2014: Estimating snow microphysical properties using collocated multisensor observations. *Journal of Geophysical Research: Atmospheres*, **119 (14)**, 8941–8961, doi:10.1002/2013JD021303.

Yaghjian, A., 1980: Electric dyadic Green's functions in the source region. *Proceedings of the IEEE*, **68 (2)**, 248–263, doi:10.1109/PROC.1980.11620.

Yano, J.-I., and V. T. J. Phillips, 2011: Ice–ice collisions: An ice multiplication process in atmospheric clouds. *Journal of the Atmospheric Sciences*, **68 (2)**, 322–333, doi:10.1175/2010JAS3607.1.

Yokoyama, T., and H. Tanaka, 1984: Microphysical processes of melting snowflakes detected by two-wavelength radar. Part I. Principle of measurement based on model calculation. *Journal of the Meteorological Society of Japan*, **62 (4)**, 650–666, doi:10.2151/jmsj1965.62.4_650.

Yokoyama, T., H. Tanaka, K. Nakamura, and A. J., 1984: Microphysical processes of melting snowflakes detected by two wavelength radar. Part II. Application of two wavelength radar technique. *Journal of the Meteorological Society of Japan*, **62 (4)**, 668–677, doi:10.2151/jmsj1965.62.4_668.

Young, K., 1993: *Microphysical Processes in Clouds*. Oxford University Press, 427 pp.

Yurkin, M., and A. Hoekstra, 2007: Discrete Dipole Approximation: An overview and recent developments. *Journal of Quantitative Spectroscopy & Radiative Transfer*, **106**, 558–589, doi:10.1016/j.jqsrt.2007.01.034.

Yurkin, M., V. Maltsev, and A. Hoekstra, 2007: The Discrete Dipole Approximation for simulation of light scattering by particles much larger than the wavelength. *Journal of Quantitative Spectroscopy and Radiative Transfer*, **106 (1-3)**, 546 – 557, doi:10.1016/j.jqsrt.2007.01.033.

Yuter, S. E., D. E. Kingsmill, L. B. Nance, and M. Löffler-Mang, 2006: Observations of precipitation size and fall speed characteristics within coexisting rain and wet snow. *Journal of Applied Meteorology and Climatology*, **45 (10)**, 1450–1464, doi:10.1175/JAM2406.1.

Zawadzki, I., E. Jung, and G. Lee, 2010: Snow studies. Part I: A study of natural variability of snow terminal velocity. *Journal of the Atmospheric Sciences*, **67**, 1591 – 1604, doi:10.1175/2010JAS3342.1.

Zawadzki, I., W. Szyrmer, C. Bell, and F. Fabry, 2005: Modeling of the melting layer. Part III: The density effect. *Journal of the Atmospheric Sciences*, **62**, 3705–3723.

Zhang, D., Z. Wang, A. Heymsfield, J. Fan, and T. Luo, 2014: Ice concentration retrieval in stratiform mixed-phase clouds using cloud radar reflectivity measurements and 1D ice growth model simulations. *Journal of the Atmospheric Sciences*, **71 (10)**, 3613–3635, doi:10.1175/JAS-D-13-0354.1.

Zhang, G., S. Luchs, A. Ryzhkov, M. Xue, R. L., and Q. Cao, 2011a: Winter precipitation microphysics characterized by polarimetric radar and video disdrometer observations in central Oklahoma. *Journal of Applied Meteorology and Climatology*, **50**, 1558–1570, doi:10.1175/2011JAMC2343.1.

Zhang, J., and Coauthors, 2011b: National Mosaic and Multi-Sensor QPE (NMQ) system: Description, results, and future plans. *Bulletin of the American Meteorological Society*, **92 (10)**, 1321–1338, doi:10.1175/2011BAMS-D-11-00047.1.

Zikmunda, J., 1972: Fall velocities of spatial crystals and aggregates. *Journal of Atmospheric Sciences*, **29**, 1511–1515, doi:10.1175/1520-0469(1972)029<1511:FVOSCA>2.0.CO;2.

Zikmunda, J., and G. Vali, 1972: Fall patterns and fall velocities of rimed ice crystals. *Journal of Atmospheric Sciences*, **29 (7)**, 1334–1347, doi:10.1175/1520-0469(1972)029<1334:FPAFVO>2.0.CO;2.

Zrnić, D., N. Balakrishnan, C. Ziegler, V. Bringi, K. Aydin, and T. Matejka, 1993: Polarimetric signatures in the stratiform region of a mesoscale convective system. *Journal of Applied Meteorology*, **32 (4)**, 678–693, doi:10.1175/1520-0450(1993)032<0678:PSITSR>2.0.CO;2.

FINNISH METEOROLOGICAL INSTITUTE
Erik Palménin aukio 1
P.O. Box 503
FI-00101 HELSINKI
tel. +358 29 539 1000
WWW.FMI.FI

FINNISH METEOROLOGICAL INSTITUTE
CONTRIBUTIONS No. 143
ISBN 978-952-336-044-0 (paperback)
ISSN 0782-6117
Erweko
Helsinki 2018

ISBN 978-952-336-045-7 (pdf)
Helsinki 2018